POLITECNICO
MILANO 1863

Doctoral Dissertation
Doctoral Program in Aerospace Engineering: Dipartimento di Scienze e Tecnologie Aerospaziali (DAER) (35.rd cycle)

Cloud Turbulence Microphysics At Interfaces

A DNS model with phase change and droplet interaction

Mina Golshan
Aerospace Engineering
ID: 10603475

* * * * *

Supervisors
Prof. Antonella Abbà
Prof. Daniela Tordella

Politecnico di Milano
October, 2022

I hereby declare that the contents and organization of this dissertation constitute my own original work and do not compromise in any way the rights of third parties, including those related to the security of personal data.

. . . . . .

Mina Golshan

Milan, Italy 20/10/2022

Summary

Clouds play a major role in meteorology and climate, due to their fundamental role in maintaining Earth's energy budget, by regulating the amount of solar energy that reaches the surface and the amount of the Earth's energy that is radiated back into space. Therefore, understanding how microphysical processes impact cloud generation and evolution is an important aspect of atmospheric physics and is still an open question. The complexity of the phenomenon is linked to the simultaneous action of many factors, including the evolution of atmospheric aerosols, interactions with water vapor, and associated unstable processes such as nucleation, condensation, evaporation, collision, and fragmentation of water droplets, all of which play a significant role in shaping the microphysical properties of clouds. The aforementioned main processes occur mainly in turbulent background airflow. Recently, the cloud boundary within cloud environments, has attracted considerable interest. The specific study of these interfaces leads to essential results that can bring rapid progress in the assessment of cloud dynamics. These kinds of interfaces are significant examples of inhomogeneity and anisotropy within turbulent airflow.

In the present work, I addressed a few problems in the area of small-scale cloud dynamics, using direct numerical simulations to study the temporal evolution of a perturbation located in the turbulent layer that generally separates a cloud from the surrounding clear air. The second part of the research is related to in-field experimentation using the mini green radiosondes developed in H2020 COMPLETE Marie Curie Network (http:// www.complete-h2020network.eu).

In the first part, an initial value problem is considered, where the temporal evolution of an initial distribution of turbulent kinetic energy, temperature, humidity, and droplet distributions are observed. A sufficiently intense stratification was observed to change the mixing dynamics. The formation of a sub-layer inside the shear-less layer was observed. The sub-layer, under a stable thermal stratification condition, behaved like a pit of kinetic energy. However, it was observed that turbulent kinetic energy transient growth took place under unstable conditions, which led to the formation of an energy peak just below the center of the shearless layer. A monodisperse droplet population with a radius of 15 μm and a polydisperse distribution with radii within the 0.6 – 40 μm range. Polydispersity has shown a different behavior in droplet evaporation and condensation both within the

homogeneous cloudy region and in the anisotropic interface mixing zone for both distributions. However, the two populations show a common aspect in the course of the transient, that is, an increased probability of collisions within the interface layer, which exhibits a marked anisotropic velocity fluctuation. These DNSs show that supersaturation fluctuations broaden the droplet size distribution and induce an increase in the collision rate. This result is in contrast to the classical growth of (non-turbulent) condensation, which leads to an increase in the average droplet size but also to a narrower droplet distribution.

It was also found that although the turbulent kinetic energy of the airflow hosting the cloud decreased by 90 % over the course of the simulation, the collision activity decreased by 40% inside the cloud, but increased by 25% in the mixing area of the interaction. The size distribution of the number density of the droplets, for the initially monodisperse population in the mixing layer, showed a standard deviation growth 15 times faster than that in the cloud region. In the polydisperse case, the concentration distributions were oppositely skewed, and the width of the distributions decreased more rapidly (about four times) over time within the interface region than in the cloud. Moreover, for the monodisperse population, a clustering of the values of the reaction, phase, and evaporation times, that is around 20-30 seconds, is observed in the central area of the mixing layer, just before the location where the maximum value of the supersaturation turbulent flux occurs. This clustering of values is similar for the polydisperse population but also includes the condensation time. The mismatch between the time derivative of the supersaturation and the condensation term in the interfacial mixing layer is correlated with the planar covariance of the horizontal longitudinal velocity derivatives of the carrier airflow and the supersaturation field, thus suggesting that a quasi-linear relationship may exist between these quantities.

In the second part, which contains in-field experimentation with radioprobes, is a preliminary result of ongoing work. It is mainly a proof-of-concept, and in the future, more variables could be measured by equipping the probes with suitable sensors. This part of the research is aimed to study the water droplet dispersion due to turbulence in warm clouds. The analysis is afforded by means of both experimental and numerical approaches (numerical approaches based on Horizon 2020 Marie Sklodowska Curie project). The radiosonde data post-processing is based on distance-neighbor graphs, which was the original statistical analysis proposed by L.F. Richardson in 1926.

While the first part of the work deals with DNSs and is limited to small-scale dynamics, the second part, which is experiments with radio probes, was aimed to analyse a few aspects of large-scale dispersion, which cannot be dealt with DNSs, and to measure in a Lagrangian way the state changes that a parcel of moist air undergoes in the atmosphere, thus providing a reference for numerical simulations. Therefore, the two parts reflect the same point of view on the same research work, i.e., the interaction between droplets and turbulence is seen from a different

timescale.

Summary (Italian Version)

Le nuvole, contribuendo a mantenere il bilancio energetico del nostro pianeta, regolando la quantità di energia solare che ne raggiunge la superficie e la quantità di energia che viene irradiata dalla Terra nello spazio, svolgono un ruolo fondamentale nella meteorologia e nel clima. Pertanto, comprendere come i processi microfisici influenzino la generazione e l'evoluzione delle nuvole è un aspetto importante della fisica dell'atmosfera.

La complessità del fenomeno è legata all'azione simultanea di molti fattori, tra cui l'evoluzione degli aerosol atmosferici, le interazioni con il vapore acqueo e i processi attivi sulla microscala come la nucleazione, la condensazione, l'evaporazione, la collisione e frammentazione delle gocce d'acqua. I suddetti processi sono ospitati entro la fase gassosa (aria) che si trova in uno stato di intenso moto turbolento. Recentemente, l'interesse della comunità scientifica si e' focalizzato sulla regione di confine delle nuvole, la cosiddetta regione di interfaccia nuvola – aria limpida, la cui dinamica è fondamentale nella comprensione dell'evoluzione delle nuvole. Questo tipo di interfaccia e' un esempio significativo di flusso in cui le fluttuazioni turbolente sono caratterizzate da forte disomogeneità ed anisotropia.

Nel presente lavoro, ho affrontato alcuni problemi nell'area della dinamica delle nuvole su piccola scala, utilizzando simulazioni numeriche dirette (DNS) per studiare l'evoluzione temporale di una perturbazione associata alla presenza di una stratificazione instabile localizzata vicino allo strato turbolento che generalmente separa una nuvola dall'aria limpida circostante. La seconda parte della ricerca è relativa alla sperimentazione sul campo utilizzando le mini radiosonde verdi sviluppate in H2020 COMPLETE Marie Curie Network (http:// [http://www.complete-h2020network.eu)]www.complete-h2020network.eu).

Nella prima parte del lavoro, considerando un problema ai valori iniziali, è stata simulata numericamente l'evoluzione temporale di una distribuzione iniziale di energia cinetica turbolenta, temperatura, umidità contenente due tipi diversi (mono e poli-dispersa) di popolazione di gocce di acqua. È stato osservato come le dinamiche di miscelamento nella zona di interfaccia vengano influenzate dalla stratificazione termica. È stata inoltre rilevata, all'interno dello strato di miscelamento, la formazione di un sotto-strato che, in condizioni di stratificazione termica stabile, si comporta come un pozzo di energia cinetica. Ed è stato osservato che la crescita dell'energia cinetica turbolenta ha avuto luogo in condizioni di stratificazione instabile, con la formazione di un picco di energia poco sotto il centro dello strato di miscelamento.

Per quel che concerne la fase acqua liquida, i due tipi di popolazione di goccioline considerati sono una distribuzione mono-dispersa sul raggio, con raggio delle gocce di 15 µm, ed una distribuzione poli-dispersa con raggi compresi tra 0,6 e 40

µm. Sebbene le due popolazioni presentino un comportamento diverso nei processi di evaporazione e di condensazione delle gocce sia all'interno della regione nuvolosa omogenea che nella zona di interfaccia, tuttavia, esse hanno un comportamento comune nello sviluppo del transitorio: ovvero un'aumentata probabilità di collisioni all'interno dello strato di interfaccia nuvola-aria chiare che contiene una marcata anisotropia delle fluttuazioni sia della velocità che dei due scalari trasportati, la temperatura ed la concentrazione di vapor d'acqua. I risultati delle simulazioni DNS mostrano che le fluttuazioni della sovrasaturazione ampliano la distribuzione delle dimensioni delle goccioline e inducono un aumento del tasso di collisione. Si e' inoltre riscontrato che sebbene l'energia cinetica turbolenta del flusso d'aria che ospita la nube diminuisca nel corso del transitorio del 90%, l'attività di collisione diminuisca del 40% all'interno della nube, ma aumenti del 25% nella regione di interfaccia altamente intermittente. La distribuzione dimensionale della densità numerica delle goccioline, per la popolazione inizialmente monodispersa, ha mostrato nello strato di miscelamento una crescita della deviazione standard 15 volte più veloce di quella nella regione omogena che modella la dinamica della nuvola. Nel caso polidisperso a iniziale densita' in massa uniforme sui raggi, la distribuzione evolve in modo opposto, presenta cioe' un restringimento. Anche in questo caso, il processo di restringimento si sviluppa più rapidamente (circa quattro volte) all'interno della regione di interfaccia che nella nuvola.

Inoltre, per la popolazione mono-dispersa, si è osservato un raggruppamento dei valori tipici dei tempi di reazione di fase ed evaporazione, pari a circa 20-30 secondi, nell'area centrale dello strato di mescolamento. Precisamente, cio' avviene poco prima dello strato in cui si verifica il valore massimo del flusso turbolento della sovrasaturazione. Nel caso della simulazione contenente la popolazione iniziale polidispersa, questa convergenza di valori include anche il tempo di condensazione. La differenza tra la derivata temporale della sovra-saturazione e il termine di condensazione nello strato di interfaccia è molto correlata alla covarianza tra la derivata longitudinale della fluttuazione della velocità dell'aria e le fluttuazioni del campo di sovra-saturazione, suggerendo così che possa esistere una relazione quasi lineare tra queste quantità. Il che e' concettualmente equivalente a dire che il termine di produzione della super-saturazione e' proporzionale al prodotto della fluttuazione della super-saturazione con la frequenza caratteristica delle piccole strutture della turbolenza della fase aria.

La parte finale della tesi descrive alcune preliminari sperimentazioni sul campo effettuate con le mini green radiosonde prototipate nell'ambito del Progetto Europeo H2020 Marie Curie (MSCA ITN ETN COMPLETE). Questa parte della ricerca è finalizzata allo studio della dispersione turbolenta nelle nuvole tiepide in cui sono presenti aria, vapore d'acqua e gocce d'acqua liquida, ma non aghi di ghiaccio. L'analisi preliminare è condotta mediante approcci sia sperimentali che numerici ed e' qui presentata soprattutto per dare una visione prospettica sui possibili futuri risultati ottenibili mediante l'elaborazione dei dati delle radiosonde. Essa

sara' fondata su statistiche del tipo grafici neighbour-distance, cioe' l'approccio di analisi statistica proposto da L.F. Richardson nel 1926.

Mentre la prima parte di questa tesi si basa su risultati ottenuti per mezzo di simulazioni numeriche DNS ed è limitata alle dinamiche su piccola scala, la parte relativa alle misure sul campo ha lo scopo: a) di analizzare alcuni aspetti della dispersione turbolenta su larga scala nelle nuvole tiepide, cosa allo stato dell'arte non ancora affrontabile per mezzo di simulazioni numeriche, e b) di misurare in modo lagrangiano i cambiamenti di stato che una particella di aria umida subisce nei suoi spostamenti entro l'atmosfera, fornendo così un riferimento per le simulazioni numeriche.

Acknowledgements

I need to sincerely thank my supervisors and advisor for their constructive guidance, academic advice, and continuous support. Therefore, I am grateful to **Professor Daniela Tordella**, whose knowledge, vision, experience, and support have led to the successful completion of this project.

The support of **Professor Antonella Abbà**, is also gratefully acknowledged. I sincerely thank her constructive guidance. This endeavor would not have been possible without her invaluable patience and feedback.

I also wish to thank **Professor Marco Vanni** and **Professor Pierangelo Masarati** for their kind support in leading my Ph.D. activities.

I would like to acknowledge the scientific comments and suggestions from the reviewers of the scientific publications that were published during my Ph.D. activities. It is impossible to make a complete list of all those who have helped me, but I will mention as many as possible.

I would like to express my deepest appreciation to my colleague, Shahbozbek Abdunabiev, for his kind time and suggestions, and moral support.

My most sincere thanks go to my friends and office mates, Dr. Federico Fraternale, Anja Visočnik, Dr. Zahra Shakarami, Dr. Miryam Paredes, Tessa Chiara Basso, Dr. Moein Mohammadi, Dr. Emmanuel Akinlabi, and Hamid Reza Zandi Pour.

Finally, my heartfelt gratitude goes to my Parents and love of life for their constant support. Words cannot express my gratitude for their support. Their belief in me has kept my spirits and motivation high during this process. I also would like to extend my sincere thanks to Elham Mohammadi, who has offered invaluable advice that will benefit me throughout my life.

This research was funded by the Marie-Skłodowska Curie Actions (MSCA) under the European Union's Horizon 2020 research and innovation programme (grant agreement no. 675675) http://www.complete-h2020network.eu, and an extension to the programme COMPLETE by the Department of Applied Science and Technology, Politecnico di Torino (DISAT). The first part of the scientific activity is carried out at the Department of Applied Science and Technology, Politecnico di Torino (POLITO), and the second part of the scientific activity is carried out at the Aerospace engineering department (Dipartimento di Scienze e Tecnologie

Aerospaziali (DAER)), Politecnico di Milano (POLIMI).

The computational resources were provided by the HPC@POLITO http://www.hpc.polito.it for this research during the activities in the Politecnico di Torino. I also acknowledge the CINECA award under the ISCRA initiative, for the availability of high-performance computing resources and support during my research activities in the Politecnico di Torino.

I like to gratefully acknowledge all the funding and computational resources, and partner organizations provided in support of my research. Below is the list of partners and organizations that collaborated in this research.


ScuDo
Scuola di Dottorato – Doctoral School
WHAT YOU ARE, TAKES YOU FAR

POLITECNICO
MILANO 1863
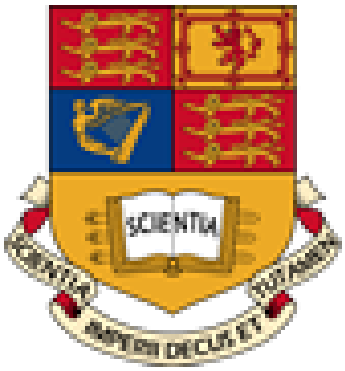
SCIENTIA

MAX-PLANCK-GESELLSCHAFT

TEL AVIV
UNIVERSITY
אוניברסיטת
תל אביב

UNIWERSYTET
WARSZAWSKI

cnrs

EnviSens
Technologies

SITAEL

INFN
Istituto Nazionale di Fisica Nucleare
INRiM
ISTITUTO NAZIONALE
DI RICERCA METROLOGICA

Incubatore
Imprese
Innovative
Politecnico
Torino

UNIVERSITÀ
DEGLI STUDI
DI TORINO

RAMOT
TAU
promising innovations

Bayerische
Forschungsallianz

iit
ISTITUTO
ITALIANO DI
TECNOLOGIA

REGIONE
PIEMONTE

MTF
MODERN TECHNOLOGIES & FILTRATION

UNIVERSITE DE LA REUNION
CNRS - METEO FRANCE
LACy
UMR 8105

ISAC

Umwelt
Forschungsstation
Schneefernerhaus

اگر شایسته ی تقدیم باشد:

تقدیم به پدر و مادرم؛

آنان که توانشان رفت تا به توانایی برسم، مویشان سپید گشت تا رویم سپید بماند، آنان که راستی قامتم در شکستگی قامتشان تجلی گشت.

در برابر وجود گرامیشان زانوی ادب بر زمین می نهم و با دلی مملو از عشق و محبت و خضوع به دستانشان بوسه می زنم و از خداوند بزرگ آرزوی سلامتیشان را دارم.

و از خواهر عزیزم که جسارت خواسته هایم در تمام لحظات ناب زندگی ام بود کمال تشکر را دارم.

و از همدم زندگیم، که آسایش او آرامش من است صمیمانه تشکر می کنم.

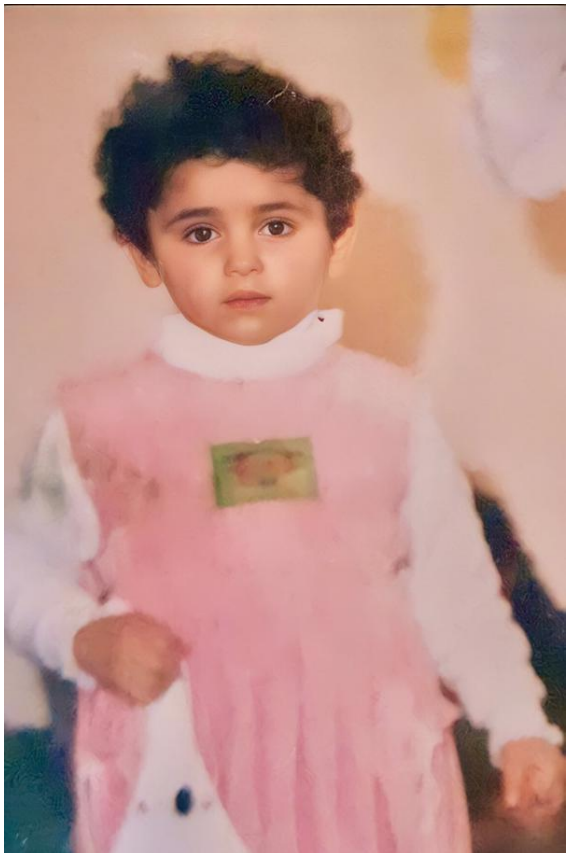

Contents

List of Tables

List of Figures

Chapter 1

Introduction and literature review

This chapter offers a brief insight into the microstructure of clouds and the effects of turbulence on atmospheric clouds and cloud charging mechanisms, as well as the interaction and distribution of cloud droplets. Applications and also developments in current research are discussed briefly, and the format of the thesis is described in detail. The first section of this chapter highlights the influence of turbulence on cloud systems and on the Earth's climatic system, while the second part focuses on the interactions between aerosols and cloud droplets within a turbulent atmosphere.

1.1 Coupling between cloud dynamics and microphysical processes

1.1.1 Turbulence in atmospheric physics

As has been claimed for more than 40 years of research, turbulent movements can be observed all over our world, and they indirectly influence all aspects of our lives. Turbulence is observed in many different and everyday phenomena. Understanding turbulence is essential in many scientific disciplines, such as engineering (car engines, aircraft turbines), the design of industrial equipment, such as pipes, ducts, and heat exchangers, cardiology field of medicine (airflow in the lungs), financial markets (oscillations in the price dynamics), in atmospheric and oceanic dynamics and in geophysics.

Turbulence was first investigated by Richardson L. and Lynch P. (1922) [102], Prandtl L. (1934) [100], Kolmogorov A.N. (1941) [12], Batchelor (1953) [85], Lumley and Panofsky (1964) [99], and Tennekes H. (1972) [67]. They defined turbulence as the chaos created in fluids by their properties. They described fluid properties as randomness, non-linearity effects, three-dimensional fluctuating vortices, dissipation, improved mixing, and continuum. They emphasized that turbulence shows

spatial and temporal structures over a wide range of scales. Perhaps the best definition of turbulence is 'the state of continuous instability' given by Tritton in Chapter 19 of his book [82]. One of the difficulties in forecasting the weather is the presence of turbulence in the atmosphere. We here focus our attention in particular on the study of the physical properties of turbulence in the atmosphere. Turbulence in the atmosphere is small-scale, irregular air movements characterized by winds of different speeds and directions. Turbulence is significant because it mixes and agitates the atmosphere and transports water vapor and smoke. It also affects other substances and energy, which are distributed both vertically and horizontally. Atmospheric turbulence is, basically, a unique form of turbulence caused by the shear, buoyancy, surface roughness, and convection of wind and it can be very intense. It is the crucial physical mechanism behind the occurrence of many atmospheric phenomena, such as thunderstorms and rainfall. Turbulence in the atmosphere is the mechanism by which heat and moisture from the earth's surface and momentum through the atmosphere are mixed. Other substances, such as aerosols or pollutants, are distributed both vertically and horizontally by turbulence, which is a clue in this study. A wide range of turbulence scales can be observed, ranging from O(1000 km) to the smallest dissipative eddies in the atmosphere, which is approximately O($\approx 1cm - 1mm$).

The main aim of the study has been to estimate the effects of turbulence on cloud formation from the droplet scale to the clouds themselves. These cloud structures have a significant effect on the weather and climate. However, they remain one of the most critical uncertainties for prediction models and a weak hyperlink in atmospheric circulation information. In atmospheric science, processes that form clouds and influence cloud field properties can usually be classified as microphysical (including chemistry and the effects of aerosols and dust), dynamic and radiative processes. These processes are mainly divided into large-scale and small-scale processes.

Atmospheric physics generally investigates phenomena at the largest scales; they are typical of the Earth as a system. At the largest scale, an exchange in the energy inputs and outputs needs to be considered in detail. The preliminary information about the system is solar energy, which arrives in the form of electromagnetic radiation. The Earth basically receives energy in the form of light and loses energy in the form of heat. Some of this terrestrial radiation is absorbed by our atmosphere, thus producing what is commonly referred to as the greenhouse effect, which demonstrates the link between atmospheric composition and energy transfer within the Earth's atmospheric system.

In this work, we do not concentrate on the largest scales in the atmosphere or on the dynamic of clouds that deal with airflow movements that create the preferred situations for the formation of clouds and precipitation.

We rather focus on microphysical processes, which are also central to the global

energy balance and, therefore, to the global temperatures and essential considerations for the formation of clouds. The most crucial process in this respect is the microphysical process, which deals with the growth of individual particles from the gas phase through condensation and smaller cloud particles through collision and coalescence. Before discussing the microphysical mechanism of the formation of the cloud particles, we will briefly describe the primary microstructural features of the clouds for the purpose of this thesis.

1.2 The primary microstructural features of clouds

The effect of turbulence on the microphysics of a cloud varies according to the evolution stage of the cloud. Most research has dealt with the estimation of the parameters that characterize clouds whose top is under the freezing level [6], Pruppacher and Klett, 1997, sections 2.1.3 and 14.5.2 [134]. This form of cloud constitutes a significant portion of the Earth's tropics. We here verify the understanding of the role of clouds on rainfall, which is considered about 30 percent throughout the world and nearly 70 percent at the Tropics [111]. This kind of cloud, in particular, carries wet air, aerosol particles, and liquid droplets are known as warm clouds.

In general, the microstructure of clouds is defined by the stratification of the temperature, the vapor content, cloud drop spectra, the liquid water content, and the vertical velocity. Since these quantities are the basic terms used to measure the properties of clouds, various instruments and practical tactics have been developed to measure them. The increasing power of computers, as well as better practices and observation strategies, allow a much more detailed study of these tactics to be obtained. State-of-the-art studies can provide knowledge on sections or subsections of the physics involved in laboratory studies or research throughout the world, using numerical simulations on machines capable of running high-performance computing (HPC). Mathematical and analytical analyses are usually limited by the high degree of complexity of such a system. Therefore, numerical/laboratory experiments and in-situ measurements play fundamental roles in the investigation of these phenomena.

It is generally assumed that the most appropriate technique to measure clouds is in-situ measurement using sensors and instruments, such as the Rosemount sensor, which is a fast response thermometer, or a dew-point hygrometer, which can be used to measure humidity. Johnsons-Williams' sensors are used to measure the liquid water concentration in a cloud. Other microstructure features of clouds, such as the vertical velocity and cloud drop spectra, are usually measured using accelerometers and forward scattering spectrometers.

It has been shown that these kinds of variations in the microstructure of clouds play a role that is at least as important as cloud formation and the lifetime of a

cloud. Clouds basically behave like energy traps in which internal Physico-chemical processes can develop energy as latent heat releases through nucleation and condensation of the water droplets or through turbulent energy amplification induced by unstable density stratification.

Clouds generally receive energy from various sources. The most critical source is acoustic gravitational waves propagating from below or above the layers in clouds. The second source comes from cosmic rays during their interaction with water droplets. Electromagnetic radiation from the Earth, or outside the atmosphere, also plays a role as a source from which energy is extracted. However, it is not yet feasible to measure or introduce these sources into numerical simulations. For example, compressibility should be included in a numerical simulation to account for internal acoustic and gravitational waves and baroclinic effects. However, techniques that are efficient in simulating clouds with relevant Mach number evanescent values have not yet been developed. The dynamics and lifetime of a cloud as a whole are closely linked to entrainment processes and subsequent turbulent mixing at their interface. Turbulent flows are well suited for mixing fluids over a wide range of length scales. Nevertheless, there are scenarios in which turbulence does not mix up a system. For example, if a fluid contains high-density particles, a turbulent flow can cause particle clustering. The particles "segregate" from the fluid and clump together and then tend to be unevenly distributed in a turbulent flow. Scientists have postulated that turbulence-induced particle clustering occurs in clouds, thereby causing raindrops to be pushed together and increasing the probability that two drops will collide and flow together. This droplet clustering has been observed in laboratory experiments and numerical simulations, but extrapolating the data to the much larger length scales of real clouds is difficult, as demonstrated by [2], [22], [10], [17], [31], [165], [166], [127], [68], [8] and [90].

Fully resolved numerical simulations [159] cannot cover the whole scale range involved in the dynamics of a turbulent cloud. Such simulations would require studies that parameterize the effect of the smaller turbulent eddies and of the microphysics of clouds in subgrid-scale models or other parameterizations [46]. Moreover, the complexity of multiscale dynamics is further increased at the cloud boundary. The air in the cloud at the aforementioned boundary forms a complexly shaped interface with water droplets (and ice crystals) and clear air. The additional coupling of the turbulent fields with the nonlinear thermodynamics of phase changes and droplet-droplet interactions leads to an environment with multiple feedbacks. Evaporation of the droplets causes a local evaporation cooling, which affects the liquid movement via buoyancy. This generates a fluid lowering movement at the cloud-clear air interface (see, e.g., [63], [151], [36]). Thus induced shear motion, in turn, influences droplet advection. Consequently, the interaction with small-scale turbulence and, thus, its evaporation is dominant. Droplets first form in clouds when gaseous water vapor condenses into a liquid. Cloud droplets have a radius of about 20 micrometers or less, and the concentration number of these cloud droplets varies for maritime

clouds, and continental clouds [134]. They are relatively light and closely follow the flow lines of the air stream. Cloud drops of this size have a lower tendency to hit other drops. However, after some time, cloud droplets become more significant and substantial in order to stay afloat and become raindrops with a diameter of more than 80 micrometers. Falling raindrops then grow on impact and merge with other drops [52].

Since there are so many cloud particles in a small shear area of the cloud, the simulating of each cloud droplet individually is somewhat complicated. For this reason, atmospheric models are set up to statistically represent the evolution of a particle population. The direct numerical simulations (DNSs) we have set up are able to resolve the turbulence down to the smallest eddy size, which allows us to investigate these aspects in an idealized environment and unravel the multiple feedbacks between small-scale turbulence and droplet dynamics. Such a configuration, which can be regarded as a paradigm for turbulence at the edge of an atmospheric cloud, is a shear-less layer or a shear-less mixed layer – one of the simplest arrangements of in-homogeneous turbulence. Such a layer is created when two homogeneous and turbulent sub-regions with different mean kinetic energies come together. This configuration has already been investigated in experiments, such as those in [14], [155], [147], [62], [137] and in the DNSs of [47], [107], [108], [7], [16], [3],[42], [44], [43].

In this study, we briefly consider the carry-over into cumulus clouds. For further details, we refer to [132], and [126], which proposed the approach chosen to model entrainment in cumulus clouds. This technique is a simple method that can be used to model entrainment in the dry plume of an isolated source. Marton suspected that lift and vertical velocity profiles are similar to altitude, but such an approach is not so successful for cloud dynamics for various reasons. For example, this approach is not able to simultaneously predict the vertical expansion and the liquid water content of a cloud [83].

Cloud droplets floating in turbulent clouds change the local environment to the order of magnitude of individual droplets in three ways: mass (condensation, evaporation), momentum (viscous resistance), and energy (latent heat). The local transformation of each droplet via these parameters can change the background airflow. For example, buoyancy effects are introduced by the phase transformation between water vapor in the air and the liquid water in the droplets. Therefore, the state of existence of these cloud droplets plays a decisive role in the dynamics of clouds (mainly due to the buoyancy effect). Consequently, the motion and size of cloud droplets are coupled with air turbulence. This is an important point when critical parameters, such as Reynolds' numbers, the energy dissipation rate, and/or velocity variations, are considered within air turbulence.

1.2.1 Interactions of aerosol-cloud droplet dynamics in a turbulent environment

On the basis of the previous explanation, it is possible to hypothesize that atmospheric aerosols, which are complicated multiphase systems, can indirectly control the Earth's radiative balance relevant to climate. The Earth's radiative balance has been controlled by aerosols in two ways: by acting as cloud condensation nuclei (CCN) or by scattering solar radiation. It has long been recognized that the main link between aerosols and cloud droplets, in the presence of the interactions between cloud microphysics and turbulent fluctuations, is the activation of CCN. CCN is generally the centers in which cloud droplets can form, and the range of sizes can be subdivided into three classes: Aitken nuclei (0.06-0.2 microns), large nuclei (0.2-2 microns), and giant nuclei (larger than 2 microns). Ambient relative humidity (saturation ratio), which leads aerosols to become cloud droplets, is assumed. The relative humidity of the ambient basically depends on the size and chemical composition of the particles, and the oscillation of the saturation ratio plays a crucial role in aerosol-cloud droplet interactions and in broadening the droplet size distributions (DSD).

In this study, we have focused on the size of cloud droplets, which range from 0.06 microns to 40 microns, and investigated the activation of CCN (Cloud Condensation Nuclei) in a turbulent environment. The effects of the cluster formation of cloud droplets have been discussed in detail.

The activation of CCN in this analysis depends to a great extent on the regions in which the aerosols are located. The activation regions in a turbulent environment can basically be subdivided into three different regions, which are identified by considering the distribution of the relative humidity. In this investigation, we have expected that the cloud droplets would have different supersaturations, depending on their location. This assumption was first pointed out by Srivastava [33], who compared macroscopic supersaturation and microscopic supersaturation. The intensity of supersaturation fluctuations is altered by varying the temperature and vapor pressure gradient. The temperature and the relative humidity are the most important parameters that control the growth and evaporation process of cloud droplets. These gradients are responsible for the molecular transport of moisture and energy [11]. The first multiphase DNS simulation of the cloud microscale was reported by Vaillancourt [11]. He studied homogeneous isotropic turbulence, which allows cloud droplets to grow as a result of the diffusion of water vapor. He included droplet sedimentation in his study, which was in contrast to previous studies on particle-laden turbulent flows (see Eaton & Fessler) [88].

Some years later, Lanotte [145], reported similar DNS simulation results. He performed simulations with the same dissipation rate as Vaillancourt, but with a high Reynold's number and an increased number of drops carried by the flow. In 2005, Boffetta and Celani [53] performed simulations with the same dynamic frame

as Vaillancourt and Lanotte and Sidin [145], but came to dramatically different conclusions. In particular, he found a dramatic increase in the width of the drop spectrum. This difference emerged because he had neglected the presence of latent heat. Such an omission leads to unrealistically large supersaturation fluctuations that are not suitable for typical cloud conditions. Two years later, in 2007, Celani [26] corrected some aspects of his work, whereby he depicted the mixing between a cloud and clear air. In the following years, Heus and Jonker [151], Holzner [106], Gerashchenko and Good and Warhaft [56]] investigated a deeper understanding of the mixing in the cloud and clear air interface in more detail. A significant development was obtained carried out by [1] and Ireland, and Collins [74]], who concentrated on the use of laboratory experiments. They focused their studies on the dynamics of inertial particles at the turbulence-turbulence interface (TTI). Previous studies by Tordella [43] focused on turbulent transport across the interface between higher and lower-level turbulence. Tordella did not consider phase changes and neglected the latent heat released during condensation and evaporation cooling. In all these studies, the authors considered the growth of particles under different aspects. For example, Vaillancourt [11], Smolarkiewicz [103], Lanotte, Seminara, and Toschi [145] and Gotoh, Suehiro and Saito [150] studied the growth of particles as a result of condensation, while the growth of particles as a result of collision and coalescence was studied for the first time by Arenberg [38], who found that turbulence can increase the relative motion and collision rate between cloud droplets. This scenario was also pursued by Gabilly [5] and some years later by East and Marshall [130].

In 1956, Saffman & Turner [59] developed a theoretical expression for the turbulence collision rate. Reuter [161] introduced a stochastic model. In his study, he emphasized the point that turbulent fluctuations could amplify the geometric collision rate with respect to the results by Saffman & Turner. The authors of [28], [29], and [144] worked on another aspect, that is, on the effect of turbulent motion on the collision efficiency of cloud droplets. This aspect of particle growth was also investigated by Kumar [19], [20] and more recently by [160], Onishi, Matsuda, Takahashi [133], [61] and [60]. The authors showed how turbulence and the relative velocity between inertial drops influence collision efficiency in the neighborhood of a fluid environment. Consequently, they emphasized that the collision and coalescence rates broaden the particle size distribution. Perrin and Jonker [50] have recently investigated Lagrangian droplet dynamics at the cloud-clear air interface. This is a critical point in the research on cloud turbulence, which shows that turbulence-particle interactions can dramatically increase two important criteria: the collision rate and collision efficiency of cloud droplets.

Chapter 2

Study of the warm cloud and clear-air interface

2.1 Computational Methodology and Simulation Set up

The calculation methods and the numerical formulation used in the context of the objectives of the present work are discussed in the present chapter. This is followed by a brief description of the governing equations of an incompressible flow, the turbulence concepts, and the simulation setup, as well as the specific methods used in this thesis.

2.1.1 Numerical set up for the simulated cloud system at an air turbulent interface

In general, transitional situation systems are considered less understandable in the atmospheric physics field and present some unique and interesting phenomena. The modeling of such a diversity of systems requires powerful and capable machines, and this phenomenon plays a critical role in the environmental and technological worlds. Our three-dimensional direct numerical simulations (DNSs) have been focused on parts of warm cumulus clouds (ice-free clouds) that could reveal the transient systems and their structures. Warm cumulus clouds are mostly ice-free, and carry moist air, aerosols, and liquid droplets, and since we have not considered ice structures, this type of cloud can be considered useful for our studies.

In our study, we have emphasized the progress that has been made in the identification of cloud boundaries. Cloud boundaries are also known as interfaces. It is possible to represent cloud interfaces by resorting to a **shear-less turbulent mixing layer** in a **decaying temporal flow**. A decaying temporal flow is essentially a flow in which the propagation of turbulence is caused by oscillations

of the velocity and pressure fields. In short, a shear-less turbulent mixing layer is a simple case of inhomogeneous turbulence whereby the transport effects can be studied independently of other influences. The formation of these layers is due to the interaction of two initially homogeneous isotropic turbulent cubes (HIT) with different (i) turbulent kinetic energy levels [27],[16], [42], [44], [43], (ii) temperature [109], [19] and (iii) inertial particles [74] also in presence of supersaturation levels [119], but with identical spectral shapes. This flow was studied experimentally in the DNS of [14] and [147], where only mono-phase fluid turbulence was considered, to configurations where inertial particles were present [57] and [142].

The computational domain is set with two cubes attached in such a way that the cloud is located on top. The size of the domain in which we perform the calculation is $0.5m \times 0.5m \times 1m$ and the calculation area is discretized using $512 \times 512 \times 1024$ grid points. The initial zero-mean, homogenous and isotropic turbulent fields are generated inside the cubes. This refers to a flow in which there are no external forces to push the flow. Reference can be made to Figure 1 (a) for the schematic of a flow inside a simulation domain, while Figure 1 (b) represents a three-dimensional turbulent kinetic energy spectrum of atmospheric turbulence. It is an observation for the infield measurement campaigns. The dark blue part on the right is part of a spectrum that is relevant for the present simulations; please, see Figure 1 for details 2.1.

Turbulent mixing has in particular been considered when the substance is assumed as a scalar, and the mixing process does not affect the flow itself. Basically, when the substances are passive, they do not have any dynamical effects on the fluid motion. This is the paradigm of most influence on turbulent mixing. We discuss, within this paradigm, how a turbulent mixing state is based on the Reynolds number of the flow and the Schmidt number of the scalar, and we point out some fundamental aspects of turbulent mixing that make it difficult to treat quantitatively and summarize a number of ideas that help us admire its physics in a variety of circumstances. It is generally accepted that this type of flow is a good example, for a number of reasonable reasons, to study its effects in our DNSs. The most crucial reason is that, through such a flow, it is possible to represent a real scenario in nature. For example, the inherent non-stationarity of such a flow, and the ability to easily include an integral scale gradient parallel to that of turbulent kinetic energy and enstrophy in order to account for anisotropy can even be extended to small scales in a highly explicit way. Fundamentally, all numerical experiments discussed in this work have been set up to simulate the turbulent shear-less mixing unsteady process, which can take place in any portion of warm cumulus clouds.

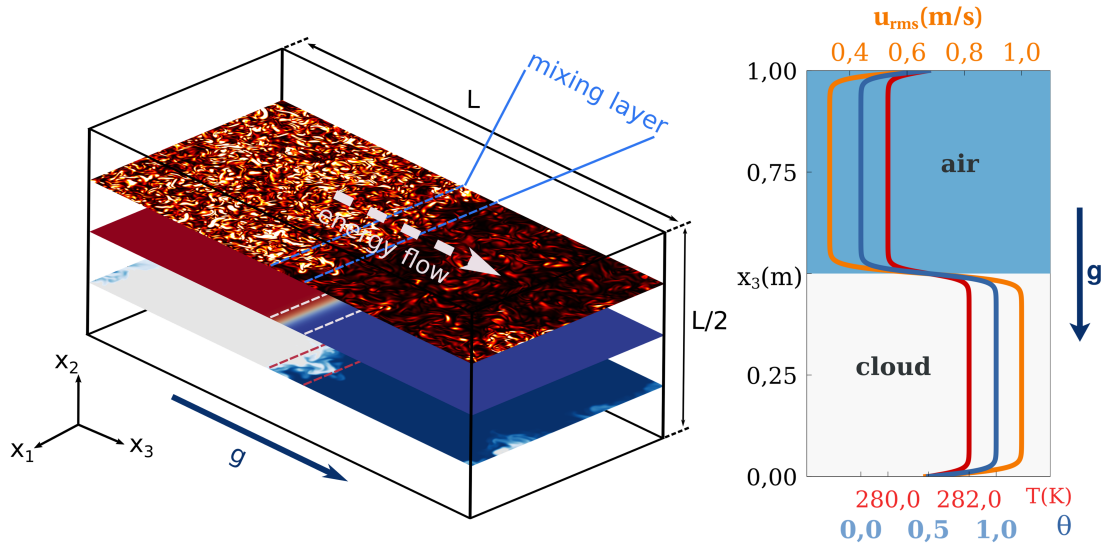

(a) Schematics of a flow inside the simulation domain. The energy flow is from left to right along the x_3 direction. $E_1/E_2 = 10$.

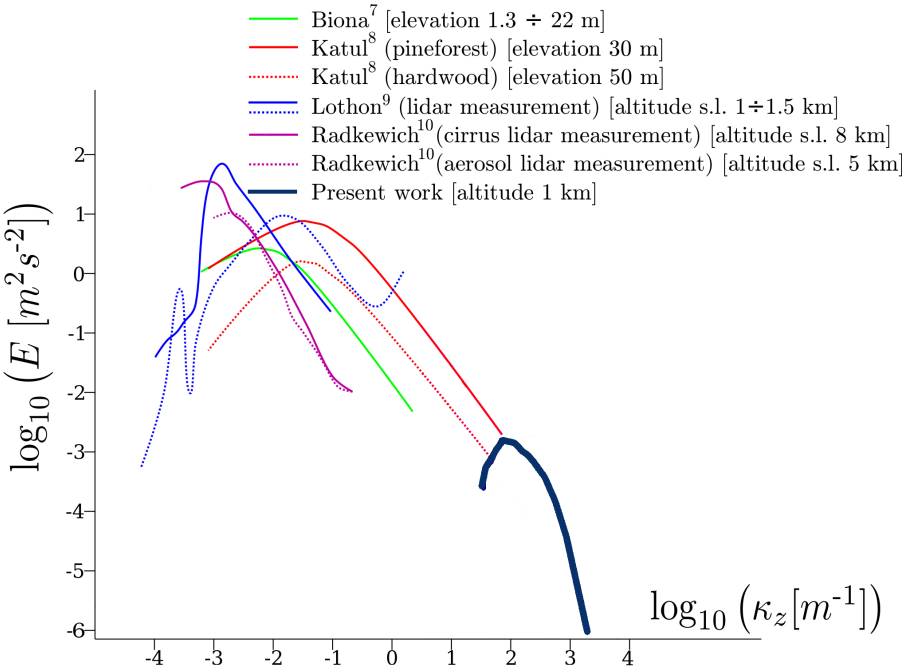

(b) Three-dimensional turbulent kinetic energy spectrum of the atmospheric turbulence observed in a set of infield measurements. Dark blue represents the part of the spectrum that is relevant to the present simulations.

Figure 2.1: **Physical system and spectral physical properties in cloud - clear air transient interaction**

The periodic boundary conditions of the flow have been implemented, and the direction of the energy flow has been observed along the x_3 direction. From now on, the cube in the lower half will be referred to as a cloud region with higher turbulent kinetic energy, and the other half of the cube will be referred to as the clear region with lower turbulent kinetic energy. So the energy flow is therefore from left to right along the x_3 direction and has a ratio of 10. In general, the region of the cloud in our simulation field represents the mixing portion. One of the essential parameters for such a mixing phenomenon, which is responsible for all turbulent transport methods and for their propagation, is the fluctuation of the pressure and velocity fields. The oscillations of these parameters are responsible for the energy transport across the mixing layer. The key point is to comprehend how the mixing of a cloud and clear air develops as turbulence, and how the thermodynamics interacts through phase changes, and, finally, how the cloud droplets react to such variations.

In our DNSs, the initial root mean square velocity is 0.1 ms^{-1}, and the initial dissipation rate is about 500 cm^2s^{-3}. The Kolmogorov scale, which is the smallest micro-scale in turbulent flow η_k, is about 1 mm. (When considering the Kolmogorov scale, viscosity dominates, and the turbulent kinetic energy is converted into heat). This Kolmogorov scale is typical of cumulus clouds. Since the dissipation rate and turbulence intensity decay over time, the Kolmogorov scale grows. This process leads to a grid size in the physical domain of 1 mm; see Figure 2.2 (e). As in Figure 2.2, the top left panel shows the turbulent energy excess with respect to the clear-air part, normalized to the difference between the two regions ($E_1 = 10 \cdot E_2$) at $t = 0$; please, see Figure 2.2. The turbulent kinetic energy, the Liquid Water Content (LWC), buoyancy, and supersaturation mean value along the inhomogeneous direction have all been represented. All the quantities are in three stages in the last few seconds of the temporal evolution ($\tau_0 = 0.42$ s).

Looking at Figure 2.2(b), a peak in the turbulent kinetic energy within the mixing region— a sort of peaky sublayer— is shown increasing in time. The high-turbulent energy region inside the cloud is separated from the low-energy clear air by a secondary gradient. This aspect will be commented in detail in Chapter 4.

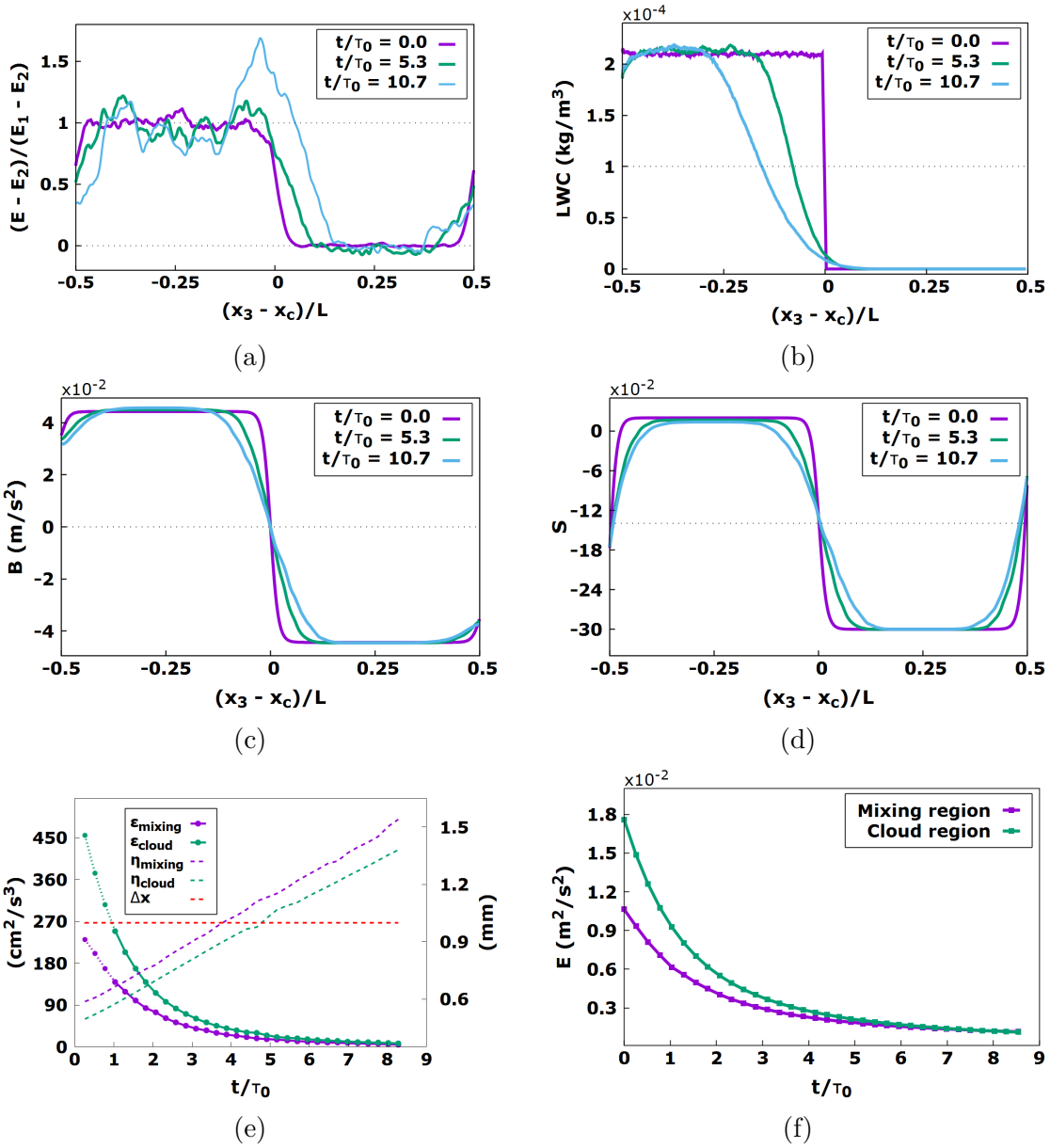

Figure 2.2: **Mean values of the turbulent kinetic energy, Liquid Water Content (LW C), buoyancy, and supersaturation along the inhomogeneous direction. The quantities are in three stages along the temporal evolution which, in physical non-normalized terms, last a few seconds ($\tau_0 = 0.42$ s, see Table 2).**

2.2 Relevant equations for the flow field

The governing equations in our overview are incompressible Navier-Stokes' equations, with the Boussinesq approximation (in which density differences are ignored, unless they occur as terms multiplied by g, that is, the acceleration due to gravity) for both temperature and vapor density, and active scalar transport equations for water vapor and thermal energy. We have specifically focused on an isochoric flow since, in fluid mechanics, such a flow refers to a flow in which the material density within a fluid package is constant.

The water droplets of the inertial cloud are represented by a Lagrangian approach, which includes Stokes' resistance and gravitational settling. This representation is coupled to the water vapor and temperature equations via their respective evaporation-condensation source terms. We follow the **drop position, velocity, and radius**. However, this is only a **one-way coupling approach** and does not include any feedback on drops to the flow field of the air stream. This is basically a combination of the Eulerian description of the turbulent velocity, temperature, and water vapor fields with a Lagrangian description of the ensemble of cloud droplets.

In parallel with other earlier direct numerical simulation Navier Stokes models, such as those in Kumar et al. (2014) [19], Gotzfried et al. (2017) [119], our code is solves the following equations:

$$\frac{\partial u_i}{\partial x_i} = 0 \tag{2.1}$$

$$\frac{\partial u_i}{\partial t} + u_j \frac{\partial u_i}{\partial x_j} = -\frac{1}{\rho_0}\frac{\partial p}{\partial x_i} + \nu \frac{\partial^2 u_i}{\partial x_j^2} - B\delta_{zi}, \tag{2.2}$$

$$\frac{\partial T}{\partial t} + u_j \frac{\partial T}{\partial x_j} = \kappa \frac{\partial^2 T}{\partial x_j^2} + \frac{L}{c_p} C_d \tag{2.3}$$

$$\frac{\partial q_v}{\partial t} + \boldsymbol{u}_j \frac{\partial q_v}{\partial x_j} = \kappa_v \frac{\partial^2 q_v}{\partial x_j^2} - C_d \tag{2.4}$$

Where the vapor mixing ratio $q_v(x_j, t)$ is given by the ratio of the mass of water vapor to the mass of dry air. The turbulent velocity field, $u_i(x_j, t)$, the temperature field, $T(x_j, t)$, the pressure field, $p(x_j, t)$ and the vapor mixing ratio, $q_v(x_j, t)$ are given from the above equations. The i, j, k indices are used in the Einstein convention context, but x_i, x_j, and x_k are often implicitly replaced by (x, y, z). The ν in these equations is the kinematic viscosity of air, while g is the acceleration due to gravity, ρ_0 is the reference value for the density of dry air at 1000 m above sea level, c_p is the specific heat at constant pressure, L is the latent heat of evaporation of water ($2.510^6 Jkg^{-1}$), k is the temperature diffusivity, D is the diffusivity of the vapour mixing ratio. All these quantities are summarized in Tables 2.1 and 2.2.

Fundamentally, the Boussinesq approximation is valid under the assumption of small perturbations of the local temperature and vapor density fields, while C_d and B are the condensation rate field and the buoyancy field, respectively.

The buoyancy field, B, in the momentum equation depends on the temperature field $T(x_j, t)$ and the vapor mixing ratio field $q_v(x_j, t)$), and is defined as:

$$B = g[T'/ < T > +\alpha q_v'] \tag{2.5}$$

where $\alpha = M_a/M_v - 1 = 0.608$ and M_a and M_v are the molar masses of dry air and steam respectively, [71].

Generally the volume mean value $<>^{\cdot}$ is introduced and the temperature variations are given by

$$T'(x_j, t) = T(x_j, t) - < T(t) + T_{bg} > \tag{2.6}$$

Where the T_{bg} is a constant in time background temperature equal to $T_0 + Gz$. The vapor mixing ratio fluctuations is given by

$$q_v'(x_j, t) = q_v(x_j, t) - < q_v(t) > \tag{2.7}$$

The droplets in this model influence the development of liquid movement through the condensation term C_d in 2.3 and 2.4. The condensation rate field $C_d = C_d(x_i, t)$ is defined as the time derivative of the mass of the liquid m_l within each of the grid cells with the volume Δ^3 surrounding the grid point x_i, relative to the mass of dry air m_a, ([11]).

Since cloud droplets are advected in the turbulent flow, C_d should be determined in the Lagrangian reference frame, which is used for the liquid-water mixing ratio described below. For use in equations 2.3 and 2.4, C_d must, of course, be rendered again in the Eulerian reference frame. The condensation rate field is determined as:

$$C_d(x_i, t) = \frac{1}{m_a}\frac{dm_l(x_i, t)}{dt} = \frac{4\pi\rho_l K_s}{\rho_0 \Delta^3}\sum_{j=1}^{N_\Delta} R_j(t) S(X_j(t), t) \tag{2.8}$$

where m_a and m_l are the air mass and liquid mass per grid cell, ρ_l is the density of water, ρ_0 is the reference density of dry air, $R_j(t)$ and $\boldsymbol{X}_j(t)$ are the radius and vector space coordinate of the $j-th$ drop, respectively. N_Δ represents the number of drops inside each grid cell, S is supersaturation described below, and K_s is a temperature and pressure dependent diffusion coefficient that includes the self-limiting effects of latent heat release.

This diffusion coefficient is considered to be constant in literature, for typical warm cloud conditions in which the characteristic heat flux due to latent heating from a small variation in the droplet temperature is of the same order as the heat

flux due to thermal conduction for the same temperature difference, because its temperature dependence is weak (K_s value in m^2 s^{-1} ranges from $5.07 \cdot 10^{-11}$ at $T = 270$ K, to $1.17 \cdot 10^{-10}$ at $T = 293$ K), see for instance [135], [150], [19]).

We used the $8.6 \cdot 10^{-11}$ m^2 s^{-1} value in relation to our volume averaged initial temperature of 281 K. The interpolation of the Eulerian field values at grid positions to the position occupied by the water droplets inside the cell is done via second-order Lagrange polynomials. An inverse procedure is then used to calculate the condensation rate, which is determined at the first step of each droplet position and then relocated to the closest eight grid vertices. The collision between droplets is supposed to occur when the distance between the droplet centers is equal to or below the sum of their radii. This explanation is related to a collision being completely inelastic. However, it is important to mention that coalescence happens after the collision of the particles, which is an important point in our simulations.

2.3 Relevant equations for Lagrangian droplet dynamics

Our three-dimensional direct numerical simulations (DNSs) have considered cloud droplets as **point particles**. This hypothesis emphasizes that no droplet-droplet interaction is considered. This supports the assumption that cloud droplets are always smaller than the grid size. The DNS simulations are performed using a mixed Eulerian-Lagrange approach, which combines an Eulerian description of turbulent velocity, temperature, and water vapor fields with a Lagrangian cloud droplet ensemble. The liquid water component in the Lagrangian description is modeled as a Lagrangian ensemble of N -point-like droplets. The flow is modeled by solving the usual Euler equations, and then representative droplets are followed using the Lagrangian approach with conventional gas-particle coupling. Two different initial size distributions were considered in these DNS simulations: **a monodisperse initial distribution of particles** with **15 μm** sized particles and **a polydisperse initial distribution** of **0.6 μm to 40 μm** droplet radii.

It is here worth mentioning that, compared to what we applied for the submitted condensation rates and Euler's flow field quantities, it is necessary to proceed numerically at the drop positions for Lagrange equations. The direct influence of the liquid drop resistance on the velocity field has been neglected in this overview, as it has been shown that the drops have no significant influence on the flow fields, i.e., on the buoyancy term in the momentum equation. The feedback is rather indirect and is limited to the coupling of the temperature field with the velocity field and the vapor mixing ratio with the condensation rate. The rationale behind such a position is that Stokes' drop numbers (Reynolds' drop number of much less than 1) and the loading of the liquid mass are insignificant. By applying the above assumption to each cloud drop, the complete equations of motion of the particles

under turbulence, which are here called Lagrangian evolutions for the i-th cloud drop, can be reduced to:

$$\frac{d\boldsymbol{X}_i}{dt} = \boldsymbol{v}_{p_i} \tag{2.9}$$

$$\frac{d\boldsymbol{v}_{p_i}}{dt} = \frac{\boldsymbol{u}_i(\boldsymbol{X}_i, t) - \boldsymbol{v}_{p_i}}{\tau_i} + \left(1 - \frac{\rho_a}{\rho_w}\right)\boldsymbol{g}, \tag{2.10}$$

where $\mathbf{u}(\mathbf{x_i}, \mathbf{t})$ denotes the flow velocity vector at the position of the i-th particle, where x_i represents the position vector of each drop, $\mathbf{v_{p_i}}$ is the drop velocity; ρ_w, ρ_a, are the densities of water and air, respectively, and τ_i is the drop reaction time, which is the characteristic reaction time of the particle to changes in the flow. This time scale is defined by the Stokes resistance coefficient and is adapted to the dynamic development of the drop radius, $R_i = R(\mathbf{X}_i, t)$. Assuming Stokes' drag, the relaxation time of each cloud drop is given as follows.

$$\tau_i = \frac{2}{9}\frac{\rho_w}{\rho_a}\frac{R_i(\boldsymbol{X}_i, t)^2}{\nu}. \tag{2.11}$$

where ν is the air kinematic viscosity. It is better to mention that all these Lagrangian evolution equations are proved in a case where the density of each droplet is much higher than the density of the air and the droplet radius is small enough to compare to the Kolmogorov scale $\eta = (\frac{\nu^3}{<\epsilon>})^{\frac{1}{4}}$ of the flow.

As said before, the response of the droplets depends on the Stokes number, which is a key parameter to govern the effects of turbulence on the collision rate. It defines as

$$St = \tau_p/\tau_\eta \tag{2.12}$$

where τ_η is the Kolmogorov time scale and defines as

$$\tau_\eta = (\frac{\nu}{<\epsilon>})^{\frac{1}{2}} \tag{2.13}$$

This dimensionless number has a great influence on our investigation since it is a key point to describe the relative inertia and settling velocity. In general, the reaction of the particles was studied for three conditions. If the particles react immediately to an acceleration of a flow that represents a small Stokes number, the cloud particles are considered tracers. If the particles react very slowly to each fluctuation of the flow, which occurs for a large Stokes number, it can be deduced that the cloud particles cannot sense these flow variations. The third and most important case is when there is a strong interaction between the flow and the particles. In this situation, the Stokes number is of the order of one. More importantly, this non-dimensional parameter can vary by more than one order of magnitude for each size range. The rationale behind this position depends on the smallness of the drop Reynolds number. In fact, for radii in the range 0.6 – 30

μm, the initial transient values of Stokes' numbers are in [0.02–0.07], while the end of transient values is in the range [0.002–0.066]. In a situation implying droplet Reynolds numbers well below.

In our simulation of the droplet model, we ignored some aspects that can have a significant impact, even when the Reynolds number is below unity. In particular, we neglected the Faxen correction related to the effect of velocity curvature on the drag, added mass, pressure gradient term, and the Basset history forces. These forces are negligible under our simulation condition, where the gas and particle density ratio is of the order of 10^{-3}, as it has already been shown in many studies, [153], [94].

In this study, droplet growth is determined by means of three processes: condensation, evaporation, and complete coalescence after the collision. Therefore, the particle growth numerical model should be coupled with the Lagrangian tracking of each individual droplet. As far as the growth by condensation/evaporation model is concerned, we reproduced a particle growth model according to the general dynamics described by Kohler's theory, which includes the spontaneous growth of cloud condensation nuclei (CCN) in cloud droplets under supersaturated water vapor conditions, see ([64], [49] [134], [65]). A simplified form of this model was also used by [11], [19], [150], [119] and [167] for larger particles than CCN. It should here be noted that other studies that resorted to direct numerical simulations did not take into account the presence of the CCN activation process. In principle, when the droplets are attracted by the liquid, they can grow or evaporate in response to the local vapor field. The vapor mixing ratio is coupled with the growing decay of the droplets by means of supersaturation S, which is defined by the vapor mixing ratio and the saturation vapor mixing ratio as:

$$S\left((\boldsymbol{X})_i, t\right) = \frac{q_v((\boldsymbol{X})_i, t)}{q_{vs}(T)} - 1 \tag{2.14}$$

The saturation vapor mixing ratio $q_{vs}(T)$ at the droplet position is obtained from the Tetens' formula ([118]):

$$q_{vs}((\boldsymbol{X})_i, t) = \frac{e_s(T)}{R_v \rho_0 T} = \epsilon_0 \frac{610.78}{\rho_0 T} exp[17.63 \frac{T - 272.16}{T - 35.86}] \tag{2.15}$$

where e_s is the saturation pressure and $\epsilon_0 = R_a/R_v \sim 0.62$, R_a and R_v are the gas constants for dry air and water vapor, respectively. See also, for temperatures above 273.16 K, [78]. The curvature of the droplet surface induces the so-called Kelvin effect on the evaporation rate. The degree of bonding that exists between any water molecule on the surface and its neighbors is reduced by the curvature of the surface. As a result, a water molecule is more likely to escape from a liquid and enter the vapor phase. This increases the evaporation rate. The greater the curvature is, the greater the probability that the water molecules on the surface can

escape. Less energy is in fact required to remove a molecule from a curved surface than from a flat surface. Furthermore, the atmosphere is not clean because there are many other types of solid, soft or liquid particles in the atmosphere, in addition to water droplets. Some of them are hydrophilic and water-soluble. The effect of soluble CCN on the water evaporation rate is called the Raoult effect. The Kelvin and Raoult effects, curvature, and solute effects can be included in the model for droplet growth. We followed [69] and [73] and [71] and wrote:

$$R_i \frac{dR_i}{dt} = K_s \left(S - \frac{A}{R_i} + \frac{B r_d^3}{R_i^3} \right) \tag{2.16}$$

Here above the diffusion coefficient K_s was introduced in relation to the condensation rate field C_d, see 2.8. The constant terms A and B represent the curvature and solution effects, respectively, while r_d represents the dry particle radius. The term A depends directly on the surface tension of water ($\sigma_w = 72.75 \cdot 10^{-7} (\text{J cm}^{-2})$), and, naturally, on the density, the gas constant for water vapor, and the local temperature of the air phase. On the other hand, B depends not only on the water and the molecular weight of water but also on the mass of the solute, its molecular weight, and the total number of ions into which the solute dissociates. Here, we followed [72] and assumed that the solute dissolved in each drop is an inorganic hygroscopic substance, like ammonium sulfate, sulfuric acid, or lithium chloride, which have solubility parameter B close to 0.7 and an accumulation mode with modal diameters r_d in the range of 10 to 50 nano-meters (fine mode, observed North Atlantic marine air masses, see [79] and [69] and [15], [70]).

We obtained $A = 1.15 \cdot 10^{-7}$ cm and $B = 0.7 \cdot 10^{-18}$ cm^3 for an almost constant air phase temperature close to 281 K. A is the Kelvin coefficient, and k is the hygroscopic parameter, which is defined as:

$$A = \frac{2 \mathcal{M}_w \sigma}{RT \rho_w} \quad [m] \tag{2.17}$$

Where σ is surface tension, $\mathcal{M}_w$ is molecular mass of water, R is the ideal gas constant for water vapor, T is the temperature, and ρ_w is the density of the liquid water.

2.4 Initial and boundary conditions applied for the flow and scalar fields

As previously mentioned, the simplest anisotropic turbulent flow in our DNS has been produced from the interaction of two homogeneous isotropic time-decaying turbulence fields. The most important aspect that characterizes this flow is in absence of a mean shear, and, therefore, leaving aside the injection of turbulent kinetic energy associated with the eventual presence of an unstable stratification, when no turbulent kinetic energy is generated due to the unique presence of a mean shear flow. Thus, the interactions between the two homogeneous regions are only the result of fluctuating pressure and velocity fields. In this investigation, the two interacting flow fields are identical, except for the turbulent kinetic energy content, and this flow therefore only differs from a homogeneous and isotropic flow as a result of the presence of two turbulent kinetic energy levels. A ratio (i.e., a gradient) of the turbulent kinetic energy is established across the interface which divides the two regions. Since it can be shown that the integral length scale of a turbulence field can be independent of its turbulent kinetic energy, it is possible to numerically obtain inhomogeneity in the turbulent kinetic energy of two HIT fields while maintaining homogeneity in the length scale [85].

The computational domain is a parallelepiped with periodic boundary conditions in all directions; see Figure 2.1 panel (a).

This parallelepiped has an aspect ratio of two, and, in dimensionless variables, its size is, therefore, 2π in the x_1 and x_2 directions and 4π in the x_3 direction. The Navier-Stokes and passive scalar equations are solved in this domain with a fully dealiased (3/2 rule) Fourier-Galerkin pseudospectral method. The time integration is performed with an explicit fourth-order Runge-Kutta scheme. A parallelized version of the velocity field code is presented in [107]. A short manual of the code and further details are also available in the Software section (Incompressible Turbulent Flows) on the `www.polito.philofluid.it`.

The initial conditions for this flow are created from two homogeneous and isotropic fields generated in a $(2\pi)^3$ cubic domain as the superposition of Fourier modes with random phases and amplitude set to create a prescribed three-dimensional spectrum, with a κ^2 shape for low wavenumbers and a $\kappa^{-5/3}$ shape in the inertial range. Both fields are then extended to generate the initial condition of the flow by periodicity in the x_3 direction to span the entire final $(2\pi)^2 \times (4\pi)$ parallelepiped domain. Each velocity field is also multiplied by a constant, and a non-unity energy ratio is thus created between them but the same spectra are kept so that the integral scales remain unchanged. Finally, a hyperbolic tangent weighting function has been applied in order to create a field with a smooth transition between the two halves of the domain with different turbulent kinetic energy over a thin layer:

$$\boldsymbol{u}(\boldsymbol{x}) = \boldsymbol{u}_1(\boldsymbol{x})p(x_3) + \boldsymbol{u}_2(\boldsymbol{x})(1 - p(x_3)) \tag{2.18}$$

where the 1 and 2 suffixes denote the high-energy or low-energy side of the cloud interface model, respectively. The weighting function, $p(x_3)$, which operates in the inhomogeneous x_3 direction, is defined as:

$$p(x_3) = \frac{1}{2}\left[1 + \tanh\left(a\frac{x_3}{L}\right)\tanh\left(a\frac{x_3 - L/2}{L}\right)\tanh\left(a\frac{x_3 - L}{L}\right)\right]. \tag{2.19}$$

where L is the width of the computational domain in the x_3 direction.

Function p allows a smooth transition to take place between the two regions under the initial conditions, thereby avoiding any discontinuity. The constant a in (2.19) determines the initial width of the interface layer between the two regions, which then becomes the mixing layer. A conventional thickness Δ can be defined, in order to have a quantitative measure of the thickness of the mixing layer, as the distance between the points with normalized energy values of 0.25 and 0.75. When the low energy side is mapped to zero and the high energy side to one. In other words, by defining normalized energy as:

$$E(t, x_3) = \langle u_i' u_i' \rangle / 2 \tag{2.20}$$

which is function of time in x_3 direction, the thickness is defined as:

$$\Delta(t) = x_h(t) - x_\ell(t) \tag{2.21}$$

where $x_h(t)$ and $x_\ell(t)$ are the points in which $\mathcal{E}(t, x_h) = 0.75$ and $\mathcal{E}(t, x_\ell) = 0.25$. If $a = 12\pi$ is chosen, the initial δ/L ratio is about 0.026; such a value is chosen so that the initial thickness is large enough to be resolved, but small enough to have large areas of homogeneous turbulence during the simulations.

The same technique is used to generate the periodic temperature and water mixing ratio fields, which are taken as non-fluctuating fields at the initial times (i.e. $T_1(\boldsymbol{x})$, $T_2(\boldsymbol{x})$, while $q_1(\boldsymbol{x})$ and $q_1(\boldsymbol{x})$ in equation (2.18) are uniform and not randomly generated). Reference can be made to Figure 1 on the right side of the panel (a) for a sketch of the mean profiles of the temperature, water mixing ratio, and air velocity root mean square. The tests were performed for regions with $4\pi \times (2\pi)^2$ dimensions and $512 \times 512 \times 1024$ grid points and with an initial mixture layer representing 1/40 of the inhomogeneous dimension (the largest grid dimension in the inhomogeneous mixture direction).

The three-dimensional spectra of the turbulent kinetic energy of the homogeneous, turbulent high-energy region of our system (dark blue line ranging from $k_3 = 25$ to $k_3 = 1570$ [m^{-1}]) are shown in Figure 2.1, panel (b). This region represents a small part of the cloud that interacts with the clear air above. This spectrum is compared in the figure with a few three-dimensional spectra obtained from field campaigns in the lower atmosphere. These measurements range from a few meters up to a few kilometers in altitude and extend over the Earth's surface with a linear dimension of the same order as the atmospheric turbulence macroscale. Tables 2.1

and 2.2 contain all the parameters used in the here presented Direct Numerical Simulations. The relevant physical and thermodynamic constants are summarized in Table 2.1, while information on the domain specifications, computational grid structure, turbulence scales, field control parameters, and water drop population is presented in Table 2.2.

In these kinds of simulations, the fields necessary for the description of turbulence convection are the velocity field, the temperature field, and the pressure field. A synthetic divergence-free field is implemented with a -1.67 slope power spectrum in the inertial range and an exponential tail in the dissipation range (random phases) as the initial condition of the velocity field, and the initial dissipation of the cloud region is set at $\epsilon \approx 500$ cm^2/s^3 after generating the synthetic field. The field was allowed to evolve for one eddy turnover time (1100 iterations) until it reached a dissipation of $\epsilon \approx 130$ cm^2/s^3. This field was then used as an initial condition. We set an energy ratio of 10 between the cloud and clear air regions as well as different temperatures and supersaturation levels, see Table 2.1 for details.

Table 2.1: **List of the thermodynamic constants and flow field parameters and their corresponding values in the present DNS**

Quantity	**Symbol**	**Value**	**Unit**
Latent heat of evaporation	$\mathcal{L}$	$2.48 \cdot 10^6$	$\mathrm{J\,kg^{-1}}$
Heat capacity of the air at constant pressure	c_p	1005	$\mathrm{J\,kg^{-1}\,K^{-1}}$
Gravitational acceleration	g	9.81	$\mathrm{m/s^2}$
Gas constant for water vapour	R_v	461.5	$\mathrm{J\,kg^{-1}\,K}$
Gas constant for air	R_a	286.7	$\mathrm{J\,kg^{-1}\,K}$
Diffusivity of water vapour	κ_v	$2.52 \cdot 10^{-5}$	$\mathrm{m^2\,s^{-1}}$
Thermal conductivity of dry air	κ	$2.5 \cdot 10^{-2}$	$\mathrm{J\,K^{-1}\,m^{-1}\,s^{-1}}$
Density of liquid water	ρ_l	1000	$\mathrm{kg\,m^3}$
Dry air density, altitude 1000 m	ρ_0	1.11	$\mathrm{kg\,m^{-3}}$
Reference kinematic viscosity	ν	$1.399 \cdot 10^{-5}$	$\mathrm{m^2\,s^{-1}}$
Entire domain average temperature	T_0	281.16	K
Temperature in cloud region	T_1	282.16	K
Temperature in clear air region	T_2	280.16	K
Background temperature gradient	G	-2	K/m
Diffusion coefficient	K_s	$8.6 \cdot 10^{-11}$	$\mathrm{m^2\ s^{-1}}$
Accumulation diameter	r_d	$0.01 \cdot 10^{-6}$	m
Kelvin droplet curvature constant	A	$1.15 \cdot 10^9$	m
Raoult solubility parameter for inorganic hygroscopic substances, like Ammonium sulfate, Lithium chloride, ...	B	0.710^{-18}	cm^3
Initial relative humidity inside cloud	S (cloud)	1.02	-
Initial relative humidity inside clear air	S (clear air)	0.7	-
Saturation vapor mixing ratio at T_1	q_{vs}(cloud)	$0.79 \cdot 10^{-2}$	$\mathrm{kg\,m^{-3}}$
Saturation vapor mixing ratio at T_2	q_{vs}(clear air)	$0.69 \cdot 10^{-2}$	$\mathrm{kg\,m^{-3}}$
Water saturation pressure at $T_1 = 281$	e_s	1.061	kPa
Molar mass of air	m_{air}	28.96	$\mathrm{kg\,mol^{-1}}$
Molar mass of water	m_v	18	$\mathrm{kg\,mol^{-1}}$
Initial liquid water content	LWC	$7.9 \cdot 10^{-4}$	$\mathrm{kg/m^3}$

Table 2.2: **List of the parameters used for the direct numerical simulation hosting of unstable cloud-clear interface of the monodisperse and polydisperse distribution of water droplets**

Quantity	Symbol	Value	Unit
Simulation domain size	$L_{x_1} \cdot L_{x_2} \cdot L_{x_3}$	$0.512 \cdot 0.512 \cdot 1.024$	m^3
Simulation domain discretization	$N_1 \cdot N_2 \cdot N_3$	$512 \cdot 512 \cdot 1024$	
Simulation grid step	Δx	0.001	m
Initial and final Kolmogorov time	τ_η	$3.75 \cdot 10^{-2}$, 0.27	s
Initial and final Kolmogorov scale in the cloud region	η	0.6, 2.2	mm
Root mean square of velocity fluctuation in cloud region	u_{rms}	0.1125	m/s
Initial particle response time $R_0 = 15\mu$ m	τ_p	$3.6 \cdot 10^{-3}$	s
Initial large eddy turn over time	$T_l = \boldsymbol{\tau}$	0.42	s
Initial droplet radius for monodisperse distribution	R_{in}	15	μm
Minimum droplet radius for polydisperse distribution	$R_{in-p,min}$	0.6	μm
Maximumm droplet radius for polydisperse distribution	$R_{in-p,max}$	30	μm
Total number of initial droplets (monodisperse population)	N_{tot-m}	$8 \cdot 10^6$	-
Total number of initial droplets (polydisperse population)	N_{tot-p}	10^7	-
Simulation time step	Δt	$3.8 \cdot 10^{-4}$	s
Initial energy ratio	$E_{cloud}/E_{clear\ air}$	6.7	-
Initial integral scale	l	0.048	m
Initial Taylor micro-scale Reynolds no.	Re_λ	42	-
Reynolds number based on domain dimension	Re_L	5000	-
Brunt-Väisälä amplification factor $N = (-g\Delta T T_0^{-1} L_{x_3}^{-1})^{0.5}$, unstable stratification	N^2	-0.068	s^{-2}

2.5 Different types of initial droplet distributions

Two types of possible size distributions of the population of water drops are considered in the current Direct Numerical Simulations (DNSs). For these two initial value numerical problems, we compared the extremes between possible population size distributions of water droplets: a monodisperse versus a polydisperse population with uniform mass per class of radii. Droplets are initially placed in the cloud only (where the turbulent energy is higher). The initial spatial distribution is random and uniform. See Figure 2.3.
The choice was made because:

a) In the literature, a typical form of size distribution in warm natural clouds to refer to is not yet available

b) On the other hand, it is recognized that the existence of a unique functional shape for the distribution size can be still questioned on many grounds as, for instance, a different and competing mechanism for droplets nucleation, growth, and removal present in a different context of cloud regions and cloud lives, see for

instance the paper Chandrakar et al. Droplet size distributions in turbulent clouds: experimental evaluation of theoretical distributions, QJRMS 146 (2020), 483-504 [87].

The monodisperse distribution, a drop size selected distribution, presents a small number of collisions given the fact that equal drops do not collide unless the local spatial variation of the turbulent air velocity are sufficient to give neighboring drops different velocities leading to a collision. The other way around, inside a polydisperse drop size distribution, the collision rate is high because different inertial drops show a different motion relative to the air, and this is even more so because of gravity.

Furthermore, since we wish to model a realistic cloud-clear-air boundary temporal evolution, we are out of the ideal conditions based on statistical steadiness in time and spatial homogeneity, that at the moment are the hypotheses that can only lead to a theoretical treatment. See, for instance, the recent approach based on the principle of maximum entropy (Liu and Hallett, On size distributions of cloud droplets growing by condensation: A new conceptual model, JAS, 55 (1998), 527-536 [58]; Wu and Mc Farquhar, Statistical Theory on the Functional Form of Cloud Particle Size Distributions, JAS 75 (2018), 2801–2814 [162]) or the approach based on Langevin equations representing the stochastic condensation-evaporation (Mc Graw and Liu, Brownian drift-diffusion model for the evolution of droplet size distributions in turbulent clouds, Geophysical Research Letters, 33 (2006) [114]; Chandrakar et al. Aerosol indirect effect from turbulence-induced broadening of cloud-droplet size distributions, Proc. Nat. Ac. Sci. 113.50 (2016), 14243–14248 [86]; Siewert et al. Statistical steady state in turbulent droplet condensation, JFM 810 (2017), 254 – 280 [32]; and Saito et al. Broadening of cloud droplet size distributions by condensation in turbulence, J. Met. Society of Japan, 19 (2019) 867–891) [72]. For a few time instants inside the transient, Figs. 7 and 8 in Golshan et al. IJMF 140 (2021), 103669 [105], corresponding to Figs. 3.2 and 3.3, respectively, show the numerical and mass concentrations for both drop populations. In both cases, it is evident a variation in the shape of the distribution inside the interaction layer. In the monodisperse case, Fig. 3.2, the distribution progressively enlarges. In the polydisperse case, Fig. 3.3, the distribution progressively shrinks. The size distribution shape variation is useful to get an overall view of the population evolution. The important clue we got from both the monodisperse and polydisperse population simulations is that the unsteady turbulence mixing confining the cloud region hosts a remarkable acceleration of the droplet population dynamics. In particular, the droplet evaporation and collisional activity are enhanced. In a time span where the turbulent kinetic energy of the airflow hosting the cloud is dropping by the 90%, the collision activity reduces by the 40% inside the cloud but rises by the 25% in the interaction mixing with the clear air. For the initially monodisperse population, in the mixing layer, the size distribution of the drop numerical density shows a growth of standard deviation 15 times faster than that in the cloud

region. The drop radius of the distribution peak slightly grows in time, more in the interface than in the cloud, while the value of the concentration peak decreases 4.5 more rapidly in the interface than in the cloud. In the polydisperse case, trends are reversed. The concentration distributions are now skewed in the opposite way, and the width of distributions shrinks in time, more quickly (about 4 times) inside the interface region than in the cloud. The drop radius of the distribution peak slightly grows in time, in the same way in both regions; while the value of the peak grows in the cloud and stays almost constant in the interface.

The observed acceleration of the population dynamics in the interface, and the rapid differentiation of the size of the droplets due to the different weights that evaporation, condensation, and collision have in the highly intermittent mixing region can, at least in part, explain the rapid increase in the size of droplets that is observed in some formations of cumulus clouds, in particular the maritime ones, and is considered capable of locally inducing rainfall (Mason and Chien, Cloud droplet growth by condensation in cumulus, Quar. J. of RMS 88.376 (1962) 136–142 [77]; Li et al. Condensational and collisional growth of cloud droplets in a turbulent environment, J. Atm. Sc. 77.1 (2020) 337–353) [164].

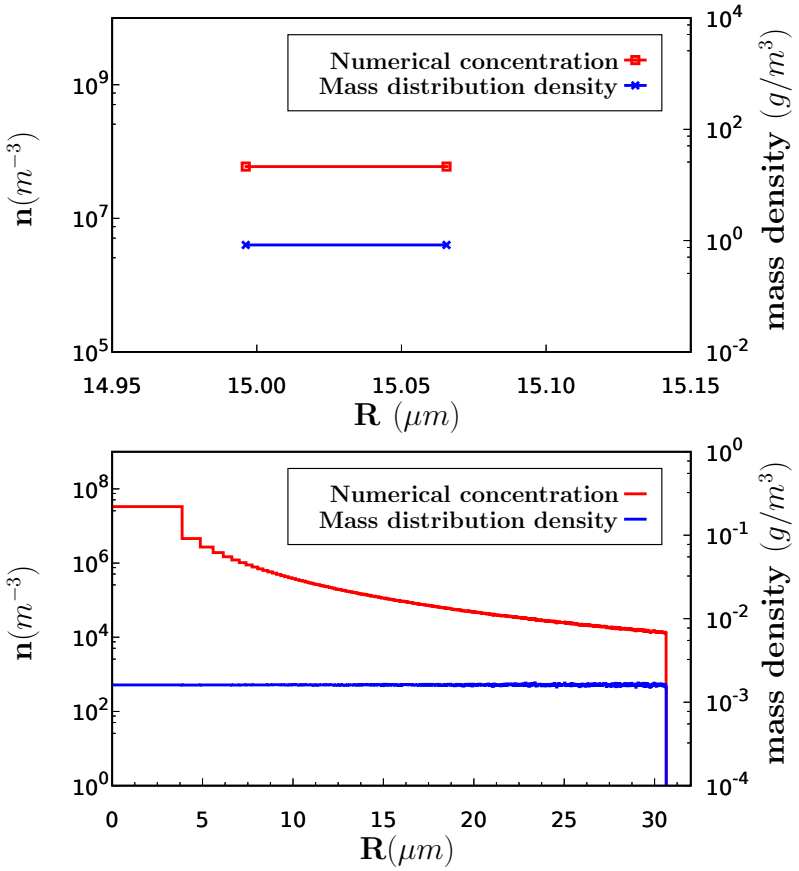

Figure 2.3: **Monodisperse (top panel, $8 \cdot 10^6$ particles) and Polydisperse (bottom panel, 10^7 particles) drop size distributions. The initial value of the total liquid content for both distributions is $LWC_0 = 0.8g/cm^3$**

It should here be mentioned that there is no source to force the system, as the aim is to model a realistic small cloud perturbation near the cloud boundary. It has in fact been demonstrated that the presence of a turbulence energy gradient is sufficient for Gaussian departure, due to the anisotropy effects, intermittency of the velocity fluctuation, and the velocity derivative statistics, for details, see Figures 2.4, 2.5.

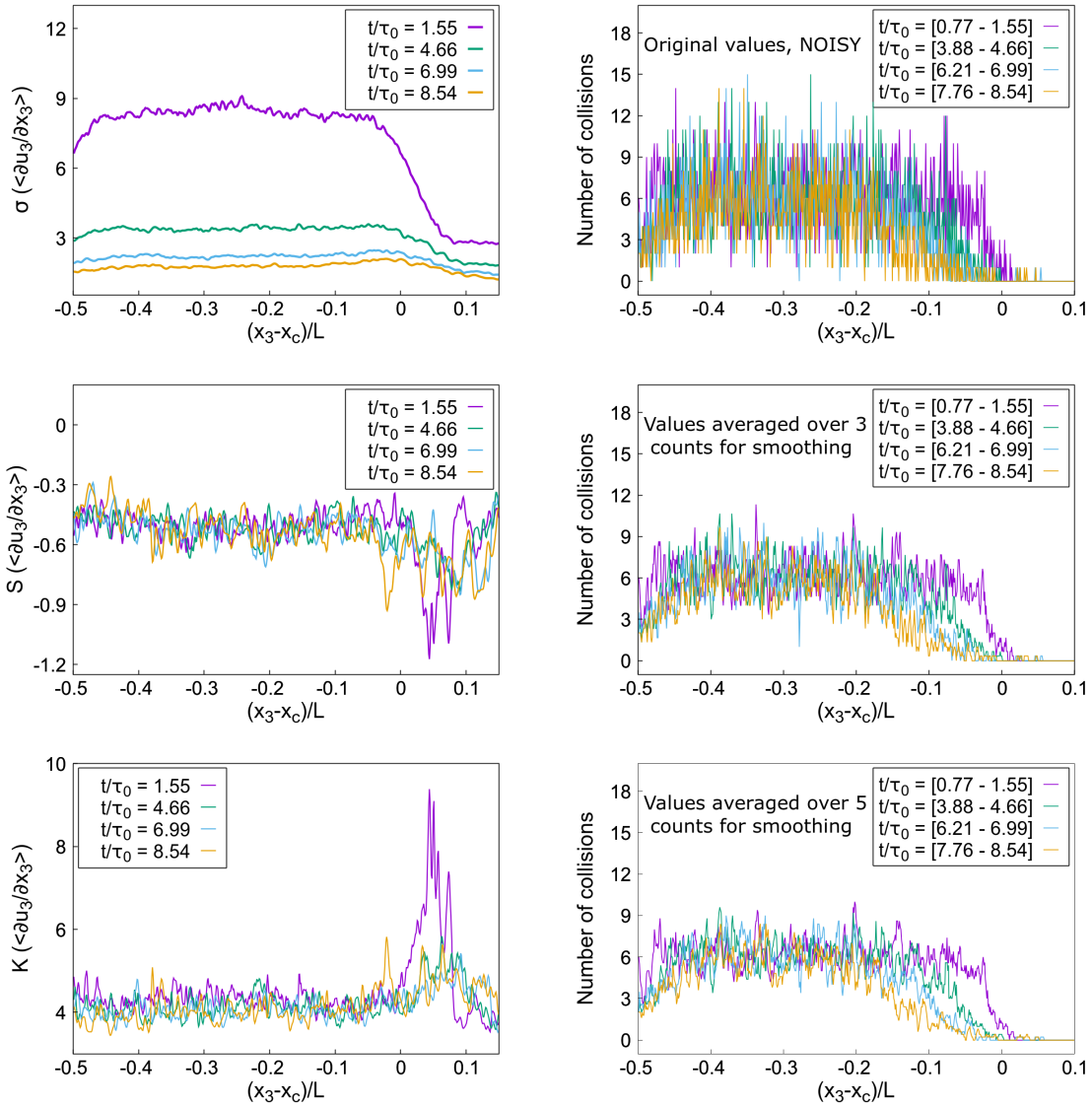

Figure 2.4: **Poly-disperse drop population, unstable and time decaying cloud clear-air interaction. Second, third and fourth statistical moments of the fluctuation of the longitudinal velocity derivatives of the background velocity field (left) and number of collisions along the vertical direction (right). The homogeneous portion of the domain (cloud region) and the interface region are shown in the panels on the left. Ensemble average obtained over three realizations. For the collision number, we show the averages over each computed section (noisy data, top right panel), and over three (middle right panel) and five adjacent sections (bottom right panel).**

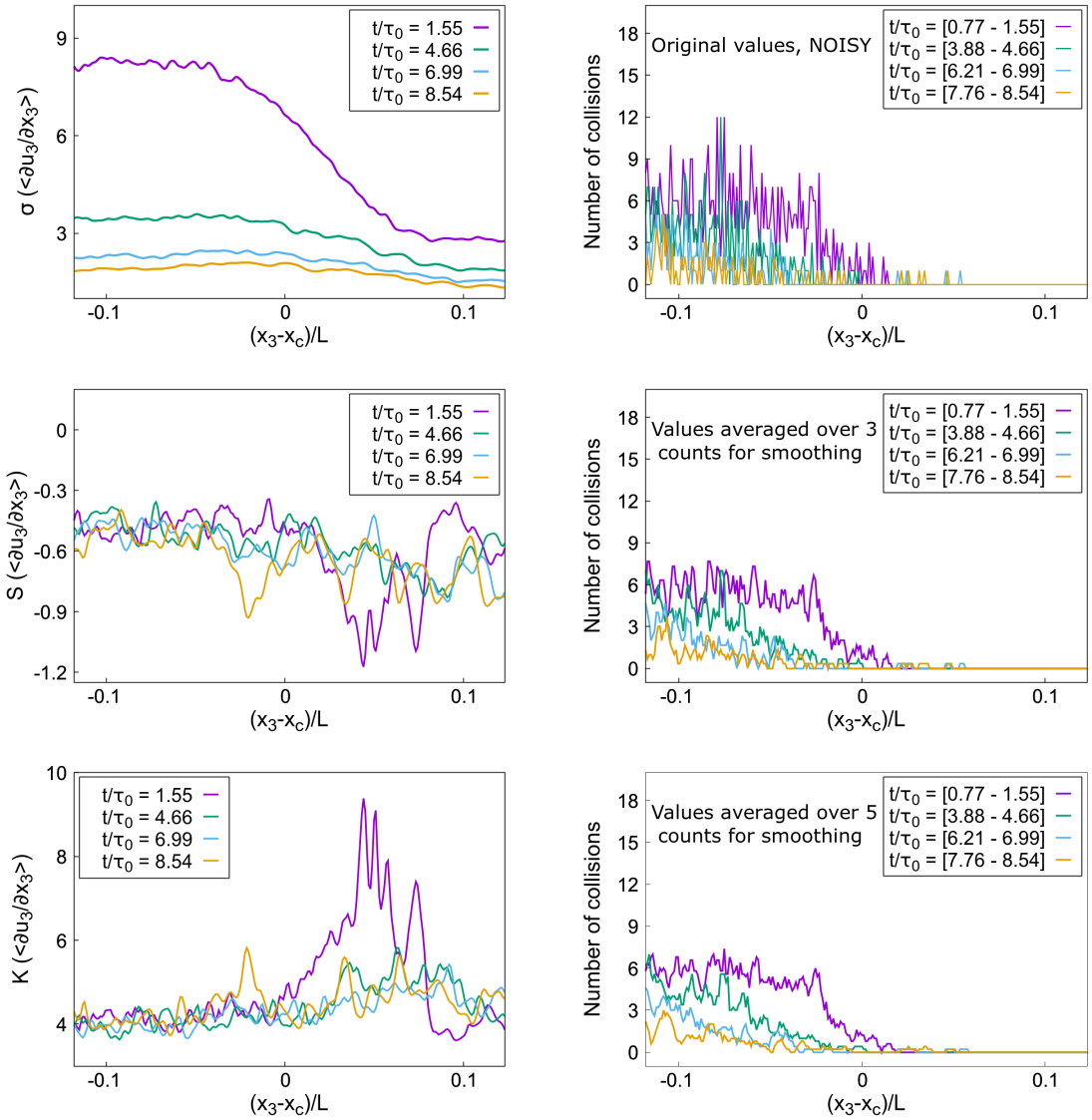

Figure 2.5: **Zoomed version of the previous figure. Second, third and fourth statistical moments of the longitudinal velocity derivatives of the background flow (left) and number of collisions (right) along the vertical direction and inside the turbulent interface region between cloud and clear air. Ensemble average obtained over three realizations. For the collision number, we show the averages over each computed section (noisy data, top right panel), and over three (middle panel) and five adjacent sections (bottom panel).**

In these figures, it can clearly be seen that the small scale of turbulence falls outside the isotropy and induces non-negligible pressure transport with respect to turbulent velocity transport, see [44] and [43]. All these aspects participate together with the transient evolution of the cloud /clear air system and influence the droplet collision rate in a way that has not yet been investigated in the literature, in particular since, in this situation, the penetration of the background airflow is maximal within the low turbulence range. However, it is interesting to observe what happens to the droplet collision rate, to the penetration of the boundary layer, and to the clear air portion of our system. In the following section, we will discuss in detail the results considering our direct numerical simulation for two types of cloud drop distributions.

Chapter 3

Intermittency acceleration of water droplet population dynamics inside the interfacial layer

3.1 Temporal evolution of the droplet size distribution and growth rate

In the following section, by applying the comparative method to the two types of drop populations, we will attempt to highlight the specific results that describe drop size growth for positive growth whenever condensation dominates and negative growth whenever the presence of evaporation dominates. The modification of the distributions and the temporal transient, which lasted for about ten eddy turnover times, was taken into account in these results.

According to the simulations that were performed in both calculation areas, that is, the volumes occupied by the cloud and the clear air interfaces, we discuss the calculation of the drop collision time rate, which is the numerical product density of the colliding drops. This information may be useful to understand, under our hypothesis of perfect collision-coalescence efficiency, the temporal evolution of the kernel of the aggregation integral term within the Population Balance Equation presented in the following section.

This term takes into account the formation of new particles resulting from the fusion of two drops and has not yet been determined under non-ergodic conditions. The current attempt to assess the temporal evolution of nuclear morphology is aimed at filling this gap. It should be considered a preliminary analysis that is necessary to understand that the set of simulations should be sufficiently meaningful to allow an effective interpolation to be made of the nuclear values. This should

provide an approximate model that represents a development of a non-ergodic system. Figure 3.1 shows a visualization of an inner slice of the computational domain perpendicular to the interface layer, in which water vapor, velocity entropy, and spatial droplet distribution can be observed. Three different transient stages of water vapor, velocity, and spatial droplet distribution were considered in these figures for snapshots at 3, 6, and 9 vortex turnover times.

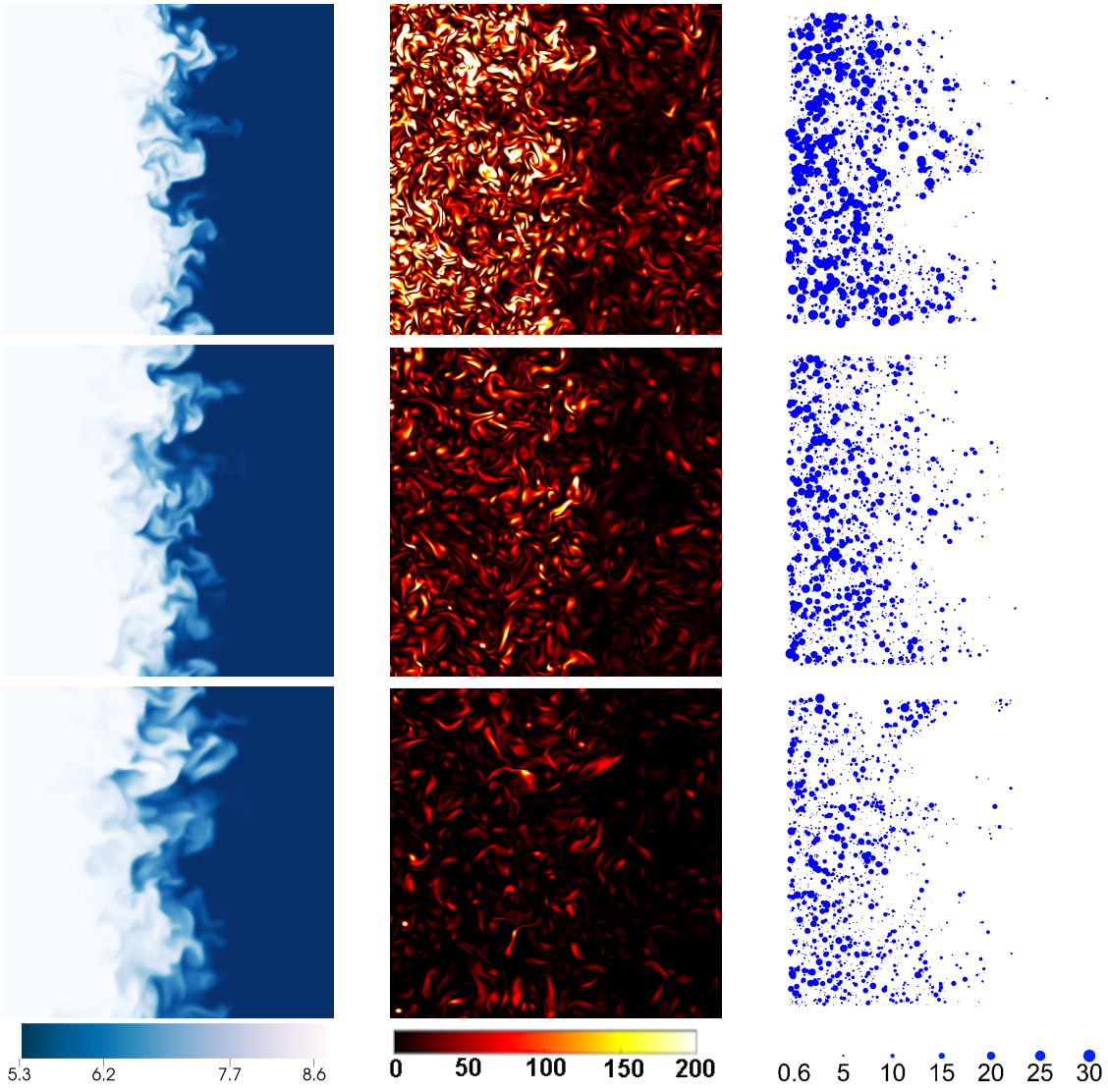

Figure 3.1: **Visualization of the fields inside the shearless interface between the cloud portion and the clear-air portion of the simulation: water vapor (left, legend values in kg/m^3), enstrophy (middle, values in sec^{-2}) and droplets (right, diameters in arbitrary units) for snapshots at 3, 6 and 9 eddy turnover times.**

3.1.1 Evolution of the droplet size distribution, condensation and evaporation collision-coalescence

The numerical and mass concentrations are demonstrated in Figures 3.2 and 3.3 for both drop populations (monodisperse and polydisperse) inside the transient, after the evaluation of a few time instants. In both cases, a variation of the shape of the distribution inside the interaction layer is evident. Figure 3.2 indicates the reaction of the size distributions for the monodisperse case. The result that this figure highlights is the intensification of the droplet size distribution for the specific radii of the cloud droplet, which are smaller than the initial radius, which is 15 µm. After some time, approximately 8.54 τ, the numerical concentration of the drops in both portions (cloud and clear air and interaction zones) is clearly visible.

The numerical concentration of the droplets inside the mixing layer, which is the interaction zone, in the 13 µm range is 100 times higher than in the cloud, and the minimum radius is slightly lower than 11 µm. We hypothesize that the distribution width from Fig 3.2 is also much broader in the mixing layer. The increase in the width of the distribution inside this zone is due to the collisions that involve coalesced droplet radii. Droplets with a different radius from the initial one (15 µm) can be observed. For instance, the collision can be seen between drops with 13 µm and those of 11 µm. When the results inside the cloud portion are considered, a different outcome is obtained. The minimum radius inside the cloud is slightly below 13 µm, and a collision takes place mostly between droplets that are close to 15 µm. This can highlight that the evaporation is much more intense inside the anisotropic portion of the system. By looking at panels c) and d) in Figure 3.4, it can quickly be appreciated that there is a figure which describes the condensation and evaporation processes that take place concomitantly in both parts of the system.

When observing the polydisperse distribution case, we perceived that there are more concentrated dynamics inside the interaction region than in the cloud region. It is worth mentioning that these type of distributions initially includes drops which are randomly situated inside the cloud region with a mass uniform in the volume classes ranging from 0.6 to 30 µm; for more details, see Figure 3.3.

An obvious distinction in time can be observed for the numerical concentration inside the interface. For example, for the droplets, which are large in radii close to 30 µm, the decrease is of three orders of magnitude; for better observation, see panel b) in Figure 3.3. An enlargement of the distribution, up to radii of around 38 µm, can be appreciated in both panels a) and b) in this figure. It is clear that the maximum radius reachable from the coalescence of two droplets is around 38 µm. However, in the cloud region, the growth as a result of coalescence is accompanied by a robust condensation, which presents radii of more than 30 µm in the interface region, see panels a) and b) in Figure 3.3.

The different weights that condensation and evaporation have on the temporal evolution of the system can be observed by considering Figures 3.4 and 3.5. These figures contain data, from the top to the bottom, on the positive radius growth (condensation), on the negative growth (evaporation), and on their resulting effects at a given instant close to the end of the transient (8.0 eddy turn overtimes).

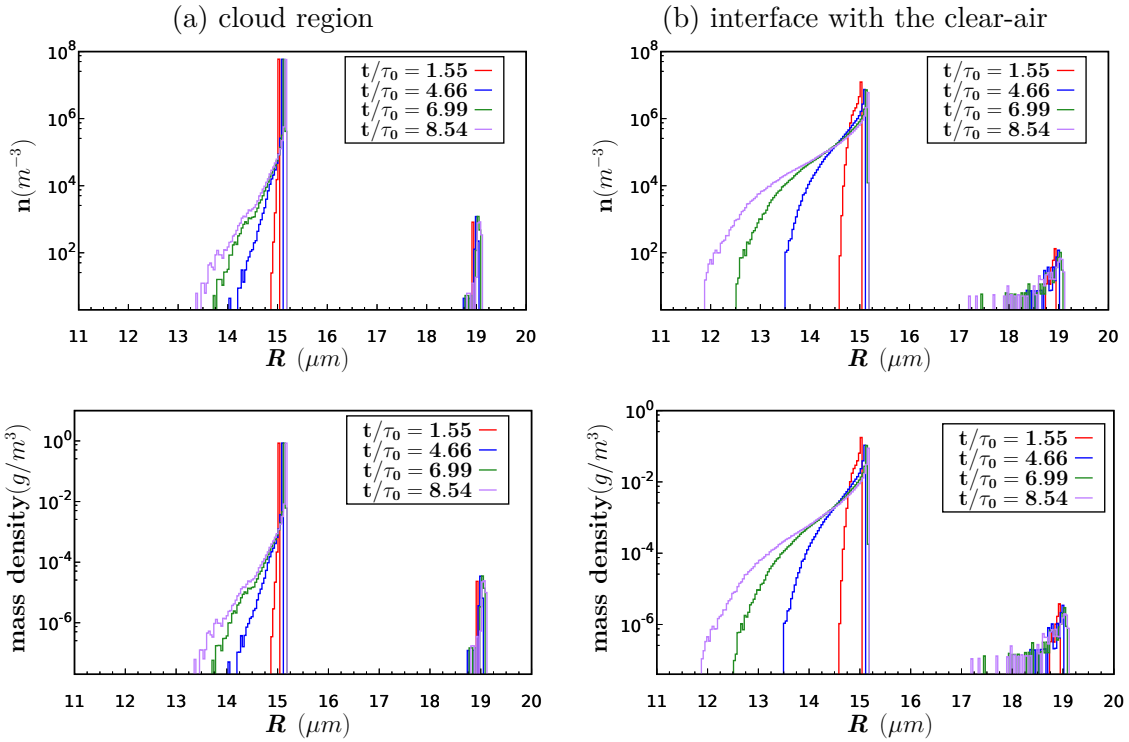

Figure 3.2: **Water droplet size and mass distribution. Simulation of the monodisperse drop population centered around an initial value of 15 µm, $8 \cdot 10^6$ droplets. Panel (a) droplet size distribution and mass distribution as a function of the radius classes for the cloud region (HIT turbulence). Panel (b): droplet size distribution and mass distribution as a function of the radius classes for the cloud and clear air/interface (shearless turbulent layer). See Table 1 for the physical and thermodynamical parameters and Table 2 for details on the numerical simulation parameters.**

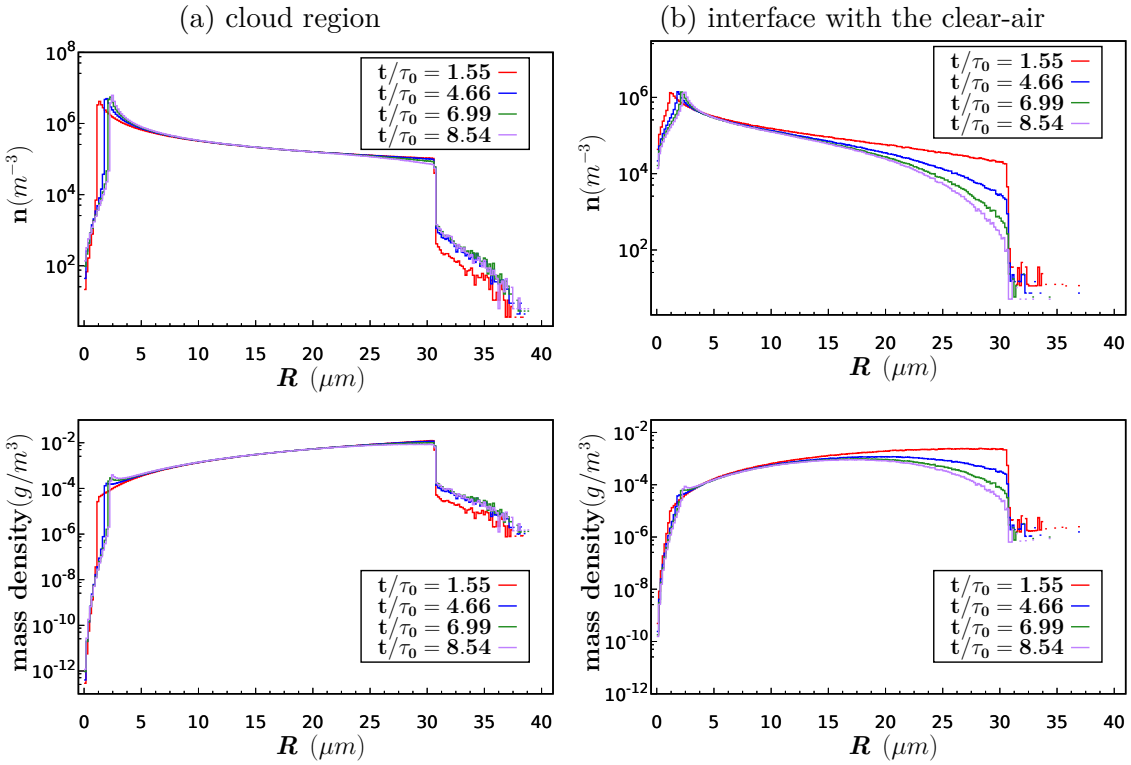

Figure 3.3: **Water droplet size and mass distribution. Simulation of the polydisperse population with radii initially inside the $0.6 - 30$ µm range, 10^7 droplets. Panel (a) droplet size distribution and mass distribution as a function of radius classes for the cloud region (HIT turbulence). Panel (b) Droplet size distribution and mass distribution as a function of the radius classes for the cloud and clear air/interface (shear-less turbulent layer). See Table 2.1 for the physical and thermodynamical parameters, and Table 2.2 for details on the numerical simulation parameters.**

If we start from the monodisperse population dynamics, it is easier to understand the consequence on the dynamics of the polydisperse population. By concentrating on the left side of Figure 3.4, it can be observed that the condensation process is present inside the cloud portion. This process is slower than the evaporation process, that is, about ten times. Counter-intuitively, condensation is proportionally more intense on collided-coalesced drops, see the right-hand side of panel a). A small range of radii ($13.5 - 13.7$ µm) can also be observed where the condensation-evaporation processes are perfectly balanced (see panel c). We can also observe an intense condensation for droplets close to 15 µm and for the collided-coalesced droplets droplets in the interaction region, panels b), d) and f), which gather around radii close 18.9 µm.

Evaporation becomes very important over time and generates drops as small as 11.8 µm after 8.54 τ_0, even though the turbulent kinetic energy inside the system falls by as much as 18 times in the cloud region and by six times in the clear-air region. It should be noted that evaporation is immediately active inside the collided particle within the shear-less interface layer, which does not happen inside the cloud region. Overall, evaporation and collision prevail over condensation inside the interface region.

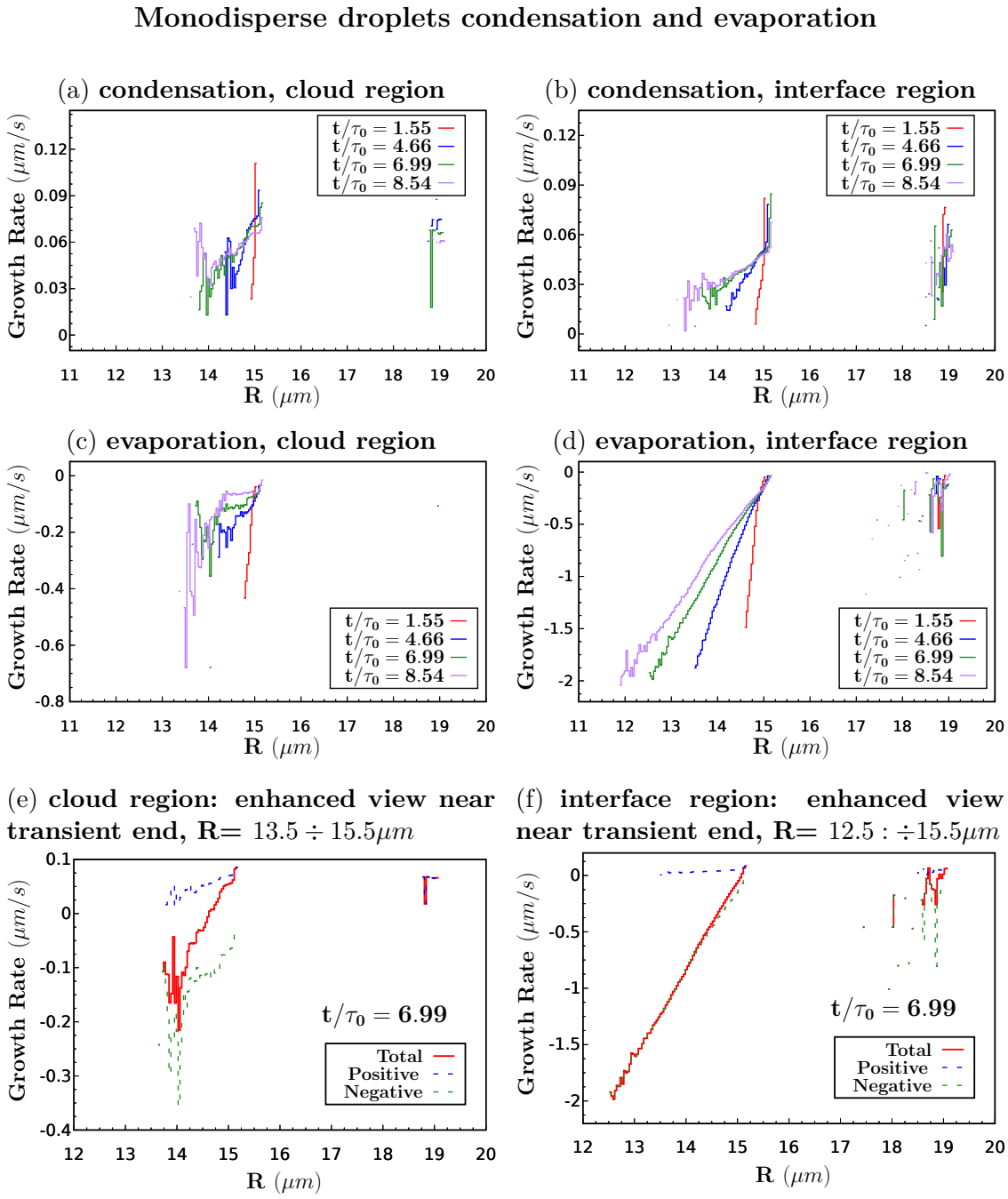

Figure 3.4: **Monodisperse drop size distribution, unstable and time decaying cloud clear-air interaction. Mean droplet radius growth rate for different radius classes. From top to bottom: positive, negative and mean growth rate are shown for selected time instances for Polydisperse droplet condensation and evaporation.**

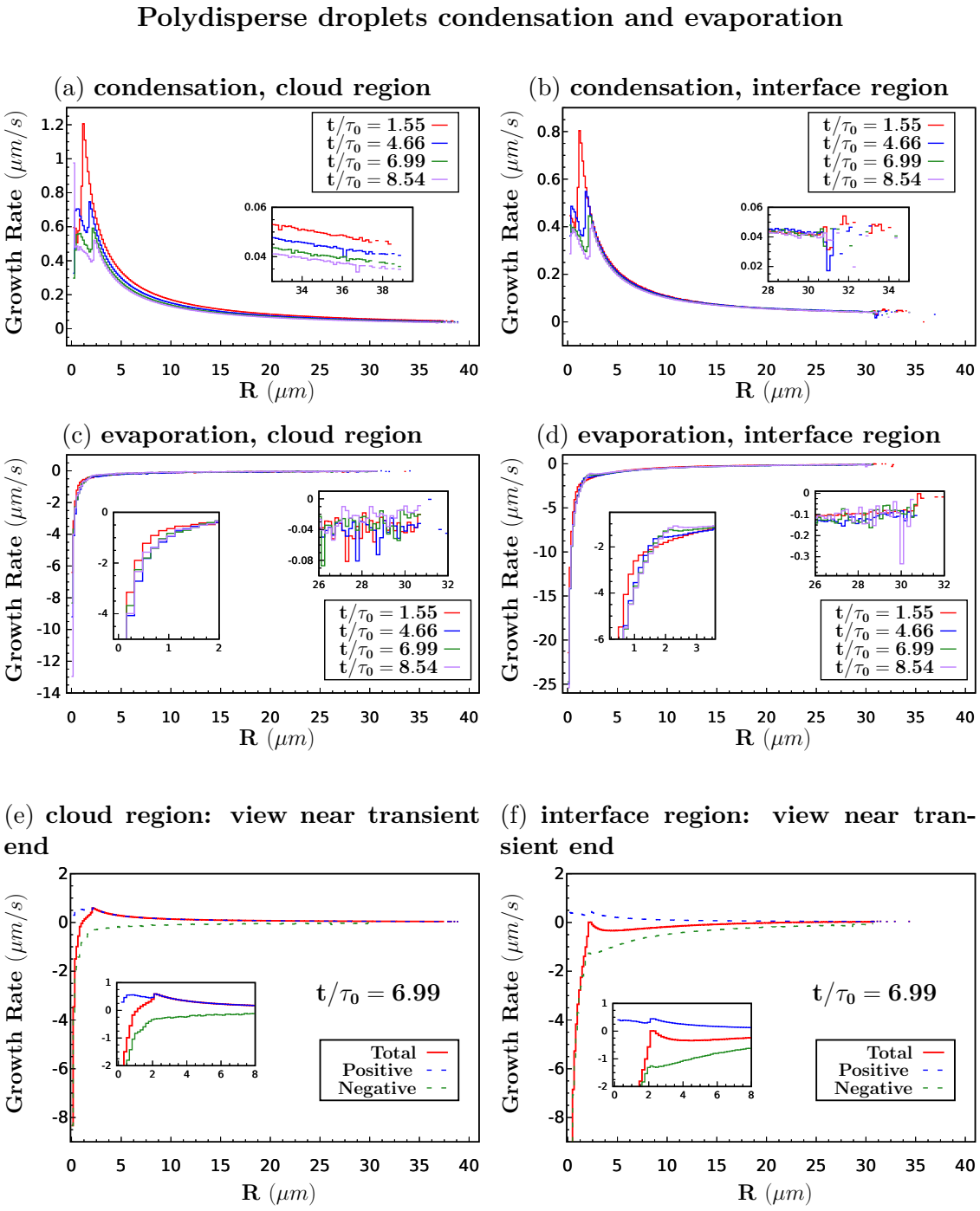

Figure 3.5: **Polydisperse drop size distribution, unstable and time-decaying cloud clear-air interaction. Mean growth rate for different radius classes. From top to bottom: positive, negative, and mean growth rates for selected time instances. The total, positive, and negative means are shown for selected time instances.**

The situation is different for the case of the polydisperse distribution, see Figure 3.5. Transient condensation clearly prevails over evaporation throughout the cloud region. Inside the interface layer, once again, evaporation prevails over condensation, but more weakly. As usual, more intense evaporation is present for smaller drops, as the curvature effect (the negative Kelvin term in the radius growth rate equation (2.16)) plays an important role. An evaporation rate that is about three times more intense than the condensation rate can be observed here. The condensation and evaporation rates both evolve non-linearly over time at the interface, and the maximum values can be observed for around five eddy turn overtimes.

Table 3. Droplet size distribution trends during the transient decay inside the cloud and the interfacial layer

CLOUD **Quantity**	**Fit Law**	**Unit**
Initial Monodispersion		
Standard deviation	$\sigma_{CM}(t) = 0.015\, t/\tau_0 + 0.05$	μm
Width w at the 0.03% of the probability density peak	$w_{CM}(t) = 0.047\, t/\tau_0 - 0.006$	μm
Polydispersion (initial uniform mass)		
Standard deviation	$\sigma_{CP}(t) = -0.19\, t/\tau_0 + 19.69$	μm
Width at the 3% of the probability density peak	$w_{CP}(t) = 26.47 - 2\,\exp(0.11 t/\tau_0)$	μm
INTERFACIAL MIXING **Quantity**	**Fit Law**	**Unit**
Initial Monodispersion		
Standard deviation	$\sigma_{IM}(t) = 0.23\, t/\tau_0 + 0.003$	μm
Width w at the 0.03% of the probability density peak	$w_{IM}(t) = 0.28\, t/\tau_0 - 0.02$	μm
Polydispersion (initial uniform mass)		
Standard deviation	$\sigma_{IP}(t) = -0.74\, t/\tau_0 + 17.94$	μm
Width at the 3% of the probability density peak	$w_{IP}(t) = 16.62 - 17.23\,\exp(0.67 t/\tau_0)$	μm

Suffices: CM cloud mono, CP cloud poly, IM interface mono, IP interface poly

3.1.2 Comments on the droplet size distribution structure

The turbulent energy inside the transient regions decays quickly in both the cloud and the interface regions, which are characterized by intense anisotropy. A system that is far from ergodicity could be expected in this area. It should be pointed out that the premium data and information revealed by the size of the drop distributions are not sufficient to emphasize the quantitative details of the condensation-evaporation procedures, which are instead visible in the analysis shown in the previous figures, that is, Figures 3.4 and 3.5. However, a variation of the size distribution structure is useful to obtain an overall picture of the population evolution.

Figures 3.6 and 3.7 represent the quantitative data of the distribution shape, width and position of each cloud droplet inside the domain. In the monodisperse case, see Figure 3.6, the distribution is highly skewed both inside the cloud region and the interface layer, see panels a) and b), where the distribution near the end of the transient is shown. The two distributions are different and in particular, their widths are different. The width of the interface region is greater and is almost five times larger than that of the cloud region. By considering panels c) and d), it can be seen that, in order to enrich the specific information on the shape of the size distribution of the drops, it is necessary to measure the time scale of the standard deviation of the drop size and the width of the distribution at a given percentage of the distribution peak value (0.03 %, where values are clearly readable).

The width of the distribution and the standard deviation of the drop size evolve over time. A difference in these quantities can be observed according to where they are located. For instance, the standard deviation growth is 13 times larger at the interface, while the width is six times larger at 0.03% of the peak value. The highlighted point refers to the slightly growing radius of the distribution peak over time, which occurs more in the cloud region than at the interface. On the other hand, the value of the concentration peak decreases more rapidly at the interface, see panels e) and f).

For the polydisperse case, see Figure 3.7, where it can be observed that the trends are reversed. The concentration distributions are skewed oppositely, i.e., the concentration distributions increase over time toward the large radius side, see panels a) and b), where the distribution shape is shown near the end of the transient, that is, again at about 7.8 eddies turn overtimes. The width of the distributions shrinks more quickly over time (about three times) inside the interface region, see panels c) and d), where information is included on the width of the distribution at a concentration equal to 3% of the peak value. The radius of the distribution peak and its value grows over time in more or less the same way both inside the cloud and inside the interface region.

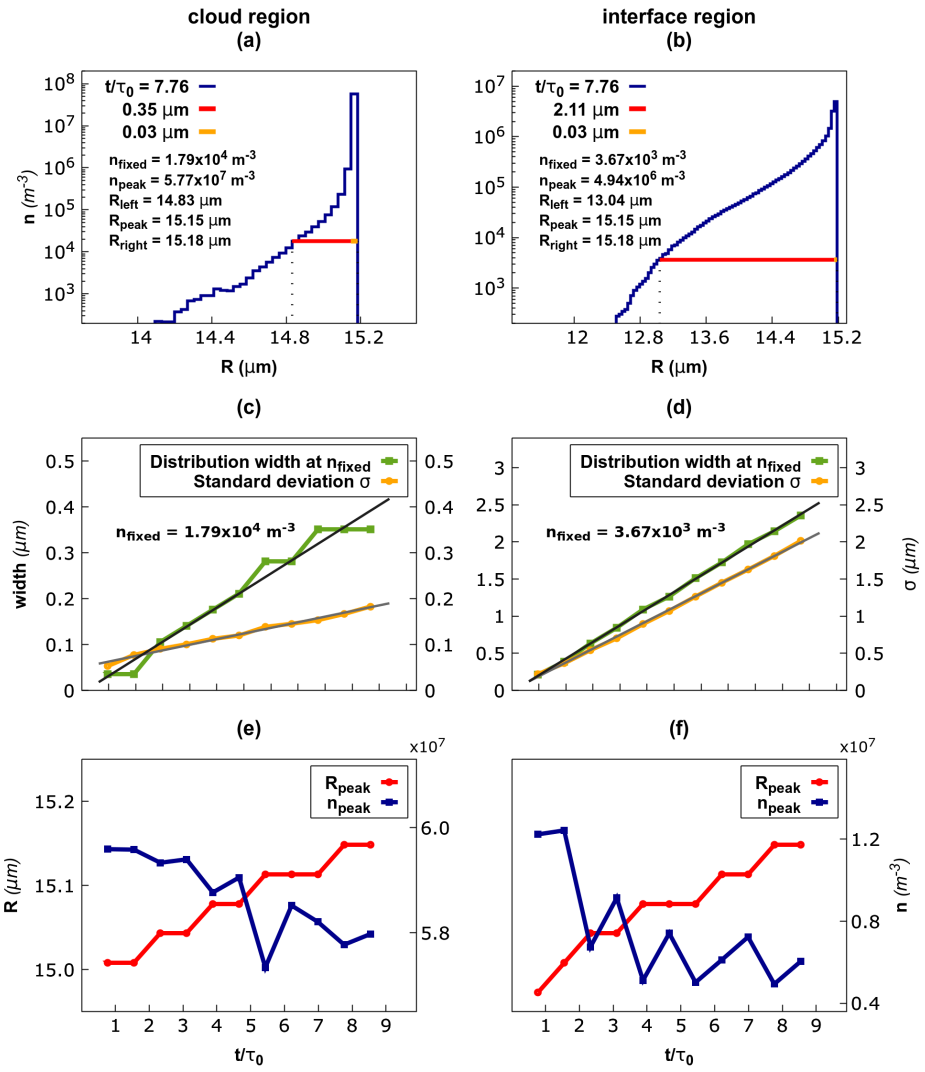

Figure 3.6: **Drop size distribution for the Mono-disperse case, unstable and time-decaying cloud clear-air interaction. Distribution characteristics. From top to bottom: left and right parts of the distribution with respect to the peak value for selected time instances (a,b); change in the distribution width over time (green) and its fit (black, $0.047\ (t/\tau_0) - 0.006$ in the cloud and $0.28\ (t/\tau_0) - 0.02$ in mixing), standard deviation of the distribution over time (orange) and its fit (gray, $0.015\ (t/\tau_0) + 0.05$ in the cloud and $0.23\ (t/\tau_0) + 0.003$ in mixing) (c,d); change in the peak distribution value (blue) and corresponding radius class (red) over time (e,f).**

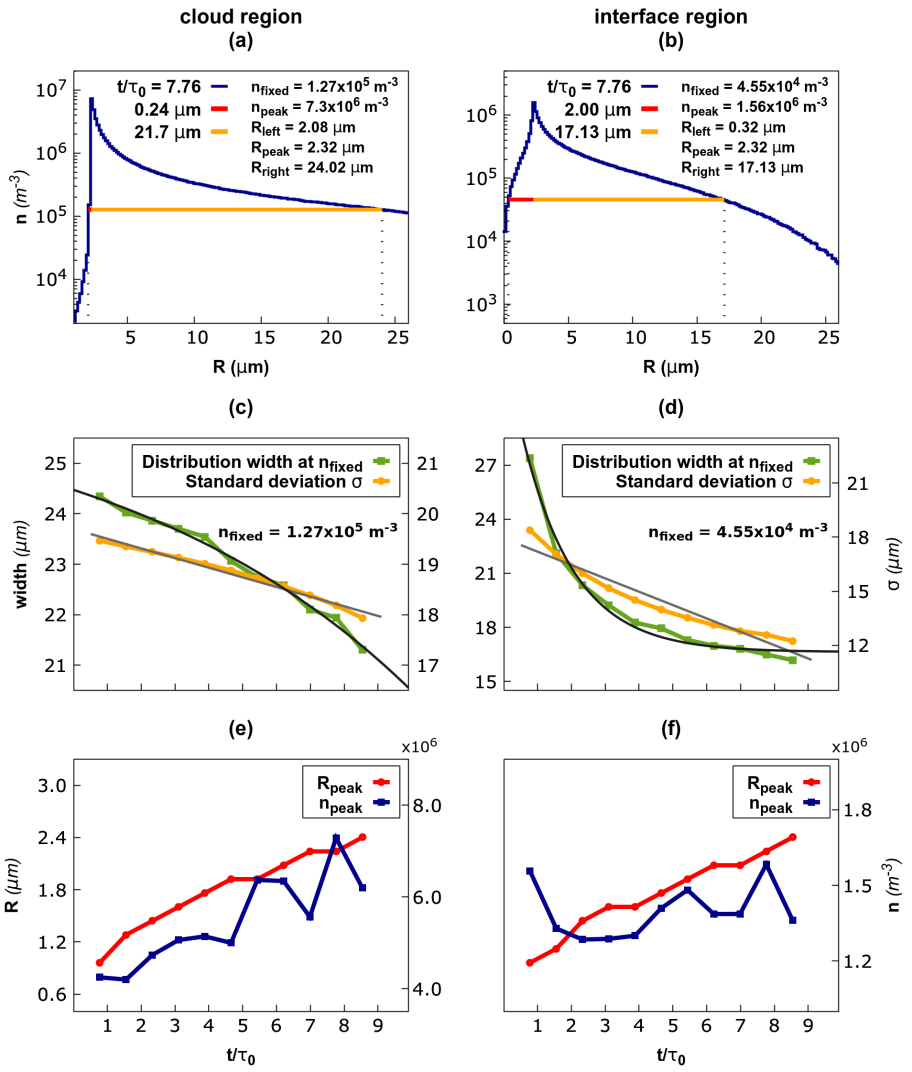

Figure 3.7: **Poly-disperse drop size distribution, unstable and time-decaying cloud clear-air interaction. Distribution characteristics. From top to bottom: left and right part of the distribution with respect to the peak value for selected time instance (a,b); change in the distribution width over time (green) and its fit (black, $26.47 - 2\exp(0.11\,(t/\tau_0))$ in the cloud and $16.62 - 17.23\,\exp(-0.67\,(t/\tau_0))$ in mixing), standard deviation of the distribution over time (orange) and its fit (gray, $-0.19\,(t/\tau_0) + 19.69$ in the cloud and $-0.74\,(t/\tau_0) + 17.94$ in mixing) (c,d); change of the peak distribution value (blue) and the corresponding radius class (red) over time (e,f).**

3.1.3 Collision Kernel under anisotropic temporal decaying flow

There are basically three major effects of turbulence on enhancing the chance of droplet collision: the first one refers to the turbulent transport effect, which augments the droplet radial relative velocity (RRV) through the local shear and air acceleration [145] (increase in the swept volume). The second effect, termed the clustering effect, redistributes the cloud droplets in such a way that they cluster in low vorticity and high shear regions because of their inertia ([131], [136], [31], [11]) proposed that clustering can also occur in low Lagrangian acceleration regions. The third effect pertains to droplet-droplet aerodynamic interactions, which affect the collision efficiency [145], whose effect has not been considered in this study. The collision kernels generally depend on three criteria: the size of the colliding droplets, the type of the initial drop size distribution (monodisperse or polydisperse), and the process conditions.
Collision kernels are used in equations that govern the evolution of the droplet size distribution, which are referred to as population balance equations (PBE), See, for instance, [110], [113].

The main purpose of the present work has been to extract direct numerical simulations, which refer to what takes place inside a turbulent airflow, in order to evaluate the possibility of computing the collision kernels. As seen above, this evaluation has been carried out for two initial size distributions with a uniform mass. The purpose of this comparison was to help clarify the topic, which has not yet been done, and no results are, in fact, available in the literature. Investigating the typical form of the size distribution in warm natural clouds remains an open question.

In such a fully non-ergodic condition, the aim of this work has been to offer a first preliminary data set on the statistical convergence that can be reached using the popular approach whereby the drop size spectrum is approximated by a set of size classes. Most attention has been concentrated in the literature on turbulent flows laden with solid particles or liquid droplets, which are based on steady-state homogeneous isotropic turbulence. Let us here summarize the situation. The pioneering theory proposed by Marshall in 1954 [130] may be considered one of the most significant works for atmospheric sciences. The most crucial result of his work is that equal drops rarely collide. A few years later, Saffman [59] considered collision between small drops of similar size in a homogeneous, isotropic, statistically stationary turbulent flow. He considered both drops moving with the air (zero inertia particles) and relative to the air in the presence of gravity. The distribution of drops was random and uniform. Since homogeneous and isotropic turbulence was considered, the resulting collision rate could be presented in two fundamental terms: the dissipation rate of turbulent kinetic energy and viscosity (as well as the radius of each drop). Recent research has shown that the drop concentration in

turbulent flows may be highly non-uniform, with anomalously high or low local concentration regions. The coherent vortical structures in real turbulent flows are the mechanisms that lead to preferential concentrations by producing directed (non-random) motions of the particles. This kind of dynamics is frequently observed in gas flows laden with solid particles or liquid drops, and it is related to the significant difference in density between the carrier flow and the filling particles. The variations in particle concentration are much more significant than could be expected from statistical considerations. This raises serious concerns about the usefulness of statistical models to represent particle-laden turbulent flows, [88]. The preferential concentration of drops usually describes the accumulation of dense particles within specific regions of an instantaneous turbulence field, which means that liquid drops do not tend to follow whirling curved streamlines. These particles will tend to accumulate in regions of high strain rate or low vorticity. When this hypothesis is considered, a low drop in concentration can be expected in the regions where the vortex cores are dominant. Numerous experiments and simulations have confirmed this result, see for example, [131], [136], [31], [11], [80].

Another effect is related to droplet-droplet aerodynamic interactions, which affect the collision efficiency [145]. Because of the complexity of the problem [116], there are only a few Direct Numerical Simulations (DNSs) studies concerning this latter effect ([115], [117]), and most of these researches are still underway. This effect was not considered in the Lagrangian model of droplet transport and collision used here.

Let us now return to the investigation of the collision kernel, which we have carried out using direct numerical simulations. The analysis was performed on a disturbed shear-less turbulent layer, where a slightly unstable stratification is active on either the monodisperse or the polydisperse droplet population. In this second case, given the simultaneous presence of somewhat different droplets, the volume ratio between the largest and the smallest droplet is in the order of $1.25 \cdot 10^5$, and the number of collisions will be large. We observed about $5 \cdot 10^4$ collisions over about ten physical time scales for 10^7 total droplets.

The turbulent process for which we measured the collision kernel tries to imitate a particularly small initial disturbance of the boundary cloud and clear-air.

The process includes the effects of non-stationarity, anisotropy, and inhomogeneity of the fluctuations, including inertial effects, condensation-evaporation-growth decay of the droplets, as well as gravitational stratification and settlement. It should be recalled that such collisions have to be considered from a geometrical point of view since Stokes' resistance has been included in the momentum equation of the particle, but any local aerodynamic interactions between droplet and droplet have not been considered. Therefore, we have assumed a collision efficiency equal to one.

Another small simplification is that the coalescence efficiency, which is defined as the ratio of the number of droplets that actually merged with the total number

of collisions, is assumed to be one. However, laboratory studies on colliding cloud droplets have shown that the coalescence efficiency is close to one, see ([45], and [154]).

In our study, the initial liquid water content (LWC) is 0.8 g m^{-3}, a value that is close to the typical adiabatic value found in cumulus clouds.

The collision kernel from our simulations has been computed as:

$$\Gamma(\mathrm{R_1}, \mathrm{R_2}; \mathrm{t}, \mathcal{V}) = \frac{\mathrm{N_{coll}}}{\mathrm{n_1 n_2}} \frac{\mathcal{V}}{(\mathrm{t_2} - \mathrm{t_1})}, \tag{3.1}$$

where $N_{\mathrm{coll}}(\mathrm{R_1}, \mathrm{R_2}, \mathrm{t} \in [\mathrm{t_1}, \mathrm{t_2}])$ is the counter of collisions between droplets of radius r_1 and r_2, which occur during a selected time window $[t_1, t_2]$ and within a selected spatial region of volume $\mathcal{V} = L_1 \times L_2 \times \Delta x_3$. In the denominator, n_1 and n_2 are the counters of **all droplets** within the class size where $\mathrm{R_1}$ and $\mathrm{R_2}$ are met, for the same temporal range and spatial volume. See, for example, equation (2.3) in [113].

All counters are obtained from a uniform radius discretization. This computation is approximated because n_1 and n_2 approximate the counters of particles of radius $\mathrm{R_1}$ and $\mathrm{R_2}$ in the limit for $\delta\mathrm{R} \to 0$. We performed a set of computations in which we subdivided the radius range, the range $[0.6 - 30]$ µm in the case of the polydisperse population, into 16 classes and up to 512 classes. Which means from a $\delta\mathrm{R} = 2.5$ µm to a $\delta\mathrm{R} = 0.078$ µm.

We analyzed the evolution of kernel time over intervals of a width that was comparable with the turbulence vortex rotations overtime calculated at the beginning of the simulation, τ_0. The observation starts from the starting time and continues until about $10\tau_0$. Since we have about 50000 collisions over the entire time evolution for the initial distribution of the polydisperse drop size, we obtained about 5000 collisions per interval. In the course of the development, we analyzed the variation of the number of collisions within the cloud part and on the boundary surface. This will allow us to estimate, in a future simulation campaign, the number of realizations required to obtain a useful estimate of the ensemble mean of the kernel value. Let us now start with a description of the results by looking at Figure 3.8, which shows the collision kernel values for the polydisperse population calculated within time intervals as large as one-third of the transient decay. The interface values are shown in the column on the left, while the cloud values are shown in the column on the right, where the drop radii are divided into 256 ranges. The first third of the transient decay, which is shown in the upper plates, has about 10400 collisions per 10 million drops. Almost a quarter of the collisions take place at the interface. It can be seen that the kernel values are higher at the interface almost everywhere throughout the pixelized matrix than in the cloud part. The importance of the kernel values is not sharply contoured. Large parts of the matrix can be observed where there is an intense and discrete (pixelated) merging of the values, which differ by one or more orders of magnitude. This is also true for the other two-thirds of

the transient, where the main difference is the increase in the number of collisions at the interface at the expense of the number of collisions within the cloud. At the end of the lower plates of the transient, the number of collisions on the boundary surface is higher than within the cloud (4179 compared to 3824). In Figure 3.8, we can see dots (pixels) outside the initial drop ranges $[0-30]\mu m$ x $[0-30]\mu m$, which represent drops resulting from a possible double or triple sequence of collisions, see also Figures 3.3 and 3.5.

The values here are at the maximum ($1 \cdot 10^6$) and have been determined exactly since the concentration of the drops with radii corresponding to those of the colliding drops is automatically calculated exactly. This is because drops with other radii, but in the same class, are rarely present here. It should be noted that the number density of collisions (the number of collisions divided by the volume) within the cloud region remains almost constant over time, simultaneously with the decay of the turbulent kinetic energy.

The situation within the interface region, which is expanding in both the simulation and the real system, is also interesting. The absolute number of collisions within the boundary layer increases, while the volume density of the collisions decreases slightly, by almost 30%.

This aspect is considered later on when commenting on the relationship between the collision with velocity and the interruption of the passive scalar fluctuation.

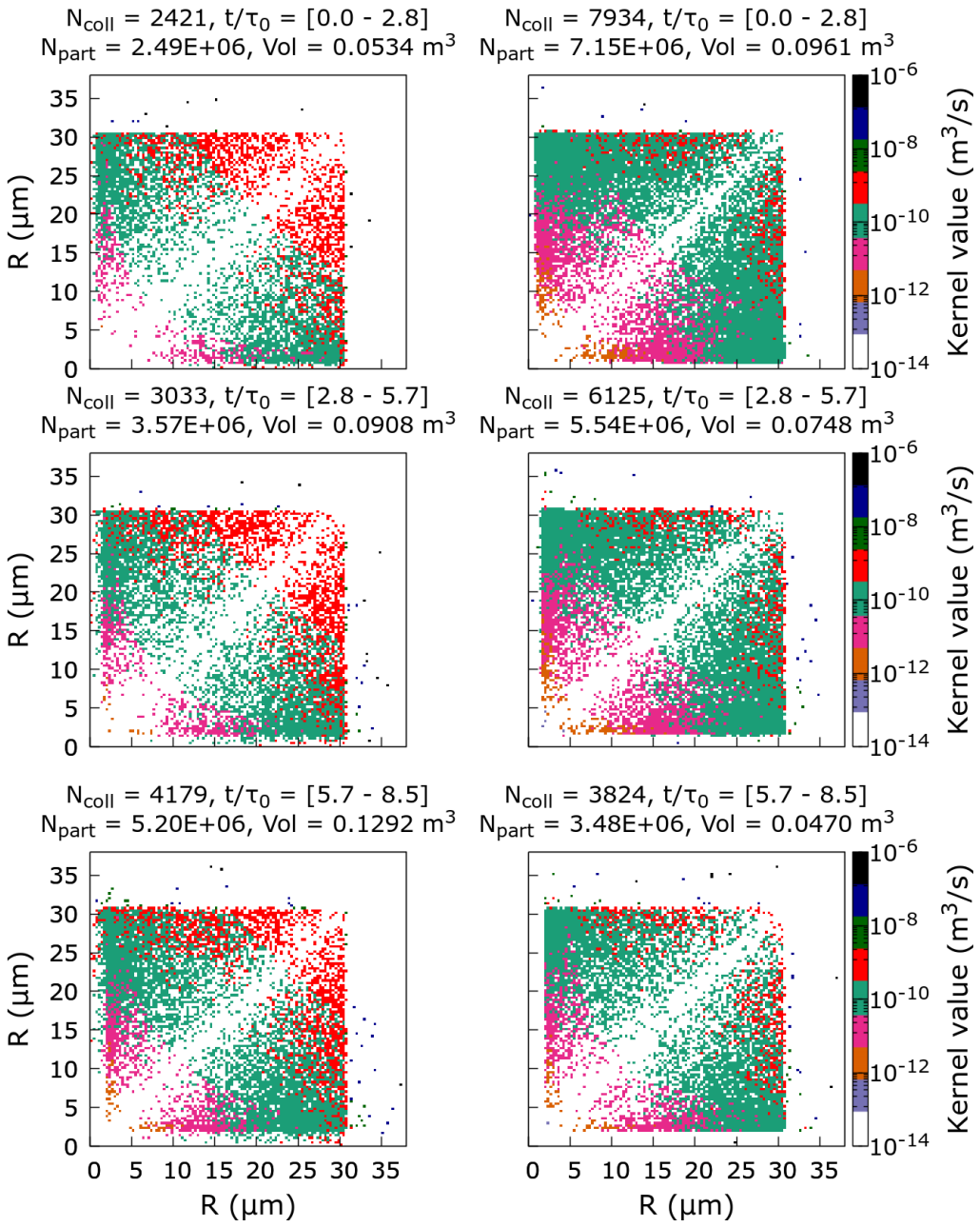

Figure 3.8: **Polydisperse drop size distribution, unstable and time decaying cloud clear-air interaction. Comparison of the kernel value evolution at the cloud-clear air interface (left) and the homogeneous cloud region (right). Ensemble average obtained from three realizations of simulation data, mean evolution over time intervals for as long as one third of the entire observed decay. Collision radii subdivided into 256 classes.**

Let us now look at the situation for the initially monodisperse droplet population. A dramatically lower number of collisions can be observed - which is quite noticeable, considering that the droplets are initially identical, see Figure 3.9, where the total number of collisions along the entire transient is about 400 of the 7 million drops introduced into the system to reach the total liquid water content for the warm cloud ($LWC = 0.8$ g/m^3). The number of collisions and the transient decay by 76 % within the cloud region. This happens simultaneously with the 92% decay of the turbulent kinetic energy. Instead, the absolute number remains constant within the expanding interface region, where the droplets evaporate rapidly. This corresponds to a 50 % decay of the number density with a simultaneous decay of the turbulent kinetic energy of 86 %.

It is evident that the collision activity is low, with respect to condensation-evaporation dynamics, within the initially monodisperse population dynamics. The information that can be derived from this analysis refers to the diagonal and lateral propagation in the radius range where information is available. From this set of simulations and by averaging the actual ensemble, a diagonal propagation of about 18% per vortex rotation over time and lateral propagation of 25% can be derived as preliminary information. About 100-200 realizations are required for a simulation campaign that would lead to an ensemble averaging based on about several thousand collision events.

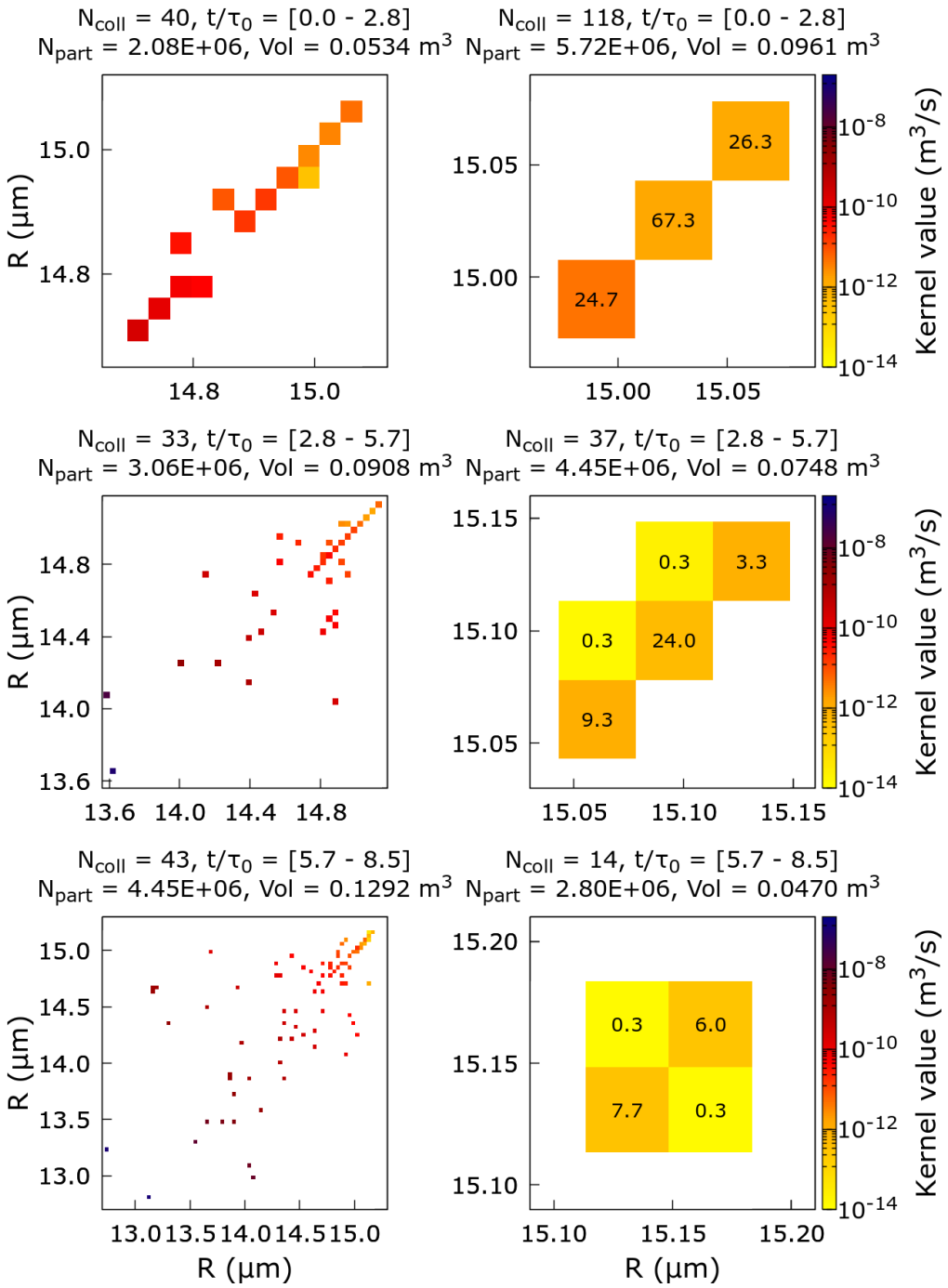

Figure 3.9: **Mono-disperse drop size distribution, unstable and time decaying cloud clear-air interaction. Comparison of kernel value evolution inside the interface region (left) and the cloud region (right). Ensemble average obtained from three realizations from simulation data.**

When looking at the temporal development of the polydisperse population for shorter intervals, the kernel morphology shown by the 256 radius class computation appears to be layered, see Figures 3.10 and 3.11.

The peaks are concentrated in the lateral corners, where the collisions between the smallest and largest drops occur. The intermediate values refer to collisions between large drops. The minimum values refer to collisions between small drops. There is zero probability of collisions occurring between drops with the same radius for each radius value. This trend applies to both the interface and the cloud regions. However, the values within the homogeneous cloud region are generally less than one order of magnitude lower. A total of 10-12 realizations would be sufficient to obtain a statistical base of a few 10^4 events. However, it should be pointed out that the polydisperse population under consideration was built according to a criterion based on a uniform mass distribution. This choice was prompted by the need to observe a population in which the collision rate was mainly expected as a result of the high density of small droplets together with droplets about 30,000 times larger. However, such a distribution is physically not possible, which means that if more physical conditions are considered – with reference to droplet size distributions in the field which are still not fully known - a lower collision rate should be expected. This would increase the number of realizations required to produce sufficiently useful kernel statistics. In this respect, the very recent work of [87], which provides an accurate experimental laboratory evaluation of various theoretical distributions, may be of interest.

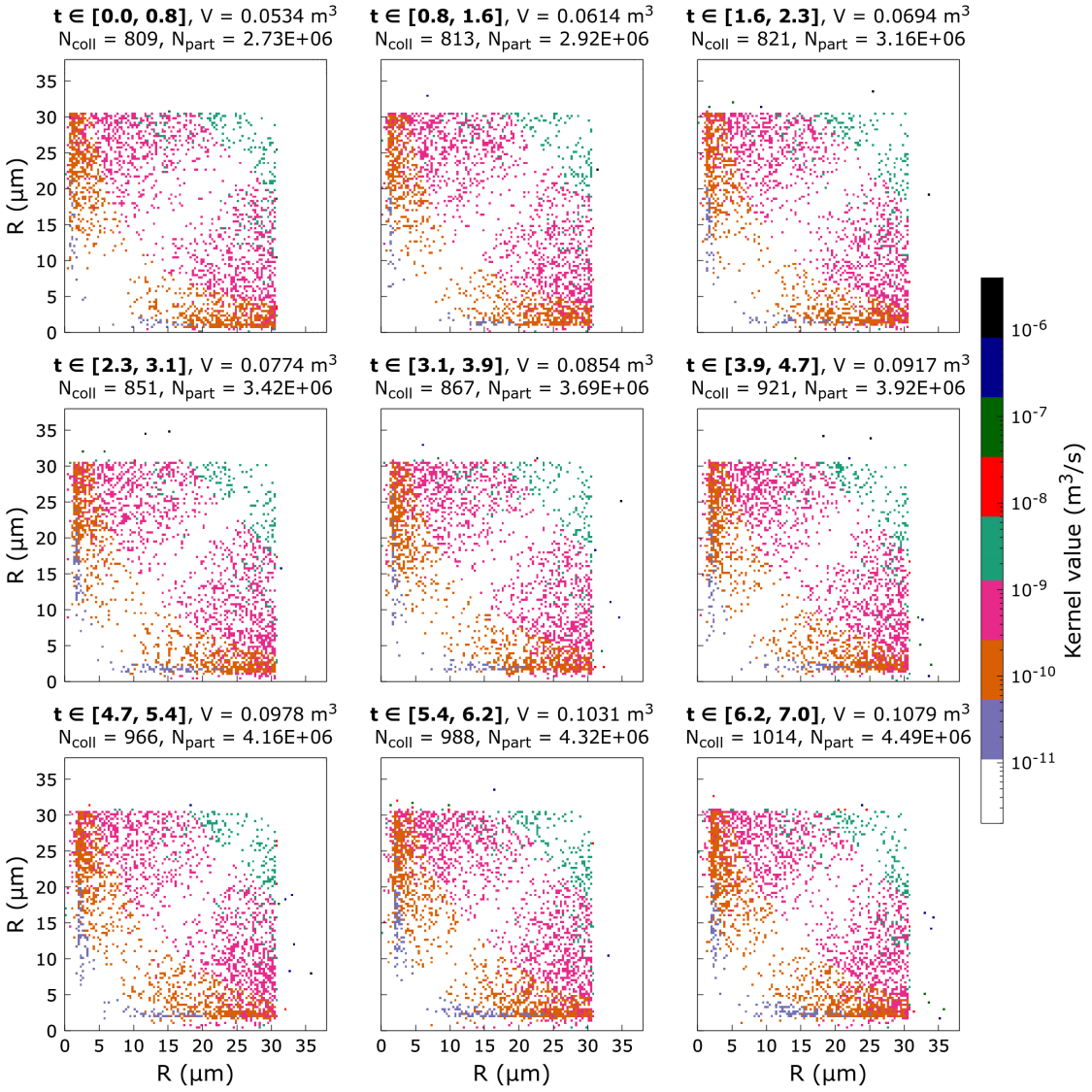

Figure 3.10: **Poly-disperse drop size distribution, unstable and time-decaying cloud clear-air interaction. Kernel value evolution over time inside the interface region. 128 radii classes. Ensemble average over three realization simulation data.**

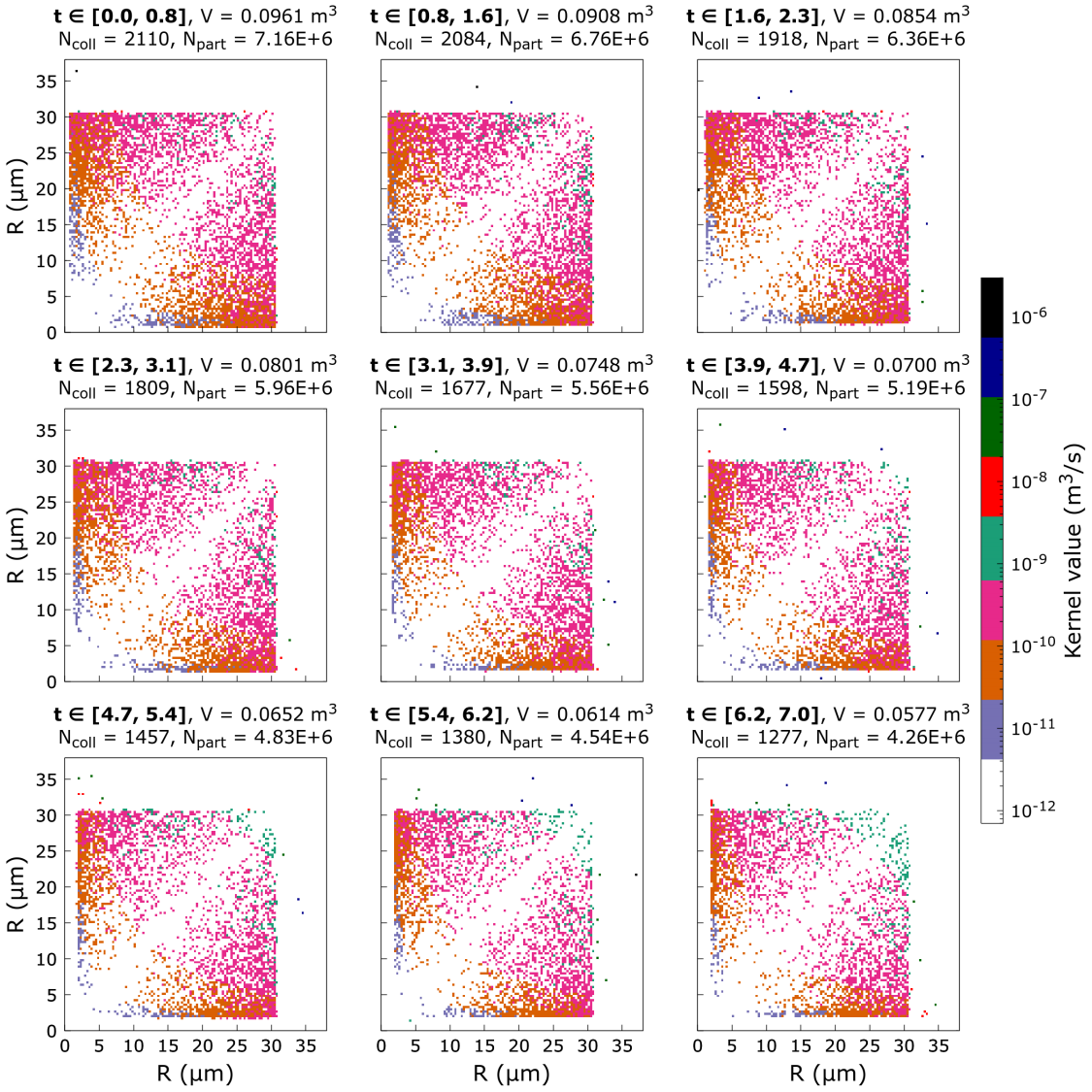

Figure 3.11: **Poly-disperse drop size distribution, unstable and time-decaying cloud clear-air interaction. Kernel value evolution over time inside the homogeneous cloud region with 128 radii classes. Ensemble average obtained from three realizations of simulation data.**

Finally, we would like to briefly discuss the results obtained so far and compared them with the widely accepted theory of Saffman and Turner (1965), which is here referred to as the ST model. This model is still a clear indication of the general interest in the design of multi-phase turbulent flow systems. The Saffman and Turner model apply to background turbulence that is stationary, homogeneous and isotropic. This is a situation that is very different from the system conditions we have investigated here. It is characterized by an unstable density stratification

and the transient decay of an inhomogeneous and anisotropic shearless turbulence that mimics the interaction between a warm cloud component and the clear air that limits it. However, the literature contains no kernel statistics for collisions caused by anisotropic turbulence during temporal decay. Therefore, this type of comparison can be useful to highlight the differences between a near-ergodic system and a completely non-ergodic one. A comparison is shown in Figure 3.12, where the three contributions to the ST model are compared, namely i) collision rate due to different particle inertia resulting from the effect of turbulent acceleration, term A, ii) the gravity effect named as term B, and iii) collision rate due to the spatial variation of turbulent air velocity, term C. The collision kernel for the droplets with inertia (Saffman, 1955) is:

$$\Gamma^{Geo} = 2(2\pi)^{\frac{1}{2}} R^2 n_1 n_2 [(1-\frac{\rho}{\rho_0})^2(\tau_1-\tau_2)^2 \overline{\left(\frac{Du}{Dt}\right)^2} + \frac{1}{3}(1-\frac{\rho}{\rho_0})^2(\tau_1-\tau_2)^2 g^2 + \frac{1}{9}R^2\frac{\epsilon}{\nu}]^{\frac{1}{2}} \tag{3.2}$$

We denote that u is the undisturbed velocity of the air surrounding the droplets. The approximate result for the undisturbed velocity obtained by Batchelor (1951) is:

$$\overline{\left(\frac{Du}{Dt}\right)^2} = 1.3\nu^{-\frac{1}{2}}\epsilon^{\frac{3}{2}} \tag{3.3}$$

This approximation is valid when the Reynolds number of the turbulence is large.

It should be recalled that the ST model is not parameterized with the Reynolds number, which is assumed to be very large. It should be noted that the collision between droplets moving with the air, term C, plays a minor role concerning the terms A and B in this model for $\epsilon = 10$ cm^2/m^3 and an air temperature of 280 K. The two lower fields of Figure 3.12 show the comparison of the ST model with the kernel calculated for the case of the polydisperse droplet population studied in our non-ergodic simulation. The comparison has been performed within a transient part where the dissipation value is not far from the value inserted in the ST model. A significant difference in the kernel values can be observed, which reaches several orders of magnitude. The values seen in the simulation are close to the lowest values shown by the ST contribution C, i.e., the contribution of the collision between droplets moving with the air. The shape of the kernel is also different. However, to derive a completely accurate kernel morphology under non-ergodic, non-homogeneous conditions, it would be necessary to obtain a sufficient number of ensemble averages.

We estimated a large number of ensemble averages, that is, 10-20, numbers that should yield statistics of more than 10^4 collision events in the widely dispersed population, where the probability of droplet collision was considered high. Conversely, in the monodisperse population, the number of ensemble averages should be around 100-200.

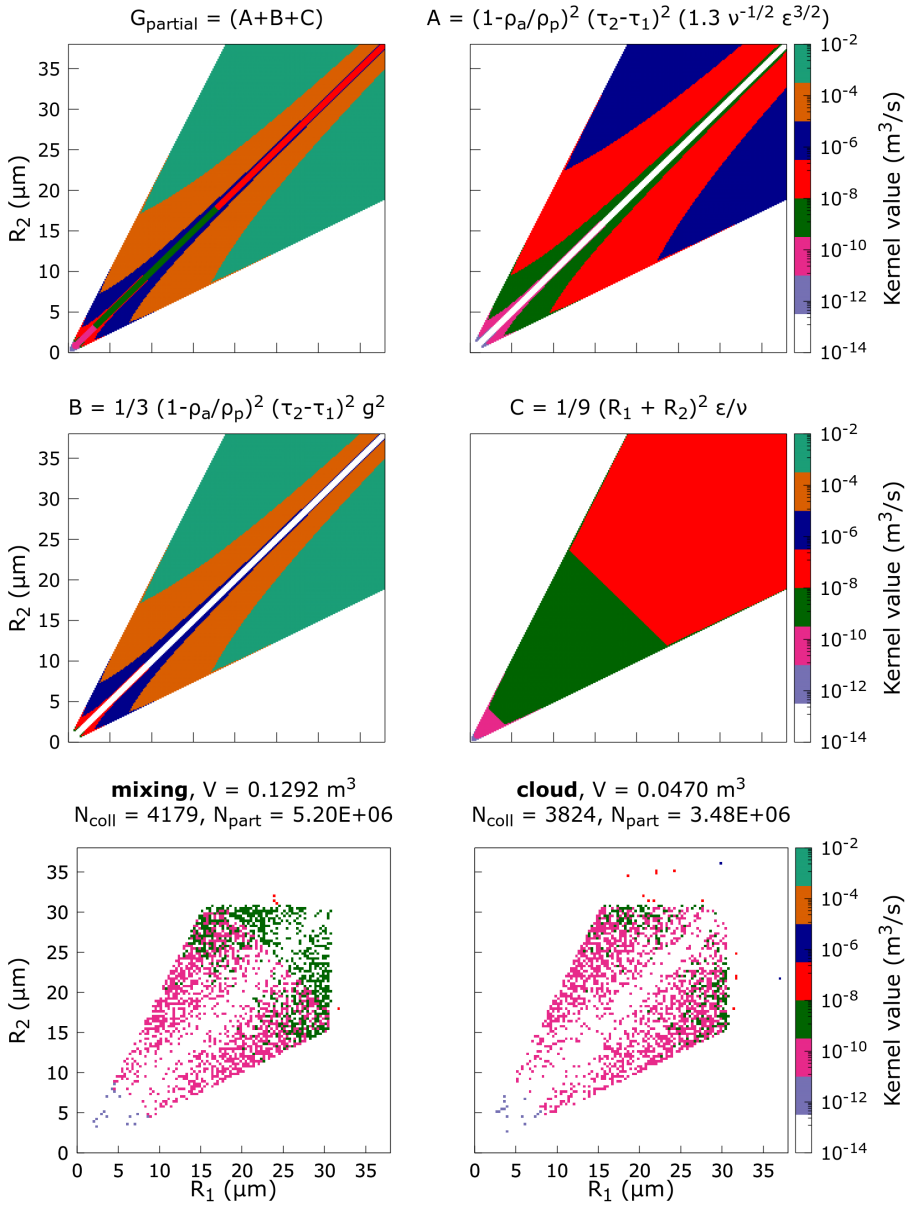

Figure 3.12: **Comparison of the analytical Saffman and Turner model (valid for steady-state homogeneous isotropic turbulence, constant dissipation: $\epsilon = 10\ cm^2/s^3$, $R_1, R_2 \in [0, 38]\ \mu m$, $R_1/R_2 <= 2$ and $R_2/R_1 <= 2$) and our simulation (unsteady, inhomogeneous anisotropic) on kernel statistics in a transient lapse where the dissipation has a comparable value, $t/\tau_0 \in [5.7, 8.5]$. The different terms of Saffman and Turner's model for the given dissipation can be seen in the upper 4 panels. The two bottom panels show kernel statistics for the polydisperse simulation. Left, mixing interface, right, cloud region.**

It is worth to highlight the reason for the extension of the collision kernel features for unsteady anisotropic cloud condition to steady homogenous condition. In a condition where the total water liquid content matches that of a warm cloud, our collision kernel analysis has shown a clear dependence on **time** and **spatial** regions where collisions take place. Thus an extension of the concept of collision kernel is required for a **transient and inhomogeneous system** in which turbulence is decaying faster than the proper time scales of the aqueous phases involved. It is interesting to observe that, due to the dynamical acceleration inside the interface, an asymptotic state for the population droplet-size distribution could be reached more easily inside the interface than inside the decaying cloudy region. For asymptotic state, we mean the long-term state of the droplet population associated to a given structure of the turbulent background airflow, supersaturation, stratification, and total water liquid content.

Our observation suggests that it may be more feasible to determine the kernel function within the interfacial region. Although it must be taken into account that in physical reality, the boundaries of the clouds do not reach true asymptotic states as they are subject to a continuous sequence of transitory phases that are different from each other. And therefore, the search for long-term statistics would not be very meaningful. The comparison with the Saffman-Turner model, valid for a population in conditions of stationary and isotropic turbulence, is partly positive. By placing ourselves in a condition where the number of droplets corresponds to the physical water liquid content of warm clouds and the dissipation of turbulent energy - the only dynamical parameter present in that model - has the same value both in the model and in the numerical simulation, we observe kernel values below those of Saffman-Turner (from a few percents and up to 90%). The morphology is also different, mainly inside the mixing region where a band structure more than a butterfly shape is visible.

3.1.4 Small scale turbulent velocity fluctuation and collision count correlation

To explain physically the observed acceleration of evaporation, condensation, and collision inside the cloud interface, it is important to verify the correlation between intermittency of the fine scale of the turbulence and the collision count for the poly-disperse population transient evolution where we can observe a high rate of collision events. It should be noted that in the shear-free transient decay, the turbulence large scale remains almost unchanged while intermediate and small scales are progressively dissipating. The mixing layer width is concomitantly growing, and a measure of the turbulence penetration in the sub-saturated ambient is given by the displacement of the maxima of the velocity field skewness and kurtosis.

A measure of the intermittency and anisotropy of the smallest scale in the mixing can be obtained in terms of velocity derivative statistics, in particular, in terms of

the longitudinal derivative statistics. We computed the variation along x3, the direction across the interface, of the correlation index (Pearson's product-moment correlation index) in the temporal window observed during the simulation.

The correlation is shown in Figure 3.13. Inside the cloud region, the correlation oscillates about zero but in the mixing; it reaches the value of 0.8 for the velocity derivative standard deviation, and the value of 0.5 for both the velocity derivative skewness and kurtosis of the longitudinal component across the interface. This result highly supports the interpretation that the relative fluid filaments compression across the interface (See, Tordella and Iovieno, PRL, 2011 [43]) foster collision among droplets. This explains how water droplet growth by coalescence, which is due to collisions, can still take place at the cloud border.

It should be noted that Pearson's correlation index is computed between small-scale intermittency of the turbulent air phase velocity and droplet collision count. The correlation is showed via turbulence small-scale anisotropy-related quantities: standard deviation, skewness, and kurtosis of the longitudinal derivative fluctuation in direction x3. Nt is the number of turbulent velocity and droplet collision fields recorded along the transient, in this case, Nt= 33.

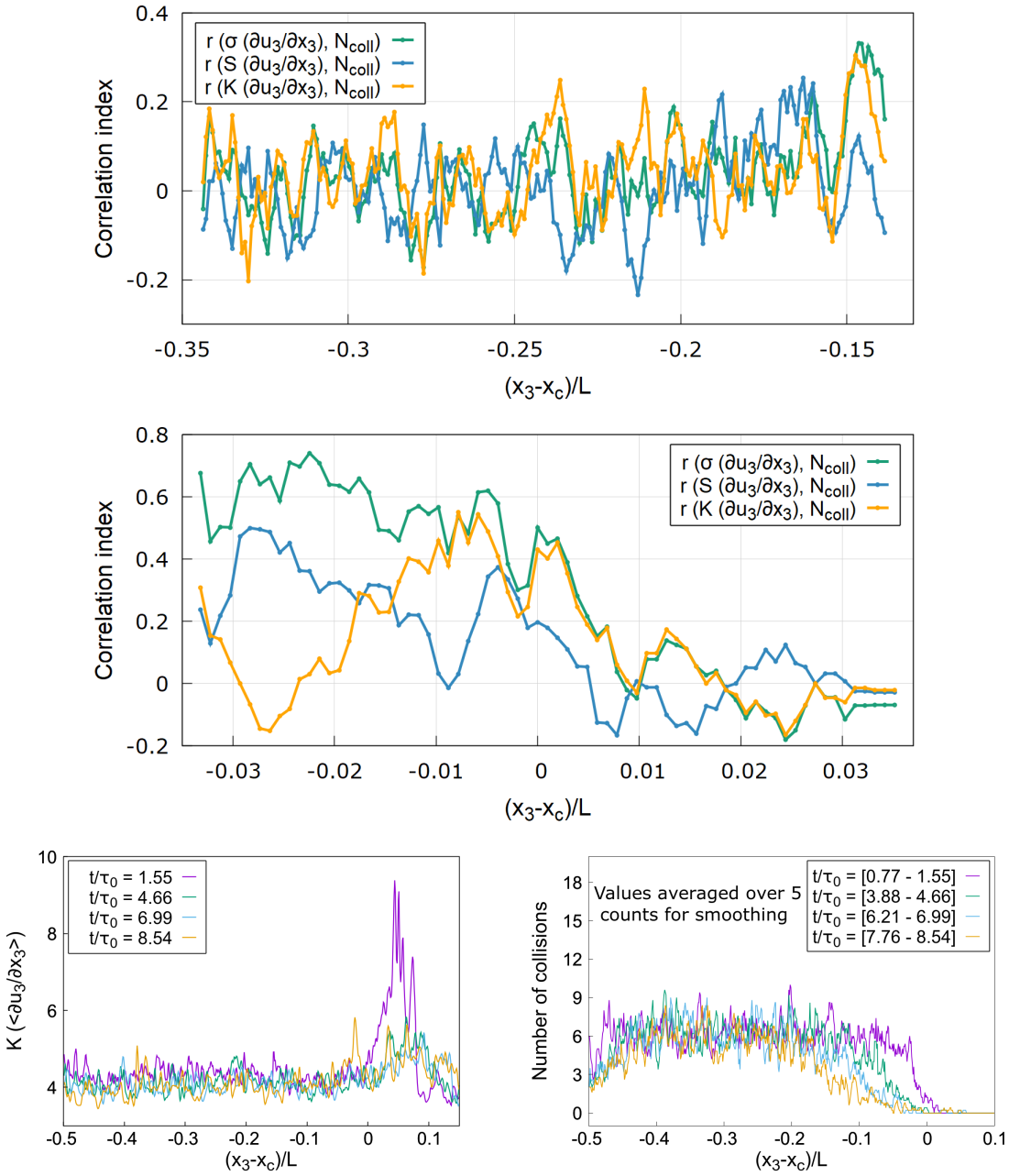

Figure 3.13: **Pearson's correlation index between small-scale intermittency of the turbulent velocity field and the droplet collision count. The collision showed via turbulence small-scale anisotropy-related quantities: standard deviation, skewness, and kurtosis of the longitudinal derivative fluctuation along x3.**

Chapter 4

Diffusion of turbulence inside both stable and unstable stratification perturbations

4.1 Introduction

As has been mentioned in previous chapters, above the boundary layer, stratification in the atmosphere is often stable [140], meaning that a fluid particle that is moved vertically tends to return to its original position. However, unstable perturbations of local stratifications can be anticipated during the phases of cloud formation and disruption. When it comes to local atmospheric dynamics, stratification effects take precedence over terrestrial rotation, see [91], and [48].

Significant progress has been made in our knowledge of turbulence in the presence of intense stratification over the previous few decades. For instance, it is well known that in the context of homogeneous stratified turbulence, initially isotropic turbulence in a stratified fluid quickly transforms into anisotropic turbulence, with the creation of pancake-like structures on its inside [163], [152].

Malinowski et al. in 2013 [120], noted that despite the fact that entrainment is known to need a high level of turbulence, data from most field studies and large-eddy simulations are too poorly resolved to determine the specifics of the interfacial layer. Therefore, we have studied transport across an unsaturated vapor cloud–clear air interface using the DNSs (Direct Numerical Simulations) in this work.

In two recent works Golshan [105], and Fossa [95], we have taken into account turbulent transport without shear in thermal stratification conditions as well as the Lagrangian dynamics of both monodisperse and polydisperse populations of water droplets. However, in this Chapter, I concentrate on the phase that occurs before the formation of a warm cloud with a liquid phase. Accordingly, I focus on the turbulent transport of the unsaturated vapor phase, as a passive scalar, and the related temperature field, as an active scalar. Adopting the two-dimensional stencil

parallelization method enables us to consider a better spatial resolution. Due to a significant communication delay between processes, this three-dimensional DNS code parallelization method cannot be effectively used in the presence of discrete elements, such as water droplets moved in a Lagrangian way. A numerical code for the study of water droplet growth, collision, coalescence, and clustering inside turbulent cloud-clear air interfaces is presented in [157].

Therefore, in this chapter, I focused mainly on the investigation of the evolution of a two-phase, air and unsaturated water vapor, time-decaying, shear-less, and turbulent layer that is spreading in the presence of both stable and unstable perturbations of the normal temperature lapse rate. I have considered how the dynamics of the smallest scales of an airflow affect the thermal turbulent transport and vapor. To better understand the fundamental phenomena that take place at the vapor cloud-clear air interface across length scales of the order of a few meters, I have simulated an idealized arrangement. Under these circumstances, I have resolved scales ranging from a few meters to a few millimeters, or only the small-scale fraction of the inertial range and the dissipative range of the power spectrum in a relatively limited region of the atmosphere over a vapor cloud-clear air interface. As a result, I have been able to evaluate the entrainment dynamics that take place on a scale smaller than that explicitly resolved in large-eddy simulations of clouds at a thin layer near the top of the cloud; for details, please see [35].

Stratification and a turbulent kinetic energy gradient are two concurrent characteristics of the top mixing layer of a vapor cloud that has been the subject of this preliminary work. We have not taken into account mechanisms like wind shear or radiative cooling, which are crucial when buoyancy reversal is present [121] and [122]. Here, I included the Lagrangian dynamics of both monodisperse and polydisperse populations of water droplets and the same physical simulation set-up that are already discussed in Chapters 2 and 3.

The 3D numerical simulations were performed within a $6m \times 6m$ wide and 12m high domain inside two cubes that are attached to each other. In this part of the study, the Taylor microscale Reynolds number was 250 inside the cloud portion. The squared Froude's number varied over intervals of [0.4; 981.6] and [4.0; 19.6]. The Prandtl number considered here is Pr= 0.74, and the Schmidt number Sc= 0.61 (standard atmosphere, altitude of 1000 m s l).

4.2 Physical problem and reviewed equations

In this section, I investigate the interaction between two turbulent regions separated by a thin interface. The two regions are assumed to contain two homogeneous and isotropic turbulent fields with initially different turbulent kinetic energy levels. The two regions also differentiate for the humidity (water vapour density). Numerically, this flow configuration is simulated by considering a $6m \times 6m \times 12m$ parallelepiped domain, discretized with $1024 \times 1024 \times 2048$ grid points.

The initial turbulent velocity field has been chosen to allow to simulate the inertial an dissipative range of an atmospheric boundary layer, according to in situ observations; See figure 4.1. Computational limitations do not allow to simulate all the flow scales, so that the largest scales are not simulated. Anyway, small-scale effects are difficult to measure and need to be parametrized in cloud-resolving models.

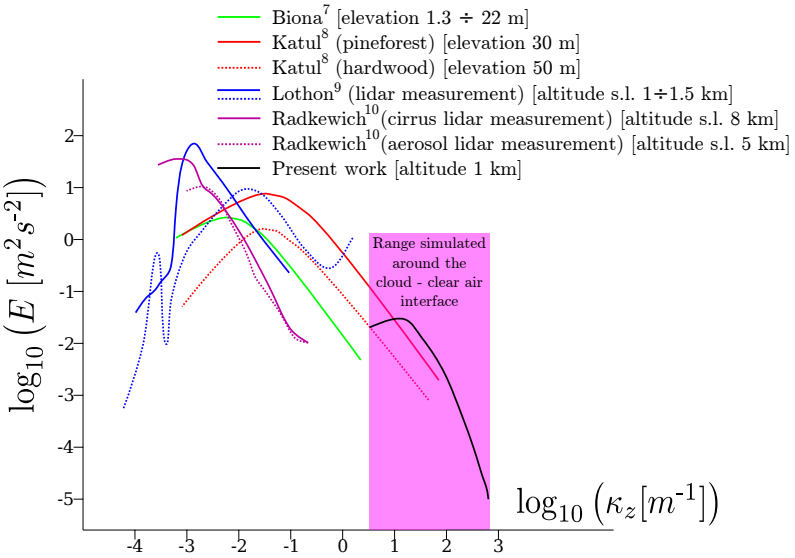

Figure 4.1: **Kinetic energy spectra. Contextualization of the present study (black spectrum, inertial small-scale and dissipative ranges) to in-situ atmospheric measurements (colored spectra: energy injection and low wave-number inertial scales). The aim of the current simulations is to represent the small-scale range of the spectrum that in situ measurements have not been able to detect.**

As the scheme in Figure 4.2 shows, the interaction between the two homogeneous turbulent fields produces a shearless mixing layer, whose thickness δ grows in time remaining roughly proportional to the integral scale ℓ of the flow, which in all the simulations is initially equal to 3×10^{-1} m. The ratio of kinetic energy between the two regions is 6.7. This energy ratio is of the same order as the ones measured in warm clouds (see, for example, [120].) and allows us to compare our results with laboratory and computer experiments on turbulent shearless mixing in the absence of any stratification (see, [43] and [147].). Buoyancy is considered through (2.5), (2.6), (2.7). The initial velocity conditions are randomly generated in the wavenumber space as a sum of independent Fourier modes with random phased and a prescribed spectrum. Then a short preparatory simulation is run before the field is used as the initial condition for the simulation in order to allow the creation of turbulent correlations. The initial conditions for the vapor are given by equation (2.4), which produces a uniform humidity in both zones and a smooth transition across a thin layer to avoid numerical issues due to the Gibbs phenomenon. The Prandtl number taken into account here is Pr= 0.74. In Figure 4.2 and Table 4.1 the initial conditions for the temperature perturbation are presented.

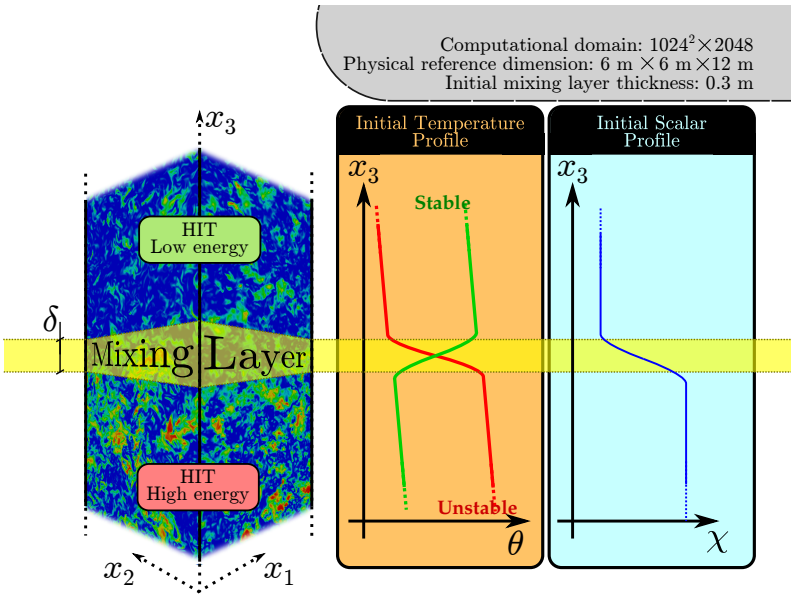

Figure 4.2: **Scheme of the initial conditions.** E_1 **is the mean initial turbulent kinetic energy below the shear-less mixing layer (cloudy, HIT high energy region),** E_2 **is the same, but for the top (clear air, HIT low energy region). We assume** $E_1/E_2 = 6.7$ **for this model of the top interface. The stratification inside this interfacial mixing is represented by a local temperature perturbation with respect to the neutral profile; the perturbation can be either stable or unstable. The unsaturated vapor (passive scalar) is initially only present in the cloudy high-energy region. The direction of gravity is opposite to the positive** x_3**.**

4.3 The evolution of the Froude number

The Froude number is used to indicate the proportion of inertial to buoyancy forces and is defined as (4.1):

$$Fr = \frac{U_{(}rms)}{l\mathcal{N}} \tag{4.1}$$

Where the Brunt-Väisälä frequency is defined as:

$$\mathcal{N} = \sqrt{g\alpha \frac{\partial \theta}{\partial x_3}} \tag{4.2}$$

Where u is the root mean square of the velocity fluctuation at the lower border of the interfacial layer, l is the macroscale length inside the cloudy region, θ is the mean temperature and g is the gravitational acceleration. The α is the thermal expansion coefficient.

Table 4.1: **Essential simulation parameters and values used for initial conditions**

Quantity	**Symbol**	**Value**	**Unit**
Domain size	L x L x L_3	6 x 6 x 12	m^3
Domain discretization	N x N x N_3	1024 x 1024 x 2048	-
Grid step	Δx	$5.86 \cdot 10^{-3}$	m
Initial rms velocity (cloud)	u_{rms}	0.2	m/s
Initial energy ratio (cloud-clear air)	E_1/E_2	6.7	-
Initial integral scale	ℓ_0	0.3	m
Initial dissipation rate (cloud)	ε_1	0.025	m^2/s^3
Kinematic viscosity of air	ν	$1.57 \cdot 10^{-5}$	m^2/s
Initial Kolmogorov time (cloud)	$\tau_{\eta 0} = (\nu/\varepsilon_1)^{1/2}$	$2.51 \cdot 10^{-2}$	s
Initial Kolmogorov length scale (cloud)	$\eta_0 = \left(\nu^3 \ell_0 / u_{rms}^3\right)^{1/4}$	$6.17 \cdot 10^{-4}$	m
Initial eddy turnover time	$\tau_0 = \ell_0/u_{rms}$	1.5	s
Initial Reynolds number (cloud)	$\mathrm{Re}_\ell = u_{rms}\ell_0/\nu$	3821	-
Initial Taylor microscale Reynolds number	$\mathrm{Re}_\lambda = u_{rms}\lambda/\nu$	250	-
Thermal expansion coefficient	α	$3.55 \cdot 10^{-3}$	K^{-1}
Prandtl number	Pr	0.74	-
Schmidt number	Sc	0.61	-
Atmospheric lapse rate	G_0	0.0065	K/m^{-1}

The initial square of the Froude number value is ranged from the negligible stratification about 981.6 to the strong stable stratification selected as 0.4.

In this study, we used the square of the Froude number value due to the reason of considering the unstable cases. Inside the unusable cases, the square of the Brunt-Väisälä frequency value for the initial temperature gradient is negligible. The evolution of the square of the Froude number is represented in Fig 4.3.

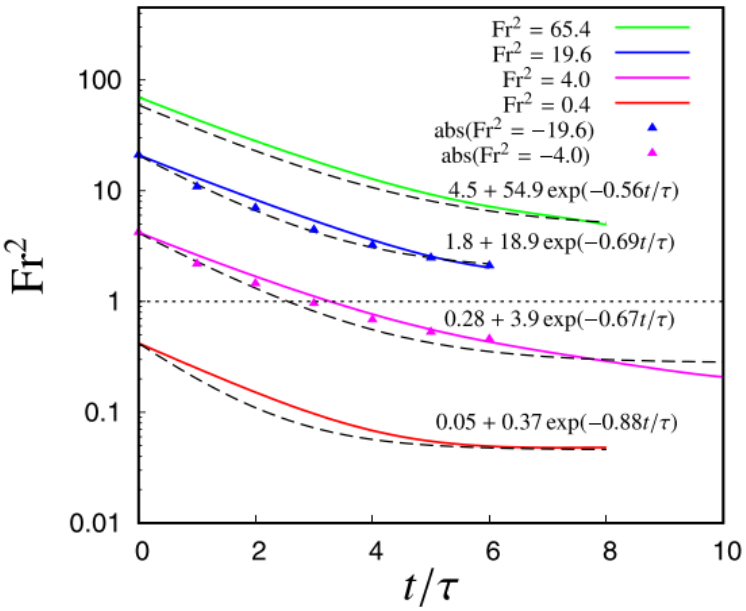

Figure 4.3: **Time evolution of the instantaneous Froude number for the simulations with stable stratification.**

By looking at the Figure 4.3, once can notice that a higher level of stratification is occur when the Froude number is small. Dashed lines represent the fitting exponential laws of these temporal decays. The initial values for startification is represented in Table 4.4 and Table 4.2

Level	$\nabla_z\theta_{ic}$ (K m^{-1})	$\Delta\theta$ (K)	$\mathcal{N}_{ic}$ (s^{-1})	Fr	Fr^2	Re$_b$	Intensity
$2G_0$	1.3×10^{-2}	4.0×10^{-3}	2.13×10^{-2}	31.3	981.6	0.7	Neutral
$30G_0$	2.0×10^{-1}	6.0×10^{-2}	8.24×10^{-2}	8.09	65.4	10.9	Quasi-neutral
$100G_0$	6.7×10^{-1}	2.0×10^{-1}	1.50×10^{-1}	4.43	19.6	36.3	Intermediate
$500G_0$	3.3	1.0	3.36×10^{-1}	2.00	4.00	181.7	High
$5000G_0$	3.3×10^{1}	1.0×10^{1}	1.06	0.62	0.4	1817.2	Extreme
$-100G_0$	-6.7×10^{-1}	-2.0×10^{-1}	...	...	−19.6	−36.3	Unstable, intermediate
$-500G_0$	−3.3	−1.0	...	...	−4.00	−181.7	Unstable, high

Figure 4.4: **Temperature gradient values (second column) are also expressed in terms of $G_0 = 0.0065$ in the first column. $\mathcal{N}_{ic} = \sqrt{\alpha g \frac{\partial\theta}{\partial x_3}}$ is the characteristic Brunt-Väisälä frequency of the initial condition (suffix ic). The Froude number, Fr$= \frac{u_{rms}}{\mathcal{N}_{ic}\ell}$, and the Reynolds Buoyancy Number, Re$_b = \frac{\varepsilon\mathcal{N}_{ic}^2}{\nu}$, offer an indication of the order of magnitude of the buoyancy forces, compared with the inertial terms (ε is the initial energy dissipation rate, ℓ is the initial value of the spatial integral scale and ν is the kinematic viscosity of air, see Table 4.1 for corresponding values).**

Froude number	**Fitting parameters**	**Asymptotic Standard Error**
$\mathrm{Fr}^2 = 65.4$	$b = 4.5, n = 54.9, u = 1.8$	$\triangle_b = 5.5\%, \triangle_n = 1.7\%, \triangle_u = 2.8\%$
$\mathrm{Fr}^2 = 19.6$	$b = 1.8, n = 18.9, u = 1.44$	$\triangle_b = 15.4\%, \triangle_n = 2.2\%, \triangle_u = 5.8\%$
$\mathrm{Fr}^2 = 4.0$	$b = 0.28, n = 3.9, u = 1.5$	$\triangle_b = 10.5\%, \triangle_n = 1.7\%, \triangle_u = 3.9\%$
$\mathrm{Fr}^2 = 0.4$	$b = 0.05, n = 0.37, u = 1.13$	$\triangle_b = 2.8\%, \triangle_n = 0.7\%, \triangle_u = 1.8\%$

Table 4.2: **Exponential fits, $f(x) = b + n\exp^{-x/u}$, of the temporal decay of the Froude numbers shown in Fig. 4.3**

4.4 Spatial statistical properties inside different stable and unstable environments

The statistical behavior of the velocity and scalar fields have been analyzed for the selected system based on chosen initial condition and chosen simulation set up.

By averaging the variables in the planes (x_1, x_2) normal to the mixing direction x_3, the statistics are computed as the average operator:

$$\langle\cdot\rangle(x_3) = \frac{1}{2^{20}} \sum_{i=1}^{2^{10}} \sum_{j=1}^{2^{10}} \cdot (x_{1,i}, x_{2,j}, x_3). \tag{4.3}$$

The scalar fields θ and χ and the variance of the turbulent kinetic energy of the velocity field which is defined as:

$$E = \frac{1}{2}\left(\langle u_1^2\rangle + \langle u_2^2\rangle + \langle u_3^2\rangle\right) \tag{4.4}$$

That are used to calculated the second-order moment.For the high-order moments, the skewness and kurtosis (third- and fourth-order moments normalized by means of the variance), are implemented.

$$S(\cdot) = \langle \cdot^3\rangle / \langle \cdot^2\rangle^{1.5} \tag{4.5}$$

$$K(\cdot) = \langle \cdot^4\rangle / \langle \cdot^2\rangle^{2} \tag{4.6}$$

It should be noted that the definition of skewness and kurtosis for passive scalar field χ differs slightly from the one given in the previous equation. Because of the proximity of the external regions, where the variance $\langle\chi^2\rangle$ vanishes, in order to prevent numerical problems, the actual definitions of skewness and kurtosis are modified as

$$S(\chi) = \langle\chi^3\rangle / \left(\langle\chi^2\rangle + 0.005\langle\chi^2\rangle_{\max}\right)^{1.5} \tag{4.7}$$

$$K(\chi) = \langle\chi^4\rangle / \left(\langle\chi^2\rangle + 0.01\langle\chi^2\rangle_{\max}\right)^{2} \tag{4.8}$$

where $\langle\chi^2\rangle_{\max}$ indicates the maximum variance value along direction x_3. In order to analyze an intermittent behavior of the turbulent shear-less mixing, two essential indicators are used skewness and kurtosis distributions.

It's crucial here to emphasize that the shear-less turbulent mixing is highly intermittent. To do the statistical study of the turbulent shear-less mixing, skewness and kurtosis distributions are frequently used since they are the main markers of intermittent behavior. Let's cite a few of these properties for the benefit of readers unfamiliar with the topic: the proof of the small scales' anisotropy [43], prerequisite for the divergence from Gaussianity [44], the measure of the mixing center's displacement, which is typically calculated using the skewness peak displacement, the reason why the first two velocity fluctuation moments are insufficient to describe the phenomenon, [147], [84], [142] [143] and the role of macroscale spatial variation as a source of intermittency and kinetic energy gradients [41].

The evolution of the system can be divided into two major stages based on the evolution of the ratio between the buoyancy force and the other dynamical effects (advection and diffusion), as well as by examining the statistical behavior of the turbulent kinetic energy shown in Fig 4.5. No appreciable variations from a nonstratified situation arise as long as the ratio stays small. But when the significance of the stratification perturbation increases, buoyancy effects take over and variations emerge from both the quantitative and qualitative perspectives.

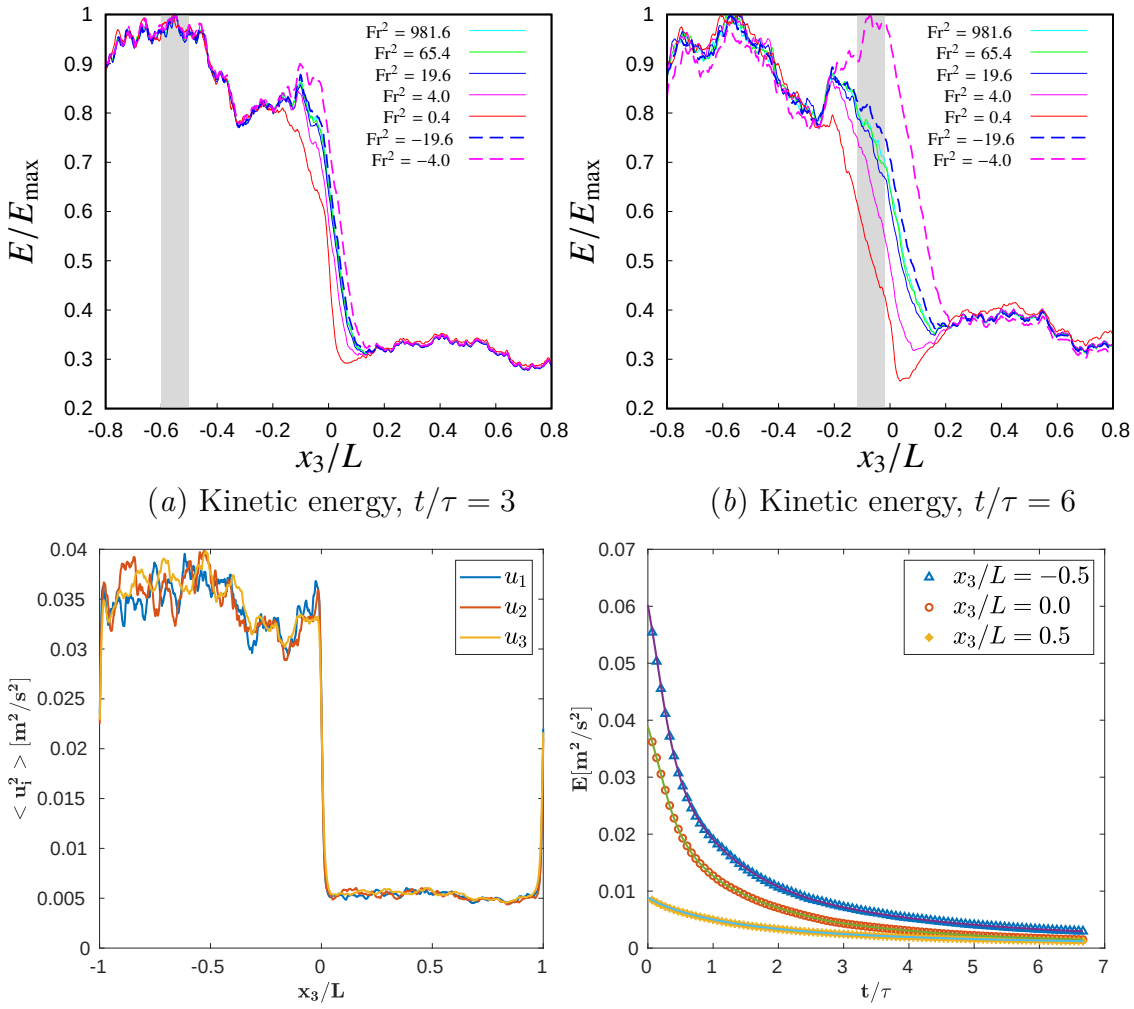

(*a*) Kinetic energy, $t/\tau = 3$ (*b*) Kinetic energy, $t/\tau = 6$

(*c*) Initial velocity variance. (*d*) Energy time decay

Figure 4.5: **Turbulent energy along vertical direction x_3, computed from the velocity variance in the horizontal planes, x_1-x_2, panels *a* and *b*: $t/\tau =$ 3 and 6, respectively. The data are taken from simulations with different levels of stratification, which are represented by the initial reference squared Froude number. Panel *c*: distribution of the initial velocity variance across the computational domain. Panel *d*: turbulent kinetic energy decay inside the unsaturated cloud (blue triangles), the interfacial mixing layer (red circles), and the clear air region (yellow diamonds).**

When comparing the turbulent kinetic energy at two different instants, in Fig. 4.5(a) and Fig. 4.5(b), where t is the initial eddy-turnover time, it is easy to see the effects of various stratification levels. The location of the energy gradient is slightly displaced lower when the buoyancy component is comparable to the other forces. The onset of a sublayer that is indicated by a time-dependent widening of the pit of turbulent kinetic energy can then be seen. Due to the creation of two interfaces in this scenario, the presence of such a sublayer alters the dynamics of the system. The high-turbulent energy region is separated from the pit by the first, which would also exist in the absence of stratification. The second one, which would not exist without stratification, divides the mixing layer's center from the area with low turbulent energy. Thus, a strong stable stratification causes a sort of physical separation between the regions below and above the mixing layer, greatly reducing their interaction. On the other hand, under unstable situations, a rise in the turbulent kinetic energy within the mixing region—a sort of peaky sublayer—can be seen. Once again, in this instance, we see the development of a secondary energy gradient, but this time it is located in the opposite direction from the stable scenario. The peak and the high-energy zone, where the vapor cloud is located, are now separated by the secondary gradient. Thus, a strong stable stratification causes a sort of physical separation between the regions below and above the mixing layer, greatly reducing their interaction. On the other hand, under unstable situations, a rise in the turbulent kinetic energy within the mixing region—a sort of peaky sublayer—can be seen. Once again, in this instance, we see the development of a secondary energy gradient, but this time it is located in the opposite direction from the stable one. The peak and the high-energy region, where the vapor cloud is located, are now separated by the secondary gradient. In fact, the peak is moved nearer the high-energy region (while the pit is closer to the low-energy one).

Parts of the flow are intermittently affected by the primary energy gradient and the second one (if it is present). Figure 4.6 displays the vertical velocity fluctuations' skewness, kurtosis after six timescales (panels (a) and (c), respectively), and time evolution of their maximum and lowest values [panels (b) and (d)].

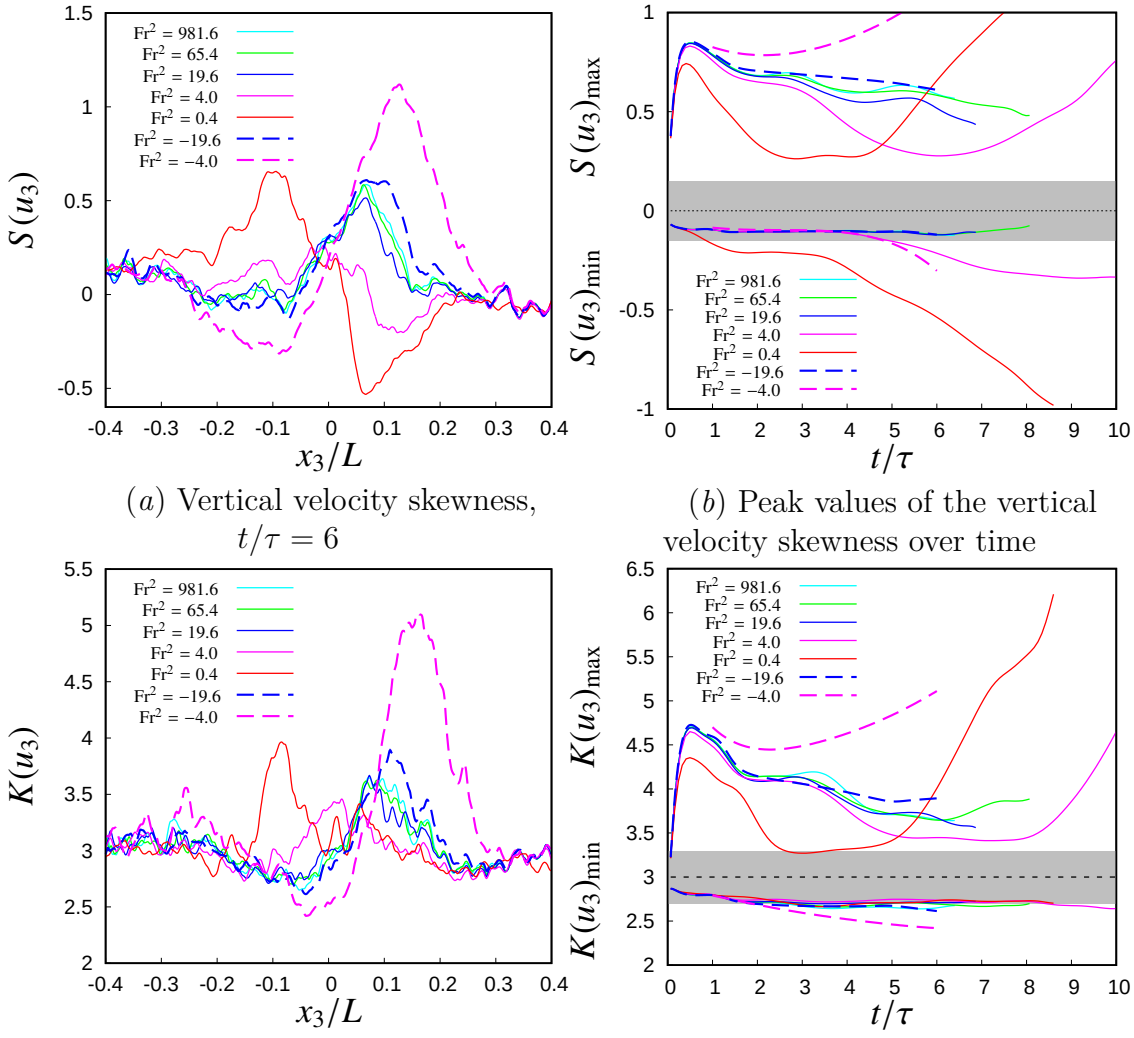

(*a*) Vertical velocity skewness, $t/\tau = 6$

(*b*) Peak values of the vertical velocity skewness over time

(*c*) Vertical velocity kurtosis , $t/\tau = 6$

(*d*) Peak values of the vertical velocity kurtosis over time

Figure 4.6: **Vertical velocity skewness (panels *a*-*b*) and kurtosis (panels *c*-*d*) along vertical direction x_3, computed from vertical velocity central moments in the horizontal planes $(x_1 - x_2)$. The data are taken after 6 τ (panels *a*-*c*) and over the temporal evolution (panels b-d). Simulations with a different stratification are represented by the square Froude number. The gray band in panels b and d represents the intermittency range measured outside the mixing layer.**

Generally, it is possible to see a decline in the maximum values, which decay considerably more quickly than in the nonstratified or weakly stratified situations. Low intermittency, which is defined by values as low as those reported outside the mixing anisotropic region, results from the quick decay that occurs during pit formation (the "normal" range is depicted by a gray band in panels b and d of Fig. 4.6). After that, S and K increase quickly, reaching larger values than in the unstratified situation.

In the unstable stratification situation, the intermittency decay is instantly stopped, and for the Fr2=- 4.0 case, an increase of S and K is seen beyond 3 timescales. The final configuration appears to be more variable at the end of the numerical simulation in both the stable and unstable instances, with values that can even double compared to the unstratified condition.

The statistical characteristics of temperature variation of the active scalar, and the concentration of the vapor passive scalar, χ, are analogous.

In fact, the buoyancy term inside the momentum equation has a stronger influence than the non-differential term $u_3 G_0$ in the energy equation.

Since it is vectorial, the latter effectively absorbs and transfers the gravitational influence to the velocity field. According to our simulations, the transport of temperature in the vapor field, which is a straightforward passive scalar field, is comparable to the transport caused by advective-diffusive Eq. 2.4; for example, look at Fig. 4.7, where the first four statistical moments across the interface are shown at t/t=6. The effects on scalar fields are less severe than those observed on velocity. The stratification level determines how wide the zone with nonzero variance is, and for stable cases, the region becomes thinner. In the case of extremely strong stratification, such as with Fr2=0.4, significant variances can be seen. In circumstances when stratification is stable, scalar fluctuations are muted, whereas they are significantly exacerbated when it is unstable. The shrinking of the mixing layer becomes notable after the onset of the pit of energy and is connected to the decrease in entrainment. For a comprehensive overview, refer to Gallana's Ph.D. thesis. 32 [96].

See the panels in the second, third, and fourth rows of Figure 4.7 for more information on how the high-order moments initially follow the same pattern as the velocity variations, with S and K decreasing when the stratification is stable and increasing when it is unstable. After a few time scales, a significant difference can be seen in the stable stratification condition. In this case, the energy pit prevents mixing, and the high-order statistics values tend to be almost constant.

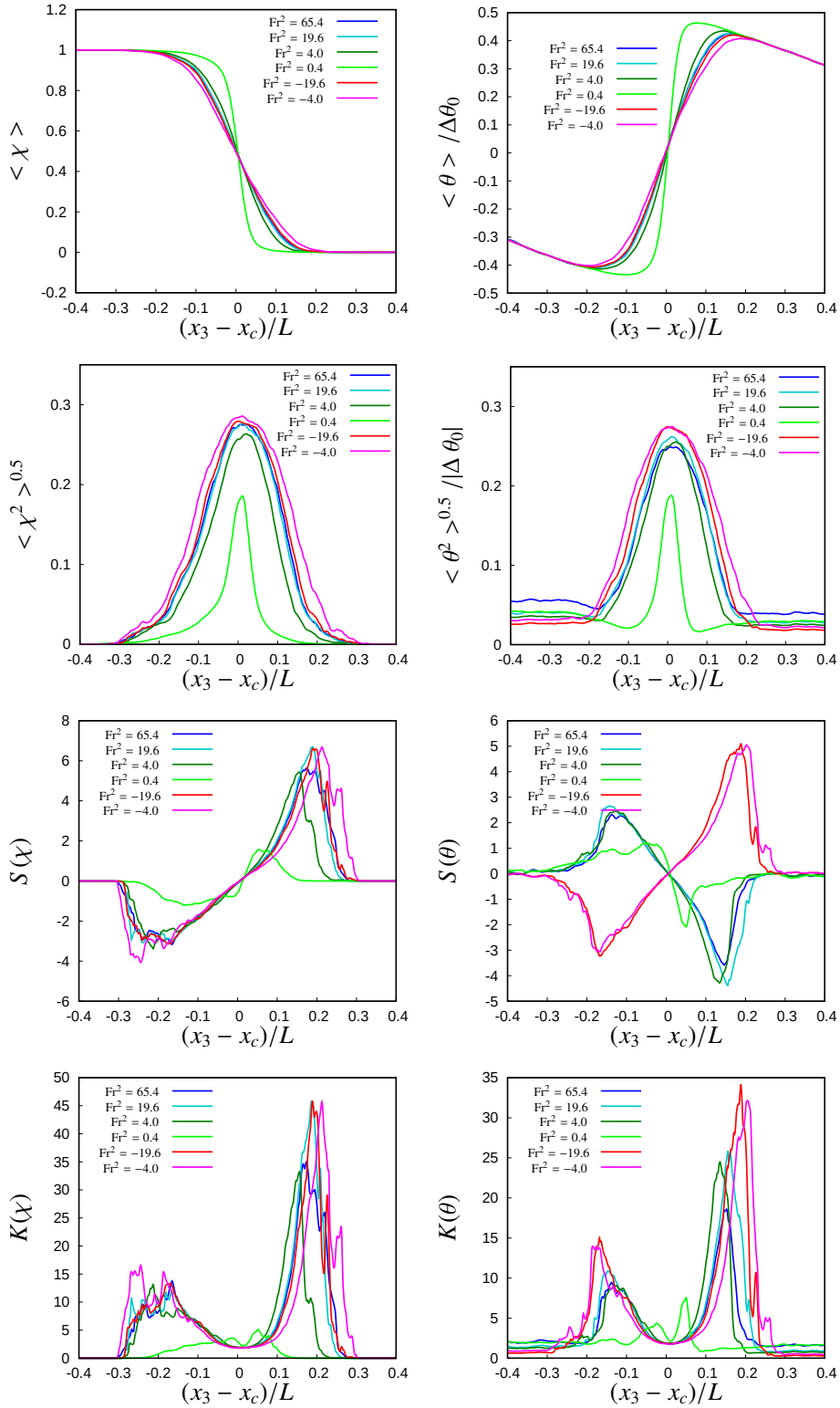

Figure 4.7: **Comparison of the passive (left) and active (right) scalar statistics,** $t/\tau = 6$**.**

It's also interesting to notice that the existence of a population of either monodisperse- or polydisperse water drops has little to no impact on the morphology of the spatial distribution of the vapor statistics, or the passive scalar. Indeed, if a comparison is made between our simulations containing the aqueous phase, which is equivalent in quantity to what is present inside warm clouds (LWC, liquid water content, equal to $0.8gr/m^3$), see Golshan et al. 2021 [105] and the work of Fossa' et al. 2022 [95] which was carried out under almost the same Froude numbers, it can be seen that only the temporal evolution of the maximum and minimum peaks of the vapor statistical distributions is in fact affected, albeit only slightly, by the presence of drops, and by the related phenomenology of evaporation–condensation and collision–coalescence, see Fig.4.8.

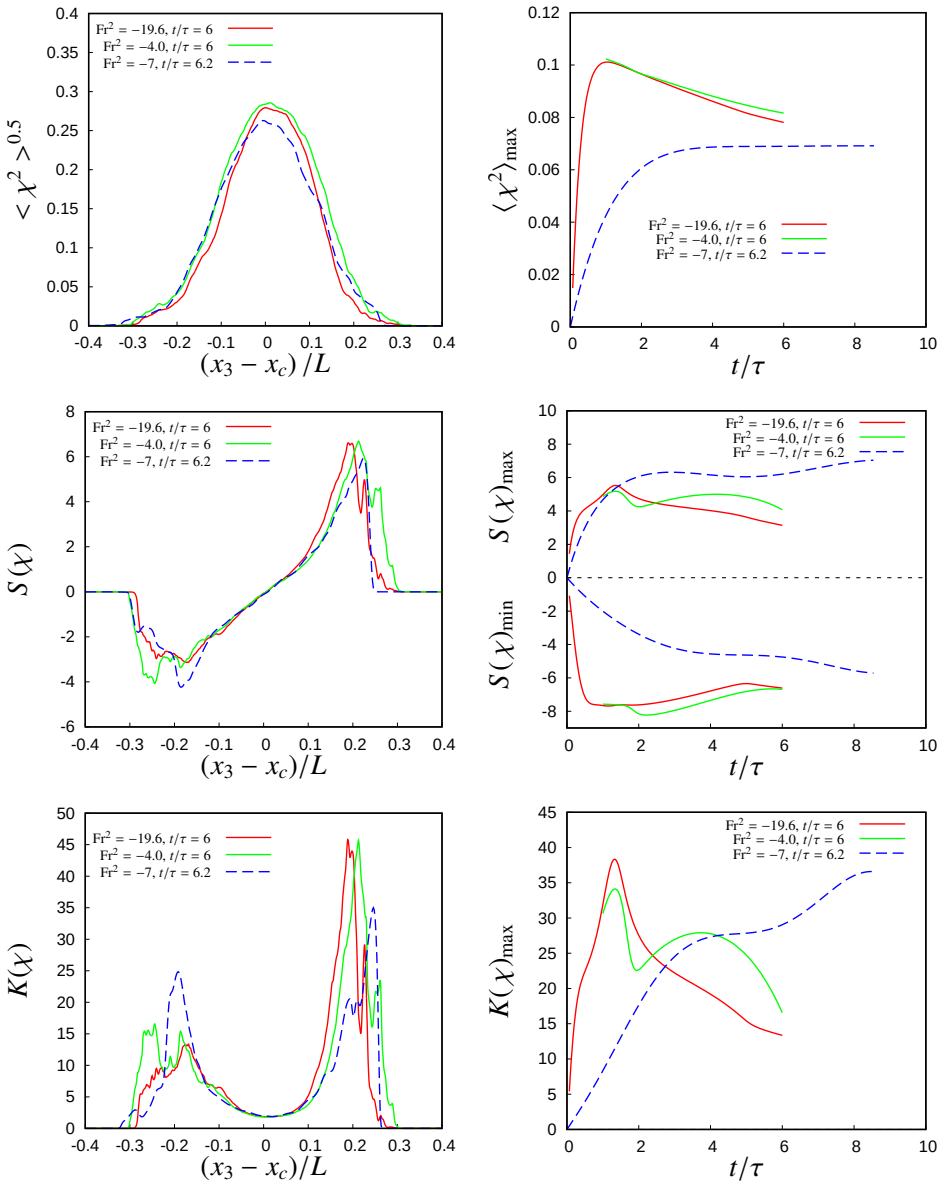

Figure 4.8: **Comparison of vapor moment statistics for simulations with droplets (dashed) and without (solid, same data as shown in the left column of Fig. 4.7).**

Additionally, the kurtosis function's maximum values vary and do not eventually settle at the same asymptotic values; for example, see the bottom right panel of Figure 4.8. In addition, it can be seen that the thinning of the mean temperature profile with increasing stratification, which thins by about four times as the stratification increases from neutral to Fr= 0.4, or 5000 G_0, is consistent with that measured by Jayesh and Warhaft [84], in particular, the curve where the mean temperature profile half width is normalized by the integral length scale of the large-scale turbulence on the lower side of their measurement.

We compare the outcomes of a related laboratory investigation conducted in 1994 at Cornell University by Jayesh and Warhaft [84] as a means of validating our simulations. In the mentioned experiment, a stably stratified interface with turbulent air below and clear air above was examined in a wind tunnel to mimic the circumstances at the inversion cap at the top of the atmospheric boundary layer. Thus, this system is identical to the one in our study in terms of the transport of momentum, turbulent energy, and temperature, even if the transport of the passive scalar is absent. They used a composite grid to generate the interfacial layer, with a small mesh size above and a big one below.

In the laboratory investigation, a uniform mean flow with varying levels of turbulence above and below the interface is used to generate the steady-state system. In contrast, the current numerical models are in temporal decay. There is no mean flow in the background.

Although the comparison is qualitative rather than quantitative due to the differences between the Richardson and Reynolds numbers ($Ri = 0.8, x/M = 32$, and $Ri = 63, x/M = 148$, in JW; $Ri = 0.11, t/\tau = 2.5$, roughly equivalent to $x/M = 40$, and $Ri = 18.2, t/\tau = 3.2$, roughly equivalent to $x/M = 48.32$, in the this study), the laboratory and numerical statistical trends are very similar see Fig. 4.9.

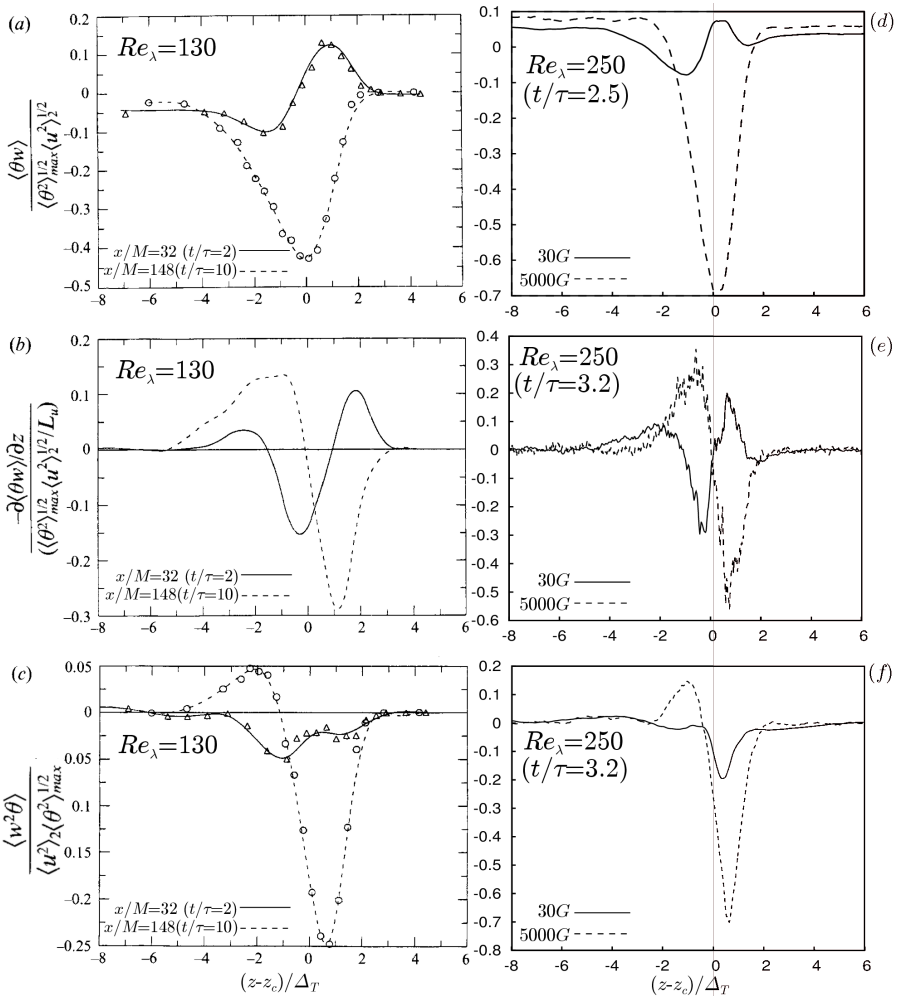

Figure 4.9: **Comparison of the flow statistics between the Jayesh and Warhaft laboratory experiment (J. Fluid Mech. 277 (1994), p. 29) (left column, spatial evolution) and the present numerical experiment (right column, temporal evolution). In their experiment, Jayesh and Warhaf considered a turbulent mixing between two regions with different kinetic energies and temperatures (see Figure 2). The velocity fluctuations were generated by forcing a flow into grids of different mesh sizes. Jayesh and Warhaft's data refer to $Ri = 0.8 (x/M = 32$, dashed line) and $Ri = 63 (x/M = 148$, solid line). By using a Taylor transformation, it is possible to see that $x/M = 32$ corresponds to a 2 time scale long temporal evolution, while x/M=148 corresponds to a 10 time scale long temporal evolution. The flows simulated in this work refer to $Ri = 0.11$ (30G case, dashed line) and to $Ri = 18.2$ (5000 G case, solid line). In panel (d), $t/\tau = 2.5$, while in panels (e) and (f), $t/\tau = 3.2$. Panels (a) and (d): temperature flow. Panels (b) and (e): derivative normal to the mixing of the temperature flux. Panels (c) and (f): the temperature fluctuation flux (correlation between the second-order moment of the velocity fluctuation across the layer and the temperature fluctuation).**

Here, the distributions of the temperature flux fluctuations, its spatial derivative, and the covariance between $< u_3^2\theta' >$ are displayed over the mixing layer. The coordinates x_3 and u_3 in Jayesh and Warhaft [84] are represented by z and by w, respectively.

It is important to consider the opposite sign of the temperature flux inside the weak turbulence region, which translates into a counter-gradient heat flux (see also Riley, Metcalfe, and Weissmann 1981 [81] and Yoon and Warhaft 1990 [93]).

The turbulent kinetic energy flow is correlated with the trends across the layer between our numerical experiment and JW's laboratory experiments (see Fig. 17, panel (a) in JW and our Fig. 4.10).

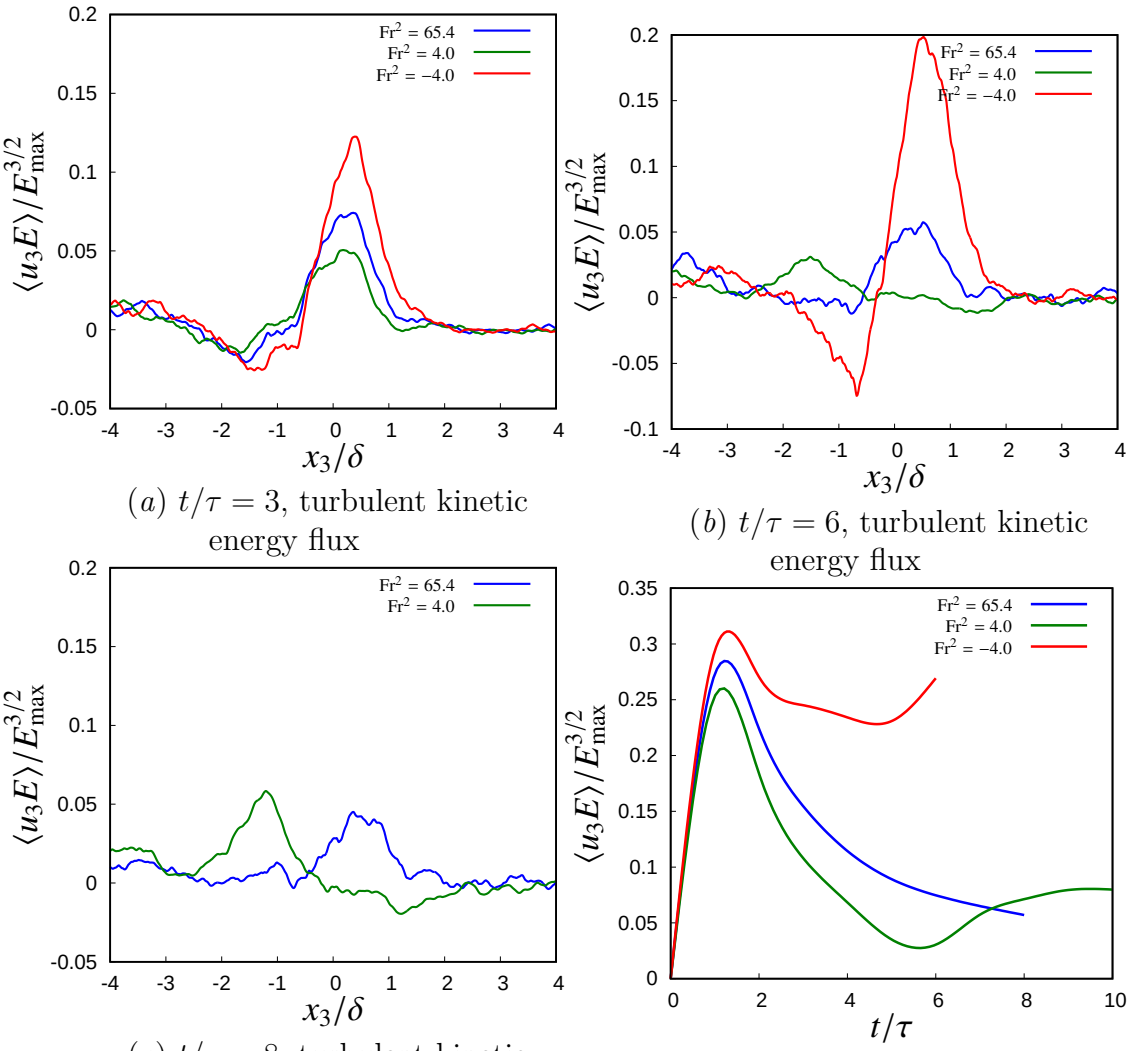

(a) $t/\tau = 3$, turbulent kinetic energy flux

(b) $t/\tau = 6$, turbulent kinetic energy flux

(c) $t/\tau = 8$, turbulent kinetic energy flux

(d) Maximum of flux over time

Figure 4.10: **Panels (*a*–*c*): turbulent kinetic energy fluxes along the vertical direction x_3, averages of the horizontal planes $x_1 - x_2$, after 4, 6 and 8 time scales, respectively. It should be noted that, for the unstable simulations, it is not possible to reach 8 time scales for the computational stability problems self-generated by the physical condition of the flow. Data from simulations considering different initial squared Froude's numbers normalized on the mean turbulent kinetic energy of the high energy vapor cloudy region. Panel *d* shows the temporal trend of the maximum normalized turbulent kinetic energy flux.**

It can be observed as a dynamic feature that goes along with the formation of the turbulent kinetic energy pit and the obstruction of the growth of the mixing layer. To complete this section, we report a comparison between the active and passive scalars studied here in Fig. 4.11, for the same distributions shown in Fig. 4.9.

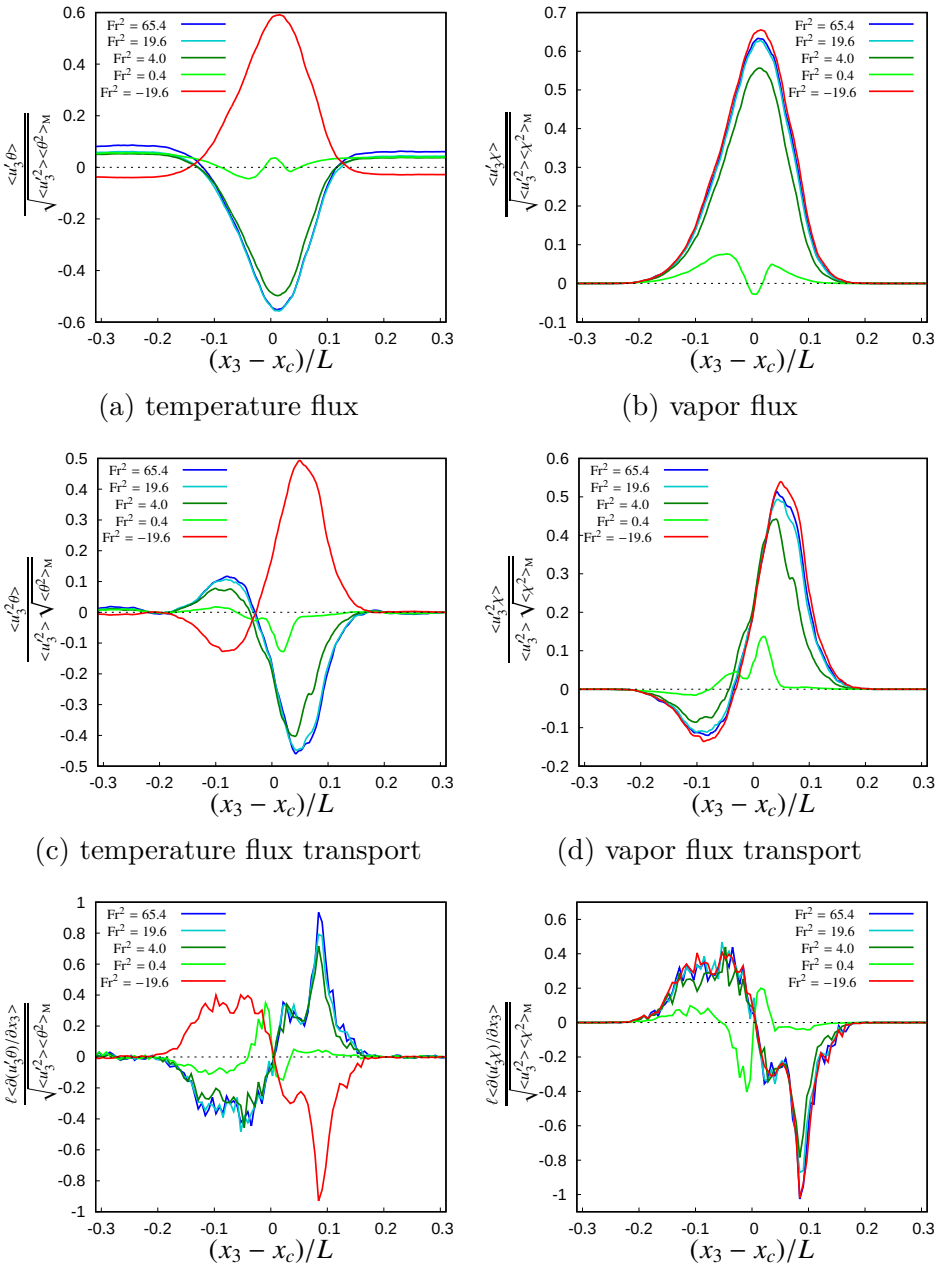

(a) temperature flux

(b) vapor flux

(c) temperature flux transport

(d) vapor flux transport

(e) temperature flux derivative across the interface

(f) vapor flux derivative across the interface

Figure 4.11: **Comparison across the interface of the normalized plane averages of the heat (active scalar) and vapor (passive scalar) flux profiles (panels *a* - *b*), of their fluxes of $u_3'^2\theta$ and $u_3'^2\chi$ (panels *c* - *d*), and of their vertical derivatives (panels *e* - *f*) for different levels of stratification at $t/\tau = 3$.**

4.5 Formation of the energy pit/peak sublayers and stratified shearless turbulent mixing

The onset of a sublayer can be seen after the transient, when buoyancy in the domain's center, where the initial temperature gradient is located, begins to become non-negligible.

A similar sublayer's formation and temporal evolution are depicted in Fig. 4.12, along with the normalized kinetic energy profiles, $E_{\text{norm}} = (\langle E \rangle - E_{\text{min}}) / (E_{\text{max}} - E_{\text{min}})$ and the time variation of the temperature are shown. Here, E_{max} and E_{min} are the maximum and the minimum mean kinetic energies, respectively. Figure 4.12, representing the mixing layer thicknesses. (a) temperature, (b) passive scalar vapor and distribution of the normalized kinetic energy at different time instants for (c) stable and (d) unstable stratification. Finally panel (e) dedicated a time evolution of the pit width with variation of a Froud number.

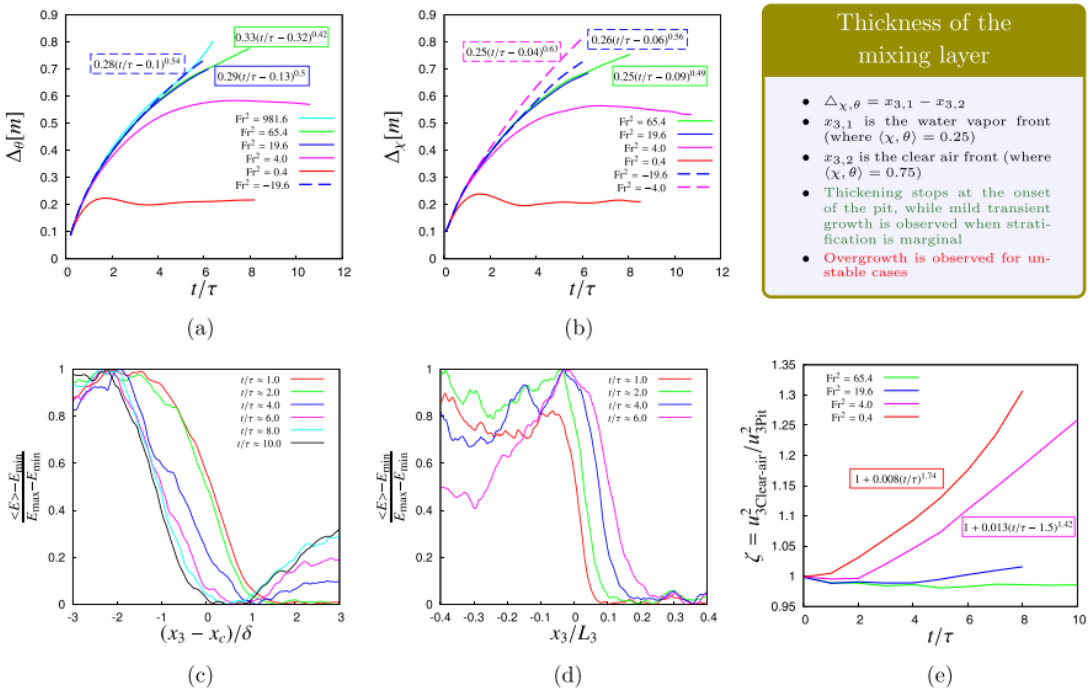

Figure 4.12: **Mixing layer thicknesses. (a) temperature, (b) passive scalar vapor. Distribution of the normalized kinetic energy at different time instants for fr=4.0 (c) and fr=-4.0 (d). E_{min}, E_{max}, minimum and maximum turbulent kinetic energy inside the mixing layer. The clear air top region in panel (c) (right part of the plot) initially shows a value of around 0.Panel (d), in this case, the clear air low energy region always shows a value of around 0. The temporal reduction in the high energy cloudy region highlights the formation of a peak which remains in the very center of the mixing. (e) Time evolution of the pit width with fr. The pit onset starts at around $t/\tau = 2$, and it is clearly visible beyond $t/\tau = 4$, when the layer portion with normalized energy close to 0 is located in the 0 - 1 range of $(x_3 - x_c)/\delta$.**

By looking at the Fig. 4.12, it is obvious that in the low-energy clear-air region, the normalized energy is almost equal to 0, whereas, in the high-energy vapor cloud region, it is almost equal to 1. whereas $E_{\max}$ always remains inside the high-energy region, in steady situations, the pit of energy shifts the location of $E_{\min}$ so that it is now inside the pit. E_{norm} is roughly equal to 1 at the onset of the pit, 0 inside the pit, and > 0 in the low-energy region, as can be seen in panel (c) of Fig. 4.12 for the fr=4.0 case. E_{norm} is 0 in the low-energy region, 1 inside the peak sublayer, and < 1 in the high-energy region in unstable cases after the formation of their peak sublayer, as shown in panel (e) of the same figure.

It is important to examine these "gain" or "loss" variations with the neutral case of fr=65.4.

The following relative turbulent kinetic energy variation can be defined as follows:

$$\mathcal{E} = \frac{E_{\text{mix}} - E_{\text{mix,Fr}^2=65.4}}{E_{\text{mix}} + E_{\text{mix,Fr}^2=65.4}}, \tag{4.9}$$

E_{mix} and $E_{\text{mix,Fr}^2=65.4}$ are the kinetic energies within in the mixing layer, respectively. By integrating over thickness Δ_χ, which is conveniently determined on the passive scalar distribution, this variation is produced.

Indeed, it is challenging to give a clear definition of layer thickness due to the complicated behavior of the turbulent kinetic energy profiles. The Δ_χ is defined by:

$$\delta_\chi(t) = x_{\text{top}}(t) - x_{\text{bot}}(t) \tag{4.10}$$

where the vertical coordinates x_{top} and x_{bot} correspond to the mean scalar concentrations of 0.25 and 0.75, respectively,

$$\langle\chi\rangle(x_{\text{top}}, t) = 0.25 \qquad \langle\chi\rangle(x_{\text{bot}}, t) = 0.75,$$

See Fig. 4.12(b).

The thicknesses of the algebraic growth of the passive scalar and the kinetic energy share a common exponent in the absence of any stratification, as shown in Fig. 6 in [109] and also [147] and [148].

Fig. 4.13 depicts the evolution of $\mathcal{E}$ over time. The exponents grow as the stratification increases -1.84 for fr=-19.6 and -2.14 for fr=-4.0.and the relative energy variation in the presence of unstable stratification increases in time with an algebraic trend. In stable cases, the issue is more complicated. It is possible to see an initial transition phase where $\mathcal{E}$ is almost constant. After that, there is an algebraic decrease with exponents less than 1.

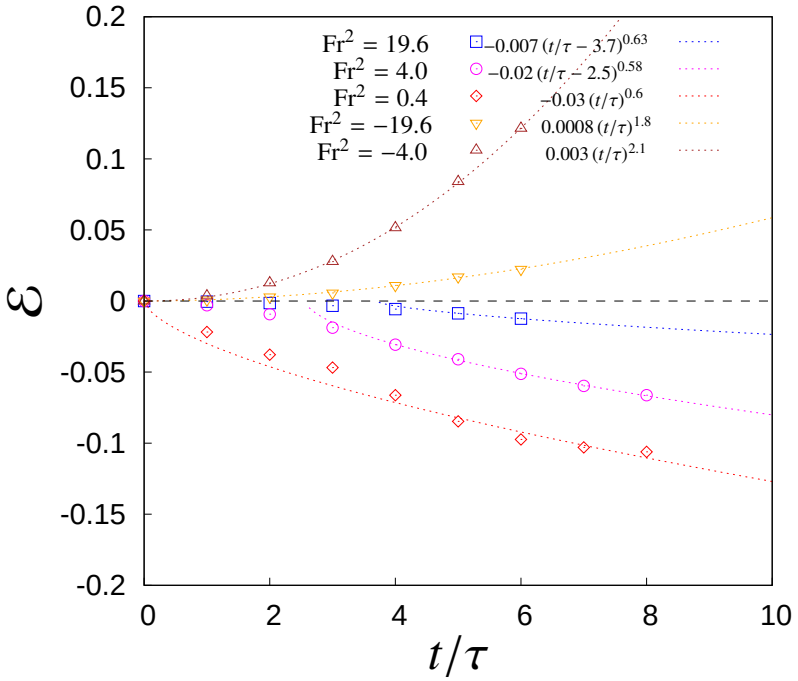

Figure 4.13: **Time evolution of the relative turbulent energy variation $\mathcal{E}$, which is defined as the difference in the turbulent kinetic energy inside the mixing layer from the neutral case fr=65.4. $\mathcal{E}$ follows an algebraic trend. In stable cases, after an initial transition that can last four eddy turnover times, a decay of the relative energy is observed inside the mixing, with lower exponents than 1. In unstable cases, the exponents are greater than 1 and the initial transition is absent.**

It should be noted that in the case of a very strong stable stratification, the initial transition is not evident. The pit sublayer is defined as the region where the mean turbulent kinetic energy is less than 80 percent of the mean energy inside the low-energy clear region (averaged in the $x_1 - x_2$ planes). Fig. 4.12(d) depicts the energy pit sublayer's intensity variation over time. The pit width increases essentially linearly over time after the initial transition. This is qualitatively consistent, at least, with the stratified Rayleigh-Taylor instability simulation's finding of the hull length growth by 36 and the temporal evolution of the downdraught penetration length in buoyancy reversal in cloud tops [123].

Fig. 4.12 show that the mixing layer's thickness is still increasing as the pit forms. The growth doesn't end until several timescales after the pit begins; after that, there are brief oscillations toward an asymptotic value. Stable stratifications exhibit different behavior. In these situations, the production of the energy peak improves mixing by causing the layer to thicken more quickly and with higher exponents—0.63 for Fr2=4.0 and 0.54-0.56 for Fr2=19.6 —than in the neutral situation, where the exponent is 0.42–0.49.

4.6 Transport and Entrainment in Mixing Layer

An important inertial component of interface dynamics is the entrainment of external fluid inside mixing layers. This entrainment can occur at shear-free interfaces, such as those found in clouds and planet atmospheres, or at more typical turbulent-nonturbulent interfaces like boundary layers, jets, and wakes. In the lack of a mean velocity, only downward velocity variations can move clear air into a vapor cloud in any plane parallel to the interface.

A marker function, w, that is equal to 1 when u_3 is negative and 0 otherwise, can be used to highlight their presence. Outside of the mixing region, the entrainment means the value is roughly constant and equal to 0.5 ± 0.01 a value that would be seen for homogeneous and isotropic turbulence. The deviation, however, is bigger (up to $\sim \pm 0.05$) within the mixing layer, with a spatial distribution and temporal evolution that resembles those observed in the third-order instant of velocity, as shown in Figure 4.6.

The vertical derivative of the descending vapor flux at $\mathrm{Fr} = 2.05$ is demonstrated in Figure Figure 4.14(a). Within the vapor cloud, the downward flux rapidly goes to zero, indicating that the entrainment of clear air is limited to a thin interfacial layer as the flow evolves and its derivative, which indicates the net variation of $1-\chi$ at a given instant.

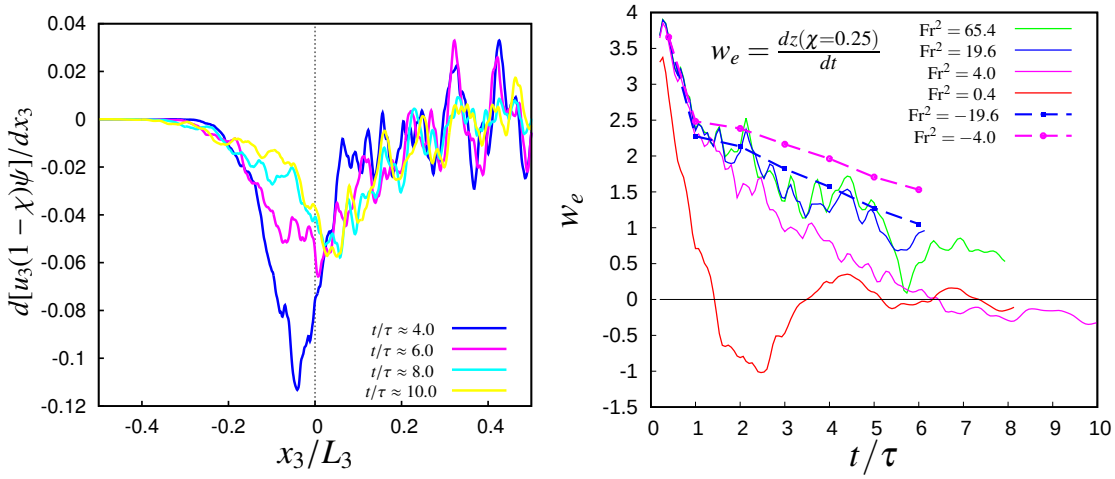

(*a*) $t/\tau = 4$, vapor flux at $fr = 4.0$ (*b*) Entrainment velocity

Figure 4.14: **Panel (*a*): vertical variation of the mean flux of the vapor in the cloud; the marker function ψ only takes into account the spatial points where the velocity is directed downward. Panel (*b*): time evolution of the mean entrainment velocity fluctuation, w_e, which is normalized with the high turbulent kinetic energy E_1 root mean square. w_e is calculated in the horizontal plane where $\chi = 0.25$. Both stable interfaces (solid lines) and unstable interfaces (dotted lines) are represented here.**

Since the expansion of a cloud is caused by the entrainment of clear air, it may be identified and consequently quantified by considering the speed at which the cloud spreads. The place where the mean vapor concentration X is equal to 25 percentage χ is known as the velocity $w_e = dz/dt$, where $z = \langle x_{3,i} \rangle$ is the mean vertical position of the cloud top interface. the time-variation of z has frequently been employed as a parameter to calculate the entrainment rate (see [35] and [121]).

The time evolution of w_e for various stratification levels of perturbation is shown in Figure 4.14 (b). We gradually decline with an algebraic trend in the presence of a quasi-neutral stratification, which is connected to the natural decay of the turbulent kinetic energy. However, when a stable, strong stratification is present w_e is significantly faster and the entrainment disappears after a few time scales. The presence of the turbulent kinetic energy pit reduces the transport efficiency, it should be emphasized that such entrainment is corresponding to the mixing thickness (see Fig. 4.12). However, in the case of unstable stratification, the presence of a turbulent kinetic energy peak promotes mixing, which slows the degradation of the entrainment speed.

looking at the turbulent kinetic energy flux in Figure 4.10, and the passive scalar flux in Fig. 4.11, it is also possible to understand how a varied level of entrainment is related to various transport efficiencies of any physical quantity.

The presence of stable or unstable stratification results in an initial reduction or increase in the energy flux, respectively, with the maximum flux, always occurring around $x_3/\delta = 1$, see Fig. 4.10. In a steady stratification, the flux falls until it reaches a very low value. According to the experimental findings, two fluxes can then be seen to form [84].

4.12(c) and Figure 4.10(c) show the first, which is below the pit at $x_3/\delta = -1$, is positive (upward flux), and the second, which is above the pit between $x_3/\delta = 1$ 3, is negative (downward flow). For the stable case with Fr2=4:0, a minimum value of 0.025 can be observed in the time evolution of the integral value of the flux in the layer 4.12, panel (d).

For Fr2=4.0, the ratio between the two fluxes is approximately 0.25. Since there is no mean flux in between these two fluxes, energy tends to build up at the pit edge rather than cross it, limiting the mixing thickness to a set width. In particular, panel (a) in JW's Fig. 17 and the temporal sequence of panels (a) -(c) in our Fig. 4.10 both exhibit an inversion and reduction of the turbulent kinetic energy flow in the presence of significant stable stratification. A significant agreement can be seen between the trend of our flow for Fr2=65.4 and 4.0 at the end of the transient and the derivative of the energy flow along the vertical in panels (b) and (c) of Fig. 17 in JW. Although the maximum flux at $x_3/\delta = 1$ continues to increase in the case of unstable stratification, a secondary negative flux that is placed close to $x_3/\delta = -1$ is beginning to form. In this state, the energy is transferred from the peak sublayer to the region of the external homogeneous vapor cloud, which encourages the mixing layer to thicken.

The passive scalar flux, in the top panel on the right of Fig. 4.11, exhibits similar behavior.

In comparison to the scalar variance, the unstable stratification increases the flux, which becomes increasingly important. The flux is consistently focused on the top region, therefore there are no obvious changes in the spatial trend. However, there are significant variations in the case of stable stratification: after an initial dampening, the flux becomes zero or even negative in the mixing layer's center (see Fr2=0.4 in the aforementioned panel), which is consistent with the experimental findings of Ref. [84]. The bottom panel on the right, shows the flux derivative and the vertical direction [25].

A positive derivative (the passive scalar moves away) can be seen as the entrainment of clear air, whereas a negative derivative (the passive scalar moves toward) implies the detrainment of clear air (the passive scalar moves into the layer). When stratification is neutral (and unstable), mixing drives the scalar upward, where it was not previously existent. In a stable stratification, we see two sublayers (dark yellow solid line, Fr2= 0.4) surrounding one sublayer with a negative derivative, retaining the scalar within the mixing layer. Looking at an instantaneous three-dimensional visualization of the flow streamlines, as shown in Fig. 4.15, where three stratification cases are represented as neutral Fr2=65.4, stable Fr2=4.0, and

unstable Fr2=- 4.0, one can also see a reduction in communication between the two regions outside the mixing layer.

The streamlines are calculated for fluid particles that are originally positioned $2\delta_0$ above (red) and below (blue) the mixing layer's center, and they are displayed after 6 initial eddy-turnover times. It is evident that streamlines from the upper side can traverse the interface in the neutral situation, panel (b), to reach the bottom region, and vice versa. When stable stratification is present, as shown in panel (a), this does not occur; in this scenario, the crossing of the interface becomes continuing rare, and nearly all the particles placed on one side of the interface remain there. The streamlines more frequently cross the layer when there is unstable stratification, as seen in panel (c), where mixing is enhanced.

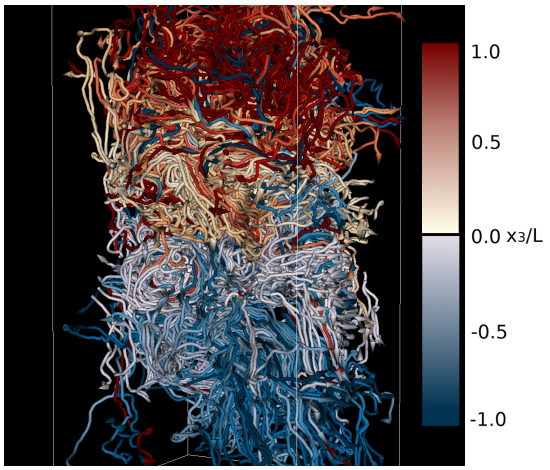

(*a*) fr=4.0

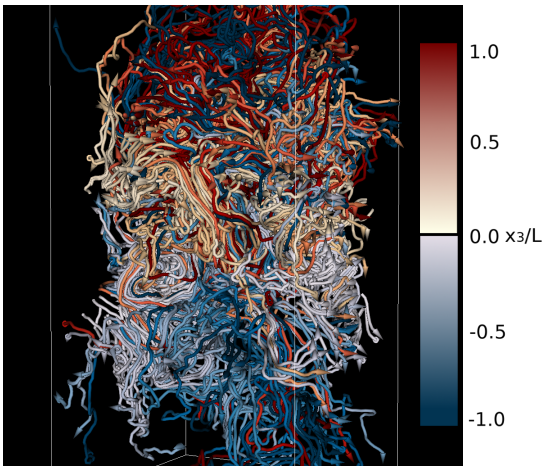

(*b*) fr=-65.4

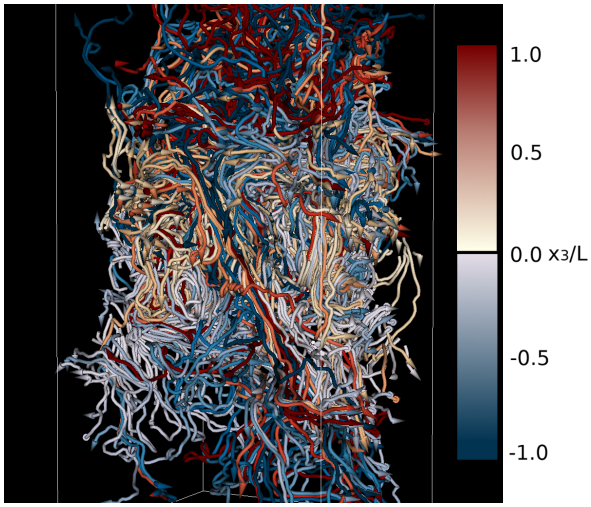

(*c*) fr= - 4.0

Figure 4.15: **Streamlines after 6 time scales for different stratification levels – (*a*) fr=4.0 highly stable, (*b*) fr=65.4 negligible stratification, (*c*) fr=-4.0 highly unstable. The starting position of each streamline is placed at a fixed distance from above (yellow/red tubes) and below (cyan/blue tubes) the center of the interface. In panel (*b*), where the buoyancy forces are negligible, streamlines from the upper side can cross the interface to reach the lower region, and viceversa. Instead, in panel (*a*), where stable stratification effects are relevant, crossing of the interface becomes increasingly rare: what is located on one side of the interface tends to stay there, and the mixing process is damped. Finally, in the case of unstable stratification shown in panel (*c*), the mixture of red and blue lines is enhanced, which means that the streamlines cross the interface more frequently.**

4.7 Anisotropy in the shear-less mixing layer

In the present system, the anisotropy is firstly set by the initial velocity fluctuation condition, which introduces a gradient of turbulent kinetic energy, which in turn, induces the flux of momentum and turbulent kinetic energy. Secondly, the temporal evolution of the vertical velocity component feels the effect of the buoyancy stable/unstable forces, which damp/enhance the transport. By considering the relative weight of the energy associated with the vertical velocity fluctuation, with respect to the other components (Pope(2000)), the large-scale anisotropy is represented by the ratio:

$$B_3 = \frac{\langle u_3 u_3 \rangle}{\langle u_k u_k \rangle} - \frac{1}{3} \tag{4.11}$$

Figure 4.16 depicts the B_3 ratio's behavior in the vertical direction (panel a) as well as the progression of its peak value over time. Anisotropy is present on a large scale for a neutral stratification condition but is limited, with a maximum deviation of 5 %. Anisotropy becomes very intense in the presence of stratification. In particular, it is feasible to see that the vertical fluctuation experiences a significant depletion under stable stratification conditions. ($\langle u_3^2 \rangle < \langle u_{1,2}^2 \rangle$) And, vice versa, an intense growth under unstable conditions ($\langle u_3^2 \rangle > \langle u_{1,2}^2 \rangle$).

Additionally, Fig. 4.16*a* shows that the variation affects the global mixing layer in addition to the previously discussed pit/peak turbulent kinetic energy sub-layers. In fact, a concurrent shift in the primary energy gradient is observed together with the creation of such sub-layers. This fact supports the finding that, along with the significant effects directly caused on the drop size distribution and supersaturation fluctuation by the small scale [119], the time evolution of a cloud during mixing is somewhat sensitive to large scales [105].

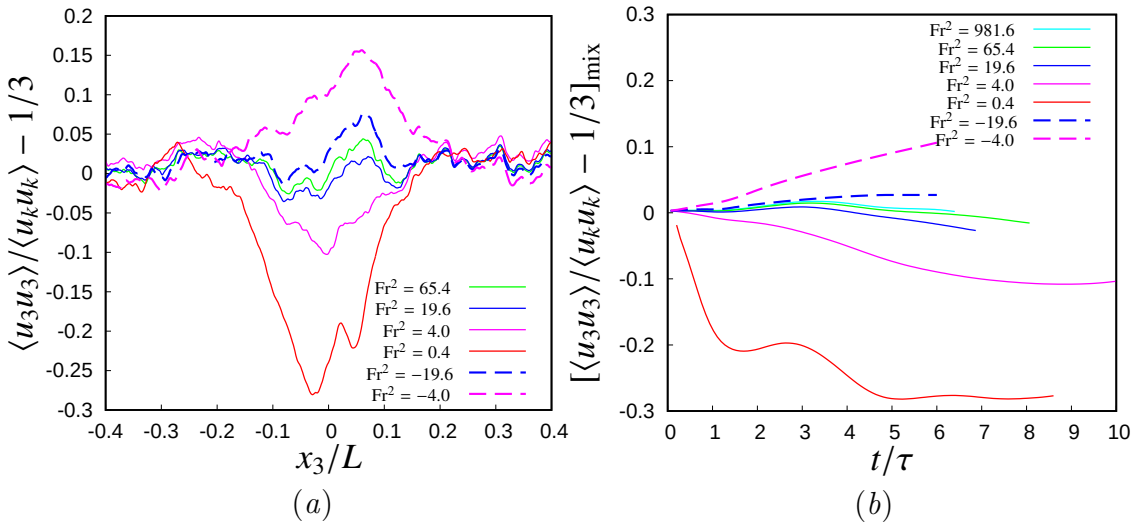

Figure 4.16: **Anisotropy of the turbulence large scales. (*a*) B_3 ratio along the vertical direction obtained by varying the fr number. (*b*) Temporal evolution of the B_3 peak value.**

It should be noticed that the first-order longitudinal derivative of the velocity components' higher moments accurately captures the flow's small-scale anisotropy [138].

4.8 Conclusion

By linking two homogeneous, isotropic turbulent fields with various kinetic energies, it is possible to simulate the evolution of a freely degrading, shearless, turbulent mixing layer that contains both air and a vapor phase and is referred to as a passive scalar phase. The effects of both stable and unstable temperature circumstances on the mixing dynamics have been evaluated using a wide range of Froude numbers.

Our numerical simulations have demonstrated that a shear-free turbulent layer's dynamics and transport characteristics are affected by both stable and unstable stratifications. The first thing that is seen is the formation of a sublayer within the mixing region: (i) the formation of a turbulent kinetic energy pit under stable conditions, which is a type of intense decay overshoot with a lower level of energy than the external regions; and (ii) the formation of a turbulent kinetic energy peak under unstable stratification conditions, where the turbulent energy becomes higher than in the external regions (15 percentages larger at Fr2 14 4:0). Energy variation inside the mixing region's temporal scaling law has been quantified. The exponent is influenced by the intensity of stratification. At Fr2=4.0, it achieves a value of 2.1, which is nearly four times more than the exponent as computed at that point.

Since any variations inside it are slowed by buoyancy forces, stable stratification almost completely inhibits vertical motion.

Large-scale structures are shown to have more anisotropy in this situation than in the neutral scenario. Indeed, the energy related to vertical fluctuations moderately decreases in comparison to the other elements. On the other hand, in contrast to the horizontal components, vertical variations amplify in unstable settings.

In the presence of stable stratification, turbulence diffusion, intermittency, turbulent kinetic energy, passive scalar transport, and clear-air entrainment all get dampened. When the Froude square number drops below 1, entrainment nearly completely disappears. At Fr2=0.4, there is a detrainment phase that lasts between 1.4 and 3.5 eddy-turnover times. Again, unstable stratification improves mixing.

When the perturbation is stable, the dissipation function significantly increases. Here, a 70 % increase at Fr2= 4.0 has been noted. On the other hand, a 2 % reduction has been noted at Fr2=4.0. The dissipation rate's log-normal probability density functions have been found to be self-similar inside different layers across the mixing. This conclusion can be understood by keeping in mind that stratification affects the energy related to the vortical structures more than their form.

In terms of small-scale anisotropy, it has been discovered that the presence of unstable stratification makes the statistical disparities between the longitudinal velocity derivatives more pronounced. As a result of the enhanced mixing intensity, the compression of the fluid filaments normal to the interface is larger. Small-scale anisotropy also tends to disappear in stable conditions because the mixing process tends to disappear.

The primary finding of spectral information relates to the velocity fields. We have observed a significant divergence in time for both low and high wave numbers for the vertical velocity fluctuations, comparing the stratified spectral behavior with the unstratified behavior of the velocity fields. Instead, differentiation can be clearly visible for the horizontal components of the velocity variation at the smallest scales, or for the largest wave numbers.

In the future, we would like to run simulation campaigns on domains that are comparable in size to those considered in this work, but that also include the aqueous liquid phase and the associated collision and coalescence phenomena of water droplets, as has recently been done, though at a much smaller domain scale than that which is considered here [105] and [95]. Specifically, rather than the few seconds of the current simulation, we would prefer to consider a longer time window, or a time of almost one minute of a three-phase (gas, vapor, and liquid) warm cloud.

It should be kept in mind; however, the structure of the clean air-cloud interface is further complicated by droplet clustering. It is impossible to predict this from the outset because of the discontinuous distribution of droplets and droplet clusters in space, which implies that various cores will have to put in very uneven computing workloads at different times. It would be quite challenging to push the code to

a massively high level of parallelization, where physical modeling is still being developed. The time required to transfer data between the cores really increases by around eight times when going from slab to pencil parallelization (which has already been accomplished for the version of the code used in this work, which does not imitate water droplets).

This happens because the quantity of data that two neighboring cores communicate is not uniform within the computational area, and additionally, the nonadjacent cores will also need to exchange data. Because turbulence hosts long-term phenomena that can cause large droplet displacements, that is, droplet displacements to a domain portion in a core not adjacent to the core where the droplet departed from, such a situation has a high probability of occurring over short time intervals, such as those that are comparable with a single computational time step.

Chapter 5

Temporal Scales in the Multiphase Microphysics of Warm Clouds

5.1 Introduction

In the following chapter, the role of temporal scales like evaporation, phase relaxation, and reaction times have been studied through a particle-resolved three-dimensional pseudospectral direct numerical simulation model. The mentioned temporal scales have been implemented to parameterize the impact of turbulent mixing on cloud evolution. The evolution of the interfaces (cloud and clear air) where the cloud has been selected on the top portion of the cubes has been modeled as an initial value problem for decaying turbulence.

In this survey, solution and curvature effects, droplet collisions, temperature stratification, and vertical stability have been looked over in detail. The dynamic of droplets and time scale statistics are computed by averaging over the planes parallel to the interface x_3 direction.

The evolution of the supersaturation balance is discussed for the size distribution of initially monodispersed and polydispersed droplets.

In this chapter, I tried to provide a brief introduction to the essential aspects of cloud dynamics and microphysics. The ideas presented in the following pages are the key to setting up a numerical model for the analysis I applied to this study. Of course, this thesis does not expect to be exhaustive and shall focus on a particular aspect of the roles that the temporal scales of microphysical and turbulent processes may have on cloud evolution. More complete discussions of the ideas that are expressed and accepted here can be found in the literature [134], [92], [156], [40].

5.2 The effect of turbulent transports on supersaturation balance

In fact, the distribution of the condensed liquid water content is a significant feature that plays a role in the formation of the cloud and its evolution in the atmosphere. The generation of the clouds and disappearing highly relies on the amount of surrounding water vapor and temperature fields. In the atmosphere, aerosols behave as Cloud Condensation Nuclei (CCN) and start to grow via heterogeneous nucleation when they are located in a supersaturated environment (Rogers and Yau, 1996) [92].

The linear relationship between the rate of condensations growth for the small drops and the local level of supersaturation can be estimated according to [24]:

$$R_i \frac{dR_i}{dt} = K_s \left(S - \frac{A}{R_i} + \frac{Br_d^3}{R_i^3} \right) \tag{5.1}$$

$$S\left((\boldsymbol{X})_i, t\right) = \frac{q_v((\boldsymbol{X})_i, t)}{q_{vs}(T)} - 1 = RH - 1 \tag{5.2}$$

Where RH, represents the relative humidity.

Therefore, based on the selected model for the growth of droplets, it mainly depends on the local value of S and the droplet radius R. Figure 5.1 presents the drop growth rate for three values of supersaturation that are selected as constant values. The value $S = 0.02$ is assumed to be in the cloud region of this study and supersaturated, and the value $S = 0$ for saturated and $S = -0.3$ for subsaturated conditions. It is better to mention here the effect of both surface tension (kelvin) and curvature (Raoult) are negligible for the droplets smaller than 1 μm.

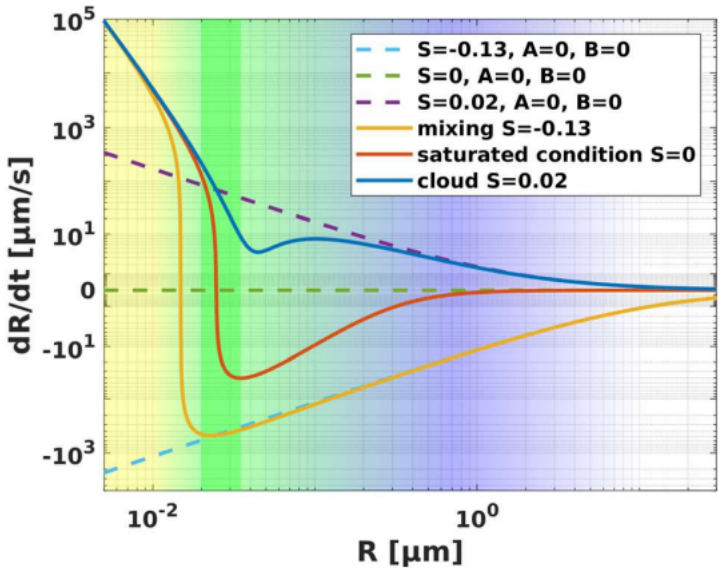

Figure 5.1: **The condensation growth rate for a drop of given radius in different conditions: supersaturated, saturated, and sub-saturated.**

5.3 Evolution of supersaturation fluctuation

In this section, I analyzed the supersaturation balance equation with the aim of considering the effect of supersaturation fluctuations on small-scale intermittency of the carrier flow. Since the evolution of supersaturation fluctuation mainly hosts the vapor and liquid water phases and has been used to model a water vapor budget on a formation of clouds, the general equation has been applied here as below 5.3:

$$\frac{dS}{dt} = \mathcal{P} + \mathcal{C} \tag{5.3}$$

Where the time derivative of supersaturation is determined by balancing a production term, $\mathcal{P}$, and a condensation term, $\mathcal{C}$ [125], [146]

The condensation term usually consider the depletion of water vapor and the release of latent heat during condensation at the surface of a spherical droplet, and it is a function of the local level of supersaturation defines as below:

$$\mathcal{C} = -\frac{S}{\tau_{phase}} = 4\pi\kappa_v N\overline{R}S. \tag{5.4}$$

The source term, $\mathcal{P}$, is frequently represented in models as a linear function of the updraft's vertical mean velocity [4, 66], or as the net flux of supersaturated water vapor via parcel boundaries. [124].

In the present analysis, the presence of updraft is negligible; thus, $\mathcal{P} = 0$ and the Equation (5.3) does not account for the advection and diffusion of water vapor and internal energy in the environment surrounding the droplet ($\mathrm{Re}_{drop} \ll 1$). so considers supersaturation S as a rather global, bulk property of an adiabatic cloud parcel [139].

Generally speaking, in a homogeneous isotropic cloudy layer that is statistically in equilibrium, a zero-mean vertical velocity field would imply a null net vertical transport of cooling vapor parcels. It should be noted that whenever an updraft can be neglected, equation (5.3) can be solved by separating the variables [158]

$$\frac{dS}{dt} \cong -4\pi\kappa_v N\overline{R}S = -\frac{S}{\tau_{phase}} \tag{5.5}$$

Therefore, an initially subsaturated (supersaturated), droplet-laden environment experiences an increase (decrease) in the vapor concentration, which results in S relaxing exponentially to 0. The time constant of this solution is the phase relaxation time which is defined as below:

$$\tau_{phase} = \left(4\pi\kappa_v N\overline{R}\right)^{-1} \tag{5.6}$$

The definition of τ_{phase} depends on the assumption of the droplet population having a constant integral radius, $N\overline{R}$, and it is able to describe the temporal variation of the supersaturation and the liquid water content [89, 34] in a homogeneous context.

The phase relaxation time was chosen from the microphysical time scales used in several DNS studies that focused on entrainment-mixing processes such as [18, 19, 86, 119, 21], and was used to define the Damköhler number

$$\mathrm{Da} = \frac{\tau_{turb}}{\tau_{microphysics}} \tag{5.7}$$

Depending on whether the choice of τ_{turb} falls into large or small-eddy time scales, a vast range of Damköhler numbers can be defined for the same microphysical time scale in a turbulent flow [18]. Large and small values of Da are associated with a fast and slow microphysical response of the droplet population to entrainment and turbulent mixing, respectively [104]. Large Da are also associated with inhomogeneous mixing, whereas small Da often indicate homogeneous mixing [76, 13]. However, it should be noted that in a highly anisotropic, in-homogeneous situation, such as inside the mixing layer that separates the cloud from the subsaturated environmental air, the momentum, internal and turbulent kinetic energy fluxes, and the water vapor are not zero. The fluxes are positive and rising, forming

a peak value that is almost centered in the middle of the layer. Beyond this point, the fluxes decrease and become zero inside the isotropic homogeneous subsaturated ambient air, [147], [44], [97].

In such a situation, a mismatch between the supersaturation time derivative and the condensation term can be expected.

On the other hand, if the focus is on the evolution of the droplet size and the number concentration, the evaporation time scale offers a good practical description of the process and should be taken as the relevant microphysical time scale, $\tau_{microphysics}$.

By neglecting the Kelvin and Raoult terms in equation (2.8), and integrating for a constant $S_0 < 0$, one can obtain in each computational cell, an estimate of the time required for a single droplet, with an initial radius of R_0, to evaporate completely in a uniform subsaturated environment.

$$\tau_{evap} = -\frac{R_0^2}{2K_s S_0} \tag{5.8}$$

Both τ_{phase} and τ_{evap} rely on the assumption of constant supersaturation and integral radius. However, since both quantities vary concurrently inside a mixing layer, it is better to define a reaction time τ_{react} [89] that considers variations of both S and $N\overline{R}$. The reaction time is defined as the shortest time that has elapsed since either the droplet has evaporated completely or the parcel has become saturated, and it is obtained by numerically solving the coupled system of differential equations, that is, Equations condensational growth and (5.5), for initial non-zero values of positive R_0 and negative S_0.

It should be noted that τ_{evap} and τ_{react} are only defined for the subsaturated regions, whereas τ_{phase} is defined for non-zero values of the integral radius, and can also be used in supersaturated regions. In order to describe a characteristic time of the condensation process in supersaturated regions of the domain, we introduce a condensation time τ_{cond}, which we arbitrarly define as the time it takes a droplet to double its radius for a constant local supersaturation S:

$$\tau_{cond} = \frac{3}{2}\frac{R_0^2}{K_s S_0}. \tag{5.9}$$

The horizontal planar average values of all these microphysical time scales are plotted for two different time instants and the initial droplet size distribution type in the cloud and mixing regions. See Figure 5.2, where the computation is performed in each computational grid cell and then averaged over the horizontal planes.

Microphysical time scales and mean supersaturation in the cloud and interfacial mixing regions

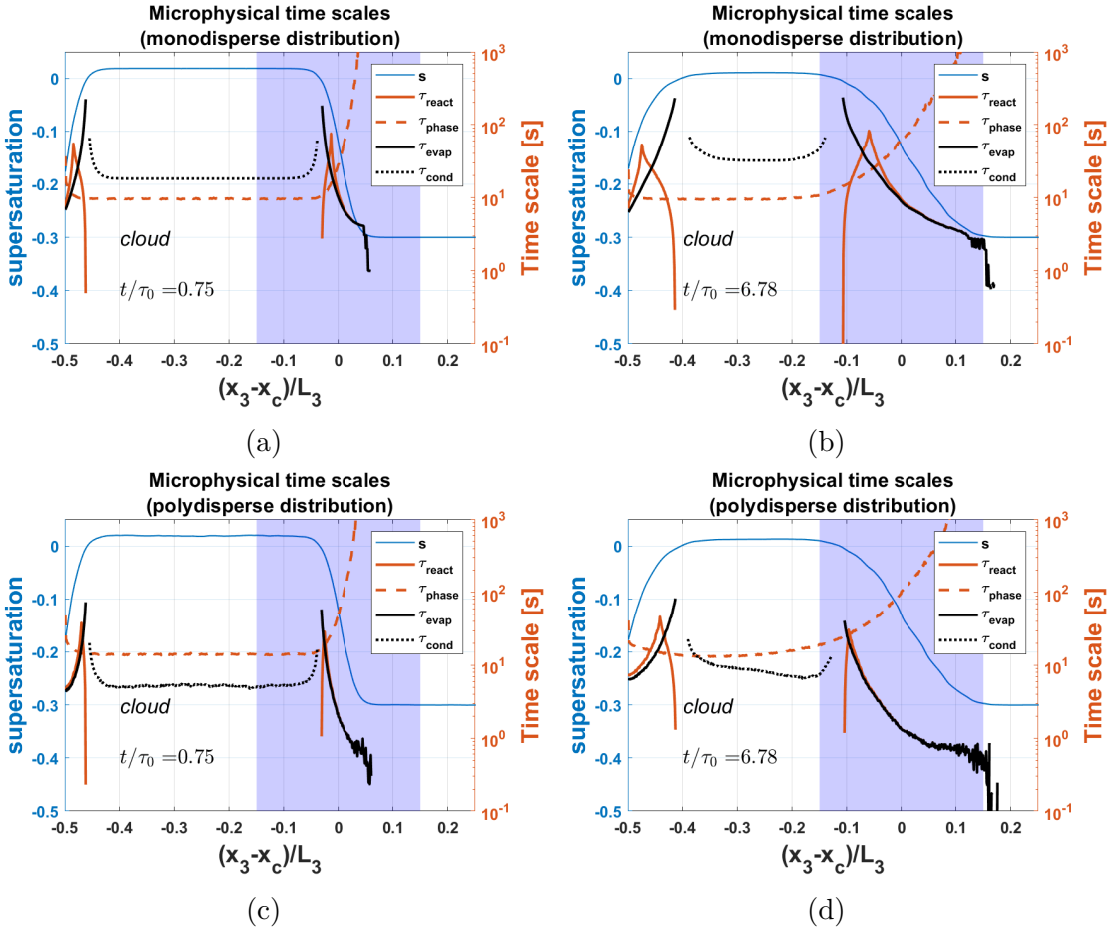

Figure 5.2: **Vertical distribution of the evaporation τ_{evap}, phase relaxation τ_{phase} and reaction τ_{react} time scales computed inside each grid cell and then averaged on horinzontal planes. The data are displayed for the monodisperse and the polydisperse cases.**

The condensation and evaporation times diverge toward values of the order of 10^3 seconds at the saturation location, S = 0. As the mean radius and droplet concentration (numerical density) decrease, the phase relaxation time, τ_{phase}, extend. In the polydisperse scenario, the condensation time is lower than that in the cloudy region, but it becomes of the same order as the τ_{phase} when the mixing process begins.

The phase relaxation, reaction time, and evaporation time cluster together in one area inside the mixing layer, which is the most intriguing finding. Clustering of the microphysical times occurs at nearly the same region where the flux rate

is close to a maximum (Fig. 5.3). Since condensation frequently happens quickly in the spectral range of drops with a small radius, the clustering also includes the condensation time.

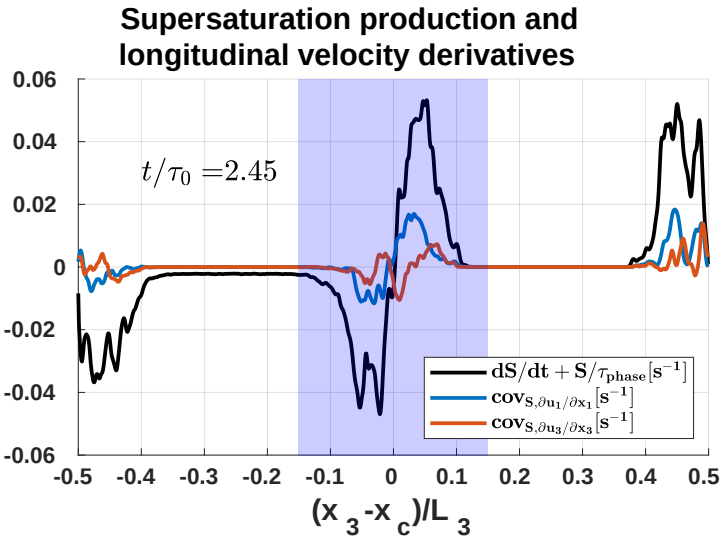

Figure 5.3: **Distribution of the planar horizontal averages along the vertical direction of the difference between the time derivatives of the supersaturation and condensation terms, $\overline{dS/dt} - \overline{C} = \overline{dS/dt} + \overline{S/\tau_p}$ and of the covariances $cov_{S,\partial u_1/\partial x_1}$, $cov_{S,\partial u_3/\partial x_3}$, see equation (5.10). These quantities vary considerably inside the mixing layer, and the two kinds of curves are both almost antisymmetric with respect to the center of mixing layer x_c. The data were retrieved from a monodisperse simulation at $t/\tau_0 = 2.45$.**

The covariance for each horizontal plane is calculated by:

$$cov_{X,Y}(x_3,t) = \frac{1}{n_1 n_2} \sum_{i,j=1}^{n_1,n_2} \Big(X(x_1,x_2;x_3,t) - \overline{X}\Big)\Big(Y(x_1,x_2;x_3,t) - \overline{Y}\Big) \tag{5.10}$$

where the over-line indicates the average of a given physical quantity in the x_1, x_2 planes and

$$\overline{X}(x_3,t) = \frac{1}{n_1 n_2} \sum_{i=1,j=1}^{n_1,n_2} X(x_1,x_2;x_3,t) \tag{5.11}$$

The Pearson product-moment correlation coefficient of two planar averaged quantities, $\overline{X}(t)$ and $\overline{Y}(t)$, only depends on the time and when used to correlate variations across the interface layer $\Delta(t)$, it can be written as

$$\rho_{X,Y_\Delta}(t) = \sum_{k=1}^{n_\Delta} \frac{(\overline{X}(x_3,t) - \overline{X}_\Delta(t))}{\sigma_{\overline{X}}} \; \frac{(\overline{Y}(x_3,t) - \overline{Y}_\Delta(t))}{\sigma_{\overline{Y}}} \tag{5.12}$$

where subscript Δ stands for the quantity averaged inside the interface and n_Δ is the number of planes inside the interface.

In the polydisperse case, which shows the reaction time on the right-hand side of the panels in Figure 5.2 oscillates to great extent, the clustering of the microphysical times takes place at almost the same location, where the flux rate is close to a maximum

5.4 Turbulent transport effects on the supersaturation balance

The rapid increase in droplet size that is observed in some cumulus cloud formations can be explained, at least in part, by the observed acceleration of the population dynamics in the same cloud-clear air interface region, see [164], [77], [105]. These findings were made despite the fact that the interface also hosts the spatial decay of the turbulence in addition to the temporal decay that is present throughout the system.

The planar averages of the difference between the time derivative of the supersaturation and the condensation terms must be null in case of zero updraft and almost statistical equilibrium (steady state, homogeneity, and isotropy).

$$\overline{dS/dt} - \overline{\mathcal{C}} = \overline{dS/dt} + \overline{S/\tau_p} \cong 0. \tag{5.13}$$

The turbulence supersaturation fluctuation production is the name for this inbalance. The covariances between the supersaturation and the longitudinal velocity derivatives are plotted across the entire $(x_3 - x_c)/L_3 \in [-0.5, 05]$ domain, as can be seen in Fig. 5.3. A temporal decay occurs after an initial transient turbulent kinetic energy gain caused by an unstable stratification. The vertical distribution of the evaporation time, phase relaxation time, and reaction time are shown in Fig.5.2.

Low small-scale Damköhler numbers, and should therefore enhance turbulent numbers are caused by high values of τ_{phase} at the interface, which should increase turbulent supersaturation fluctuations [66]. It is logical to suppose that such fluctuations predominate over those brought on by phase transition at the surface. The statistical moments of a subsaturated cloud region devoid of droplets are similar in form and value to those of mixing that contain droplets from a supersaturated cloudy region (Figure 8 in [97]). The effects of the supersaturation statistics linked to the various size distributions of the drop populations are insignificant, and the differences are actually much below than 1%.

We hypothesize that small-scale turbulent fluctuations influence the magnitude of the local supersaturation and that these turbulent fluctuations may contribute to the overall equilibrium. We searched for the relationship between: i) the difference

in the planar averages of the supersaturation time derivative and the condensation term, and (ii) the covariance, Equ. 5.10, of the supersuperturbation. Thus, we put:

$$\overline{\frac{dS}{dt}} + \overline{\frac{S}{\tau_{phase}}} = \overline{\mathcal{P}_t} \sim \mathrm{cov}_{S,\partial u_i/\partial x_i} \tag{5.14}$$

This is conceptually equivalent to modeling supersaturation production as the product of the supersaturation fluctuations and the characteristic frequency of small-scale turbulent structures, $\sim \tau_\eta^{-1}$, where the characteristic frequency of small-scale turbulent motions can be represented by the longitudinal velocity spatial derivatives. Small-scale anisotropy in turbulent shearless mixing has been investigated numerically. The results of direct numerical simulations for Taylor microscale Reynolds numbers between 45 and 150 [43], [41], [109], [105], [97] show that the longitudinal velocity derivative moments significantly deviate from the values found in homogeneous and isotropic turbulence. Even in a flow where there is no energy generation due to the lack of mean flow gradients, this intermittency is characterized by a significant deviation of the longitudinal derivative moments.

For i = 1,2,3, the Pearson correlation coefficient, $\rho_{\overline{\mathcal{P}_t},\mathrm{cov}_{S,\partial u_i/\partial x_i}}$ inside the layer of thickness $\Delta(t)$, was calculated along the transient. Each data point represents a time interval equal to roughly half of the initial eddy turnover time. The correlation is considered strong when the correlation between two sets of data is above 0.7. Both drop populations with monodisperse and polydisperse particles exhibit this.

$\overline{\mathcal{P}_t}$ and $\mathrm{cov}_{S\partial u_i/\partial x_i}$ should have a nearly linear relationship, $i = 1, 2$, with respect to the mixing layer of $\overline{\mathcal{P}_t}$ and $\mathrm{cov}_{S\partial u_i/\partial x_i}, i$ = 1,2.

The proportionality constant, C, is relevant to the dimensional quantities along the transient:

$$\int_\Delta \left| \frac{d\overline{S}}{dt} + \frac{\overline{S}}{\tau_{phase}} \right| dx_3 \cong C \int_\Delta \left| \mathrm{cov}_{S\partial u_i/\partial x_i} \right| dx_3 \tag{5.15}$$

Figure 5.4 shows the estimated values of the non-dimensional constant C (orange curve).

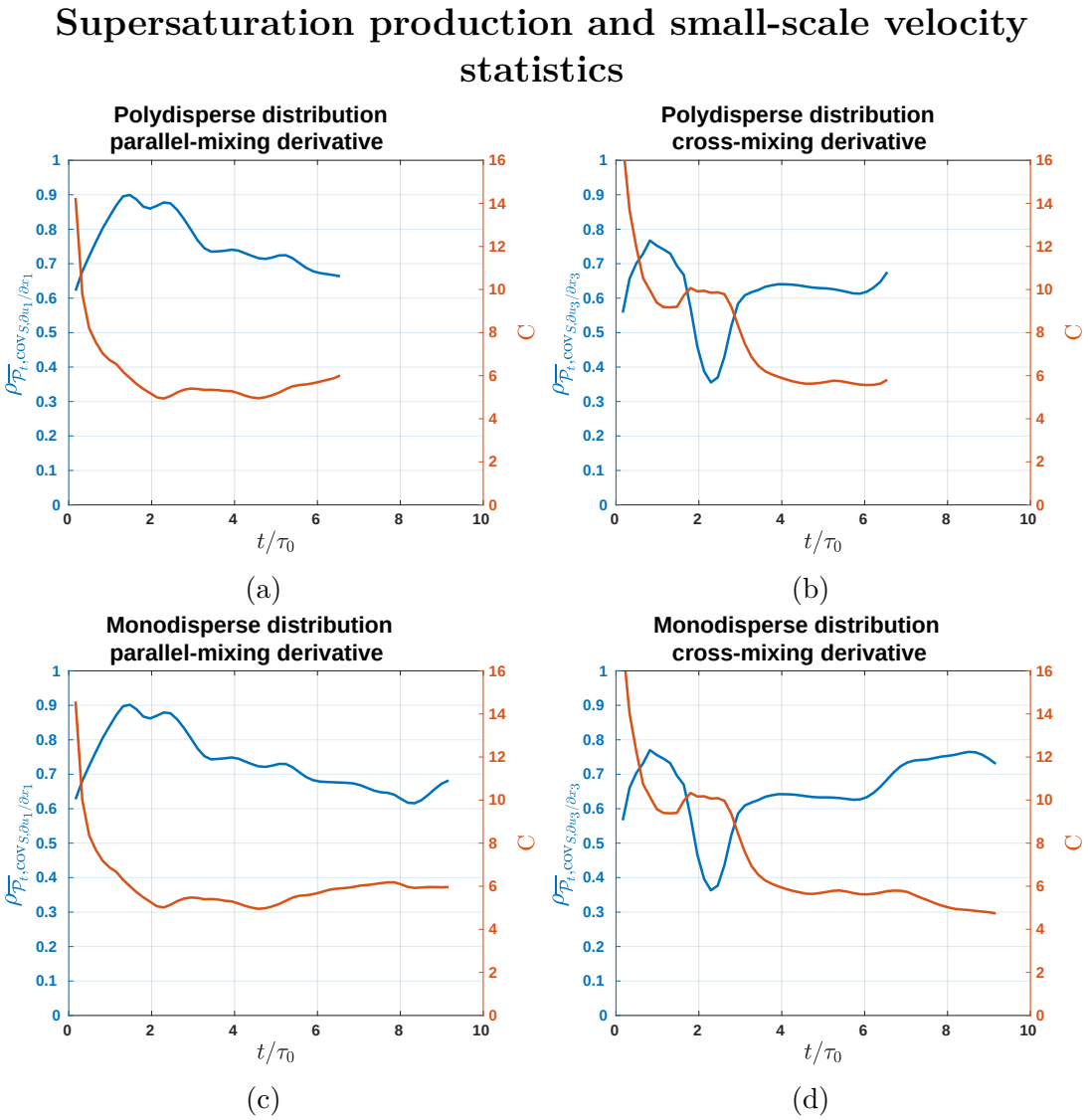

Figure 5.4: **Time evolution of the estimated production-planar covariance correlation coefficient and the proportionality constant. The Pearson correlation coefficient between the turbulence production term $\mathcal{P}_t$, see equation(5.14), and the supersaturation-velocity longitudinal derivative covariance (blue curves) plotted for the horizontal (left, ac) and vertical (right, bd) longitudinal derivatives during the transient. The correlation coefficient peaks around the first initial eddy turnover time and slowly decreases in magnitude to an asymptote ~ 0.7 as the transient progresses.**

As we can observe, C during the transient is not affected by the form of the initial droplet size distribution. Because of the intrinsic small-scale anisotropy of the mixing layer between the cloudy region and the clear-air, we can interpert a different pre-asymptotic pattern for the horizontal and vertical longitudinal derivative correlation coefficients. The estimated value in each of these situations is 5, an asymptotic number that is quickly attained following the first initial eddy turnover.

5.5 Conclusion

In this chapter, I considered the relationship between supersaturation fluctuations and turbulent small-scale dynamics in the context of an **inhomogeneous, anisotropic, shearless**, turbulent air mixing layer that is often used to model the carrier flow at the interface between warm clouds and unsaturated ambient air. Two types of initial droplet populations were tested, namely a monodisperse with a size of 15µm and a polydisperse range $0.06-40$µm with constant-mass-per-volume-class.

The different time scales affecting the microphysics of a droplet population were compared within the upper part of the cloudy region, the layer where the turbulent transport process towards the saturated ambient air takes place. The time scales for evaporation, reaction, and phase relaxation agree at a value of about $20 \sim 30$ s in the layer just before the point where the supersaturation flux reaches its maximum rate of change. In the case of a polydisperse population, this agreement includes condensation time.

The time scales before this spatial location are different, with differences in the order of a minute. Beyond this location, the evaporation and reaction times overlap, while the relaxation phase and condensation time scales diverge asymptotically as the environment becomes more and more undersaturated.

Hypothesizing that the fluctuation in supersaturation depends in large part on the small-scale intermittency of the carrier stream hosting the vapor and liquid water phases, I analyzed the equation of the supersaturation balance to show their mutual correlation. To evaluate this hypothesis, I fitted the estimated planar mean values of the time derivative of the supersaturation and condensation terms with the planar covariance of the supersaturation and the longitudinal velocity derivatives. Indeed, the statistics of the velocity derivatives are particularly relevant to small-scale dynamics. For the specific shearless turbulent structure considered here, the longitudinal velocity derivatives are more significant for small-scale intermittency than the transverse derivatives, which are zero. Moreover, the longitudinal velocity derivative can be considered a characteristic measure of the small-scale frequency. I found a high value of the Pearson correlation coefficient, $\rho_{\overline{\mathcal{P}_t},\mathrm{cov}_{S\partial u_i/\partial x_i}} \sim 0.7$ for the droplet populations both within the boundary layer and over the entire simulation run, leading to the conclusion that in the absence of upwind, the mismatch of the time derivative of the supersaturation and condensation terms is linearly related to

the covariance of the supersaturation and longitudinal velocity derivatives of the carrier current.

Chapter 6

Current developments and perspective research on turbulent dispersion inside warm cloud and surrounding environments

Before starting the current chapter, it is better to mention that the line of research has been addressed and slightly expanded to the experimental part already envisaged and developed in the H2020 COMPLETE project http://www.complete-h2020network.eu, in collaboration with the electronic engineering group coordinated by Prof. Eros Pasero. In other words, the update involved measurements with the innovative mini biodegradable radio probes for exploration in warm clouds developed from scratch inside H2020 COMPLETE. These measurements are still at the preliminary stage of fine-tuning the radiosondes.

The point in common with my previous activity would be the analysis of the turbulent dispersion inside and close to clouds observed in field tests by means of a cluster of radiosondes and, in numerical simulations, by means of the analysis of the Lagrangian trajectories of the water drops transported by the turbulence of the carrier gas flow. However, a direct comparison between the two methods is not yet possible because the most advanced field experiment, carried out in November 2022, consisted of the release into the free air of a small cluster of 10 radiosondes, whose data, sent via radio to two receiving stations, are still in the post-processing stage. And in any case, this number of probes is still too small to obtain relevant statistics. However, it seemed to me appropriate to present this activity as a work in progress and in view of possible new significant results that could be obtained beyond my research work associated with the doctorate.

This chapter aimed to study the water droplet dispersion due to turbulence in warm clouds. Here, we present an in-situ method for determining how small-scale turbulence affects cloud formation. This method is based on the design and use of a novel ultralight (about 20 g), biodegradable, and disposable radiosonde, which we'll refer to as a radioprobe. A radiosonde is a battery-powered equipment with radio transmission capabilities that are often transported into the atmosphere by a weather balloon. The concept came up when developing the proposal for a Horizon 2020 Marie Sklodowska Curie project in Europe, which was accepted in 2016 (H2020 MSCA ITN ETN COMPLETE, GA 675675: Innovative Training Network on Cloud-MicroPhysics-Turbulence-Telemetry http://www.complete-h2020network.eu).

In warm clouds and the surrounding ambient air, the small radioprobes are used to passively detect turbulent changes of air velocity, water vapor, and droplet concentration, temperature, and pressure. The Lagrangian description of turbulent dispersion, put forward by Richardson L. in 1926 [51], is here applied to both radioprobe balloons displacements data recovered during the experiments and to the particle motion in the DNS simulations.

6.1 Tracking the Lagrangian turbulence fluctuations within mini ultralight radioprobes

The small, green, ultralight radiosondes were designed and developed by Parades [129] to measure the influence of small-scale turbulence on cloud formation. Radiosondes are battery-powered instruments carried into the atmosphere, usually by a weather balloon with radio transmission capabilities, and they are designed to be as light as possible, about 20 g. These radiosondes are used to track variations in water droplet position, velocity, pressure, acceleration, humidity, and temperature according to the Lagrangian description of turbulent dispersion originally discussed with the Richardson theory. The radiation probes are inserted into balloons made of biodegradable materials and filled with helium gas. Since the idea is to release the devices into the atmosphere so they can float freely, environmentally friendly materials are used in the design to minimize any potential negative impact on the environment (i.e., green). The example of the radiation probes with a weight of 7 g (without battery) and a size of 50 mm $\times$ 50 mm, and a thickness of 0.8 mm. All electronics are mounted on both sides of a two-layer FR4 substrate with surface mount devices (SMD). See Figure 6.1 For more details on the structure of the electronic components, for more information see Miryam Paredes, 2021 [129].

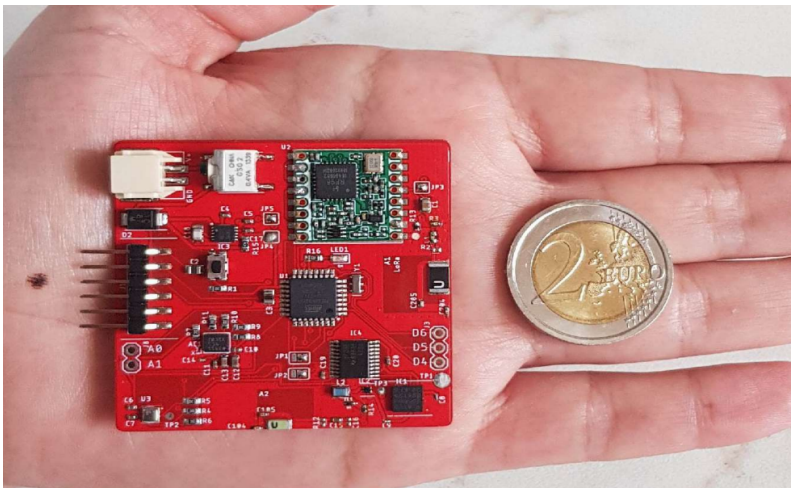

Figure 6.1: **Visualization of the radioprobes: weight 7 g and size 50 mm × 50 mm**

6.1.1 Working principle and radioprobe system architecture

The basic structure of the whole system is shown in Figure 6.2, where the main parts are highlighted in detail. The biodegradable balloons with radioprobes inside, the base stations, which receive, store, and pass this information to the processing machine; and the processing machine, which is used for database management, filtering, and visualization.

The HDV camera was used to measure balloons positions in the first stages of the experiments and to compare them with the positions supplied by the GPS. Moreover, it is important that the launch situ is close to a meteorological station that supplies reference humidity, pressure, and temperature to calibrate the radioprobe.

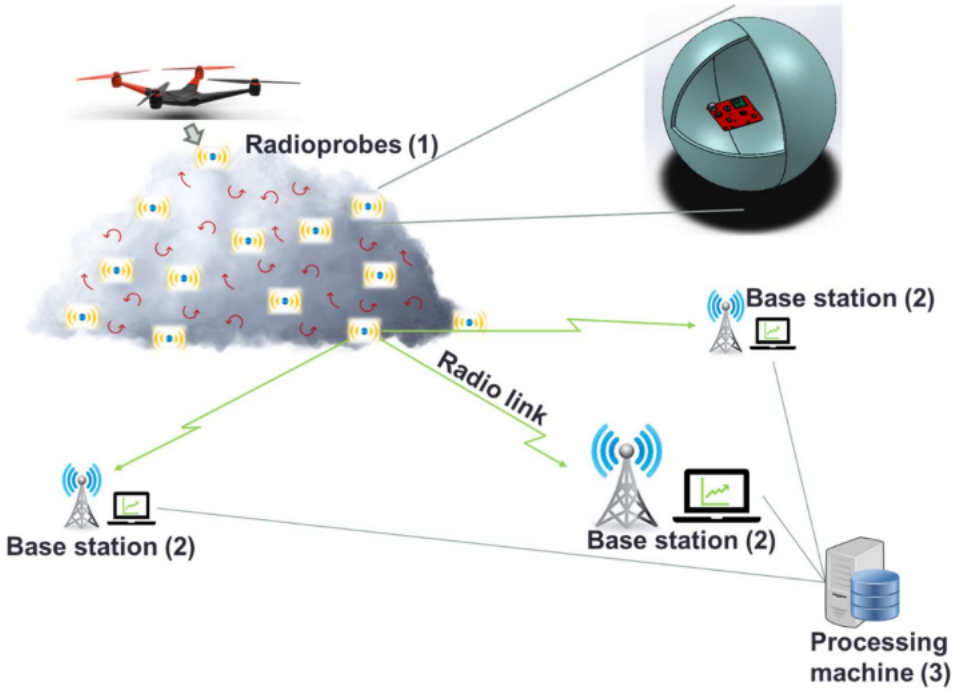

Figure 6.2: **Fundamental Work structure**

6.1.2 Materials used to make a biodegradable balloon

In this survey, the main materials used for balloons are latex and Mylar. The designed balloons are very thin with 30 μm and have a density of 1.3 gcm^{-3} [30]. The diameter is less than 14 cm, the thicknesses are between 30-60 μm, and they were made with Mylar, PLA, and Mater-Bi. A flowchart of the balloon fabrication process is shown in Fig. 6.3.

The latex balloons were purchased as balloons and therefore did not undergo any synthesis or processing. Two sheets were then assembled in a carving press, separated by a Teflon film, which has the shape of the balloon shown in Fig. 6.3 for more details see [149].

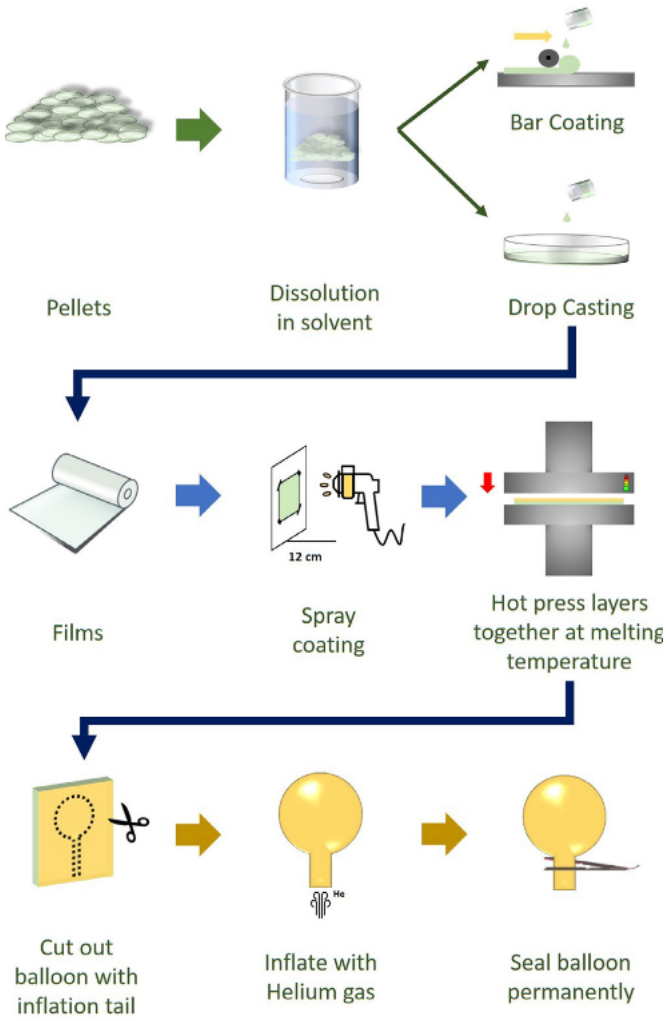

Figure 6.3: **Flow chart of balloon making process. The first row is relevant for compounds that are acquired in the form of pellets and describe how the films used in this study are made. The second row is about the surface treatments that were done. If the material comes in the form of sheets, the procedure usually starts from the second row. The last steps are specific to making the final balloons [149].**

6.1.3 Turbulent dispersion analysis via distance-neighbor graphs from direct numerical simulations

The turbulent diffusion problem is about how transportable quantities such as heat and mass are transported by the motion of the fluid [51], [85]. Turbulent particle transport plays a major role in many applications, such as water droplet growth and collisions in clouds [55], [101] rain formation [54], [164], plankton accumulation in the oceans [98], transport and sedimentation of sand particles in the environment [39], atomization in internal combustion engines [51], and many more, see the reviews by Kuerten [75] and Elghobashi [141].

Numerous studies have addressed turbulent diffusion, almost most of them based on Richardson's hypothesis [23], [112], [9], [37] where they investigated homogeneous isotropic turbulence [128]. Here, I address **non-stationary, time-decaying non-homogeneous turbulence**, which is more realistic. Richardson L. [51] discussed diffusion in terms of the distance neighbour graph function. He concluded that diffusion is an increasing function of separation, $F(l) \sim l^{4/3}$. Later, his studies were revisited by [85], to generalize the distance neighbour graph function in three dimensions. In the meantime, [112] also suggested his relation, which is equivalent to Richardson's power law, and it links separation distance directly with time. This combined result is also called **Richardson-Obukhov t^3 theory**.

The basic concept of that fundamental theory is here briefly recalled.

Let's consider ensembles of N droplets in a cluster of size $2L$ for which the $Q-l$ distance-neighbor graph can be built. The variable $Q_{n,n+1}$ is the number of neighbor droplets per length computed as follows:

$$Q_{n,n+1} = \frac{1}{N}(D^1_{n,n+1} + D^2_{n,n+1} + D^3_{n,n+1} + ... + D^N_{n,n+1}), \tag{6.1}$$

Here D^k represents a number of neighbors at a distance L, with $nh \leq l < (n+1)h$ with h a chosen unit length.

Since the integral is given as:

$$\int_{-\infty}^{+\infty} Q dl = (N-1) \tag{6.2}$$

is equal to one less the number of droplets, in the assumption of constant N, the following relation results

$$\int_{-\infty}^{+\infty} \frac{\partial Q}{\partial t} dl = 0. \tag{6.3}$$

so the area between the l axis and the time derivative of Q is null. The described theory has been applied to the fields resulting from the DNSs. A cluster with 498 and 428 monodisperse droplets is selected in the cloud and mixing region, respectively. The selected droplets are initially concentrated in a $2cm \times 2cm \times 2cm$ cubic domain with a center located in (24.4,24.4,24.4) cm. The time evolution

of these clusters is shown in Figures 6.4 and 6.5. Looking at these pictures, it is evident that the droplets diffusion is stronger in the mixing region than in the cloud one.

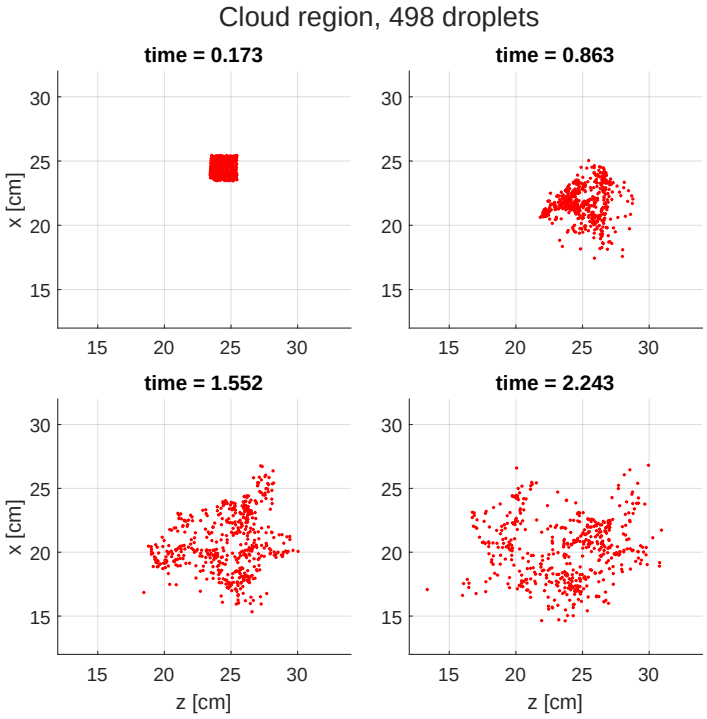

Figure 6.4: **Droplet positions in simulation domain represented in xz plane at four-time instances for cloud region. 498 droplets are selected within the same cell (neighborhood) initially and they are located in 2cm x 2cm x 2cm cubic domain, which has a center in (24.4,24.4,24.4) cm.**

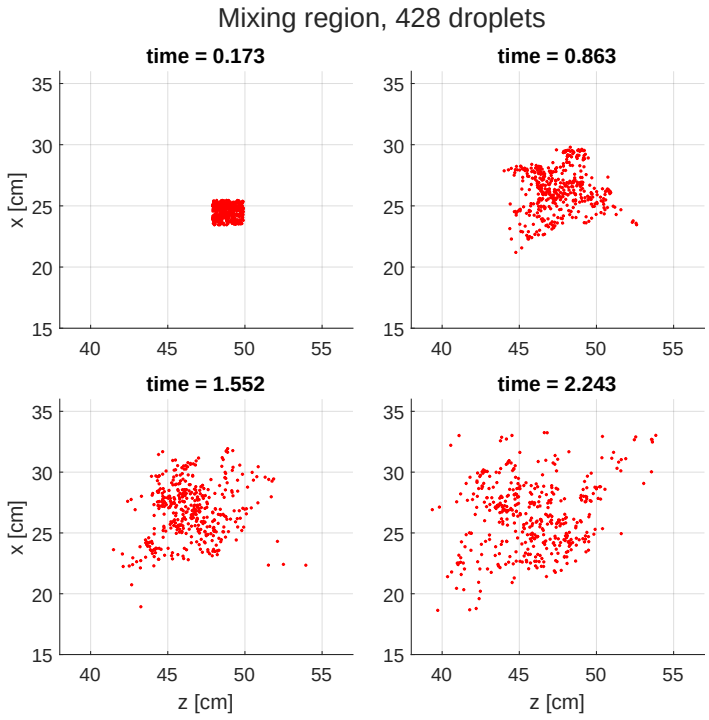

Figure 6.5: **Droplet positions in simulation domain represented in xz plane. Figures are generated for four different time instances. 428 droplets are selected within the same cell (neighborhood) initially, and they are located in the 2cm x 2cm x 2cm domain around position (24.4,24.4,48.9).**

The mean number of neighbors Q with respect to distance L between droplets is computed in the **3D** space for the selected droplet clusters. The computation has been made for distances from h to $15h$, where $h = 2cm$. Figure 6.6 is representing the Q and its time derivative at different time instances for the droplets in the cloud and mixing regions.

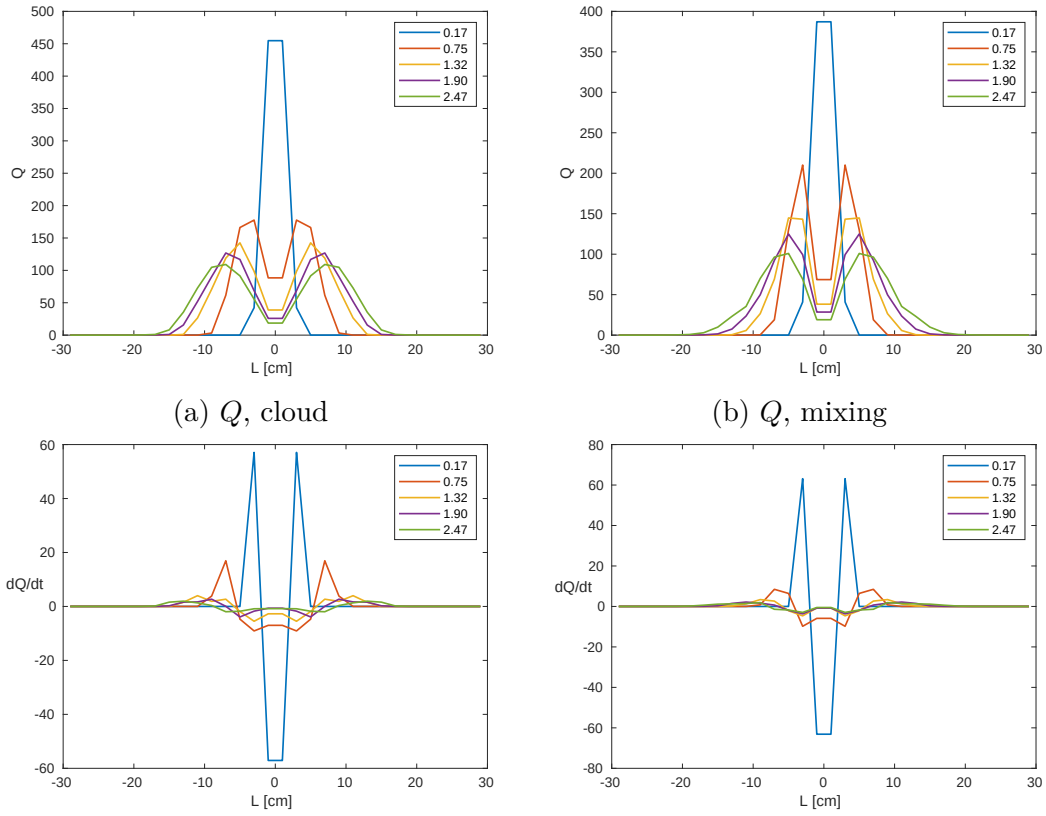

(a) Q, cloud

(b) Q, mixing

(c) dQ/dt, cloud

(d) dQ/dt, mixing

Figure 6.6: **Q at different time instances for cloud and mixing regions. The plot is for Monodispers distribution.**

In Figures, 6.6(a,b) the area underlying the Q curves represents the number of droplets and is constant in time while the area between dQ/dt and the horizontal axis in the Figures 6.6(c,d) is null. Moreover, it is evident that the rate of diffusion increases with the separation l of neighbors. This observation confirms the diffusion theory by Richardson. The property (6.3) implies that Q must satisfy a differential equation of the type

$$\frac{\partial Q}{\partial t} = \frac{\partial}{\partial l}\left\{\begin{array}{l}\text{some function of } l \text{ which attains a limit as} \\ l \to \infty \text{ equal to that attained as } l \to -\infty\end{array}\right\} \tag{6.4}$$

According to the Fick law, we can represent this by writing,

$$\frac{\partial Q}{\partial t} = K\frac{\partial^2 Q}{\partial l^2}. \tag{6.5}$$

where K is the diffusion coefficient. The theory can be extended to non-Fickian conditions as

$$\frac{\partial Q}{\partial t} = \frac{\partial}{\partial l}\left(F(l)\frac{\partial Q}{\partial l}\right), \tag{6.6}$$

where $F(l)$ is a diffusion function and is also referred as $K(l)$ in the literature. Malik in [9] generalized the diffusivity to be time dependant, such that:

$$F(l, t, \epsilon) \sim \epsilon^a \, t^b \, l^c, \tag{6.7}$$

where diffusion is a function of time, separation, and TKE dissipation rate. In the following future works, the diffusion function will be analyzed in three different cases to be able to consider the behavior of diffusion of water droplets.

6.1.4 In-field radiosonde experiment at the Osservatorio Astrofisico St. Barthelemy, Valle d'Aosta

In the following subsection, the details of the in-field radiosonde experiment, which was held at the Osservatorio Astrofisico St. Barthelemy, Valle d'Aosta on November 3, 2022, are discussed. The experiment was done in collaboration with INRiM (Istituto Nazionale di Ricerca Metrologica). In this experiment, ten radiobrobes were basically tested and launched freely into the atmosphere. The balloons were filled with helium, and two ground stations were used to receive information from the probes during their flight. Two professional Sony HDV video cameras were to film the experiment and use them to compare the relative position of the balloons. The experimental setup is represented in Figure 6.7.

(a) radiosondes (b) receiver station

(c) filling balloon with helium (d) filled balloons with radiosonde

(e) calibration instrumentation (f) PHT sensor calibration

Figure 6.7: Experiment setup with (a) 10 radiosondes, (b) 2 ground stations, (c) 2 cameras, and (e) calibration instrumentation.

The trajectory of radiosondes in satellite map view with respect to time and latitude has been shown in Figure 6.8 and the 3D trajectory of the radioprobes towards the north, east, and up directions starting from the reference observation point has been represented in Figure 6.9.

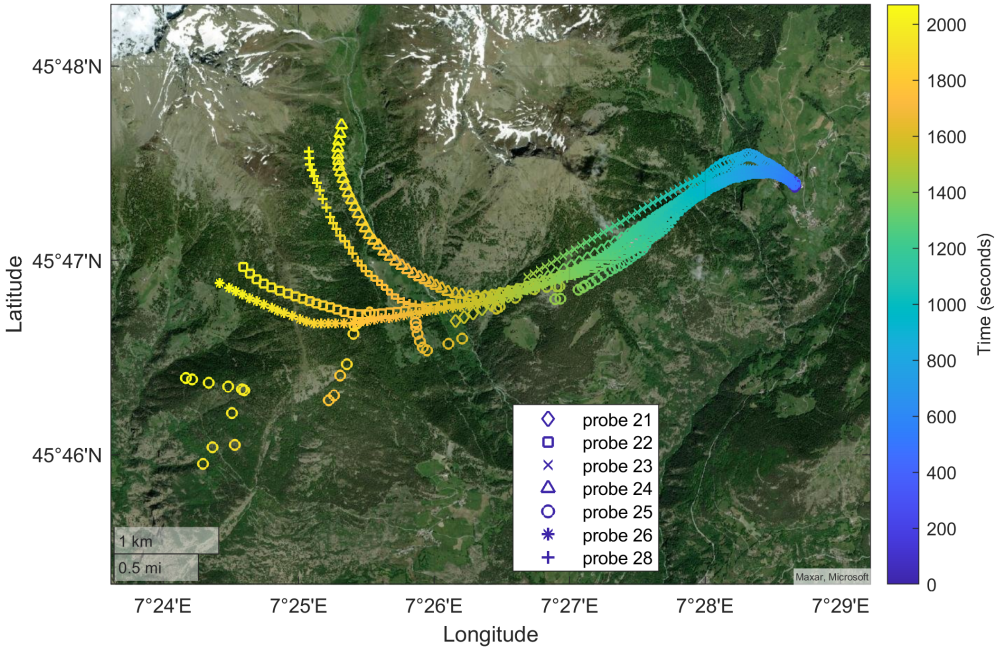

(a) Trajectory with respect to time

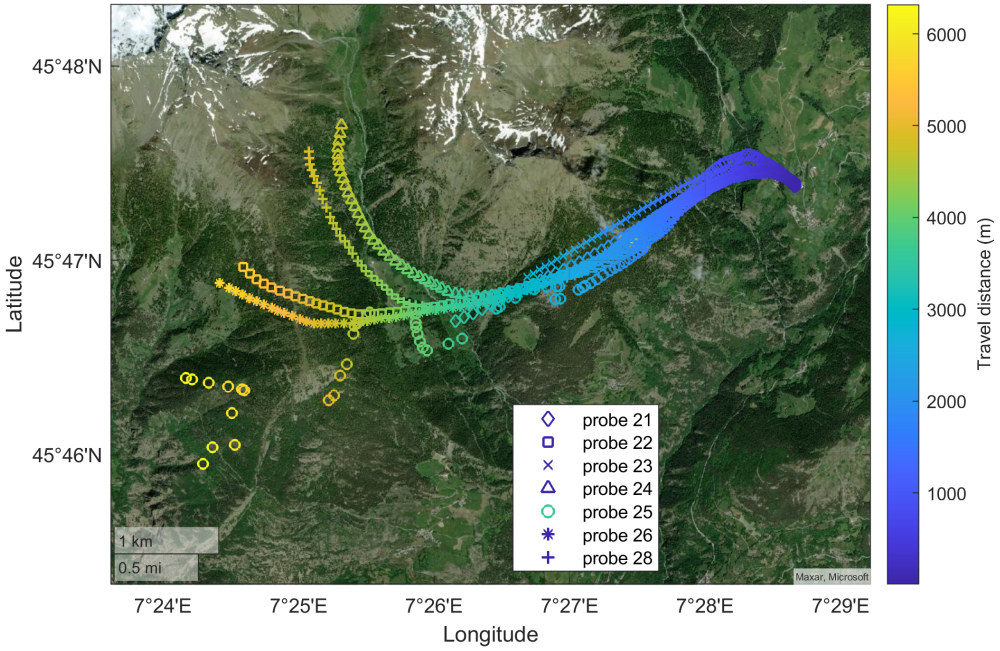

(b) Trajectory with respect to altitude

Figure 6.8: **Trajectory of the radiosondes in satellite map view with corresponding longitude and latitude readings. The color bar indicates time in seconds after the launch (a) and travel distance (b) of the radiosondes. The plotted dataset was acquired between 14:05:00 and 14:40:00 on Nov 3, 2022, at Osservatorio Astrofisico St. Barthelemy, Valle d'Aosta.**

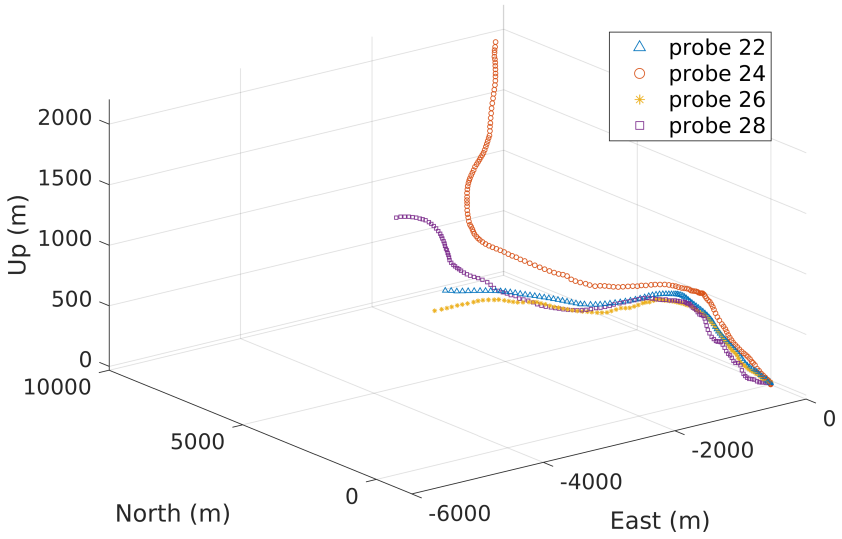

Figure 6.9: **3D trajectory of the radioprobes towards north, east, and up directions starting from the reference observation point. Reference point: latitude = 45.78994 °, longitude = 7.47764 °, altitude = 1700 meters.**

The analysis for the raw velocity from GNSS sensor readings 6.10 and positions of radioprobes in the selected time instance is demonstrated in Figure 6.11.

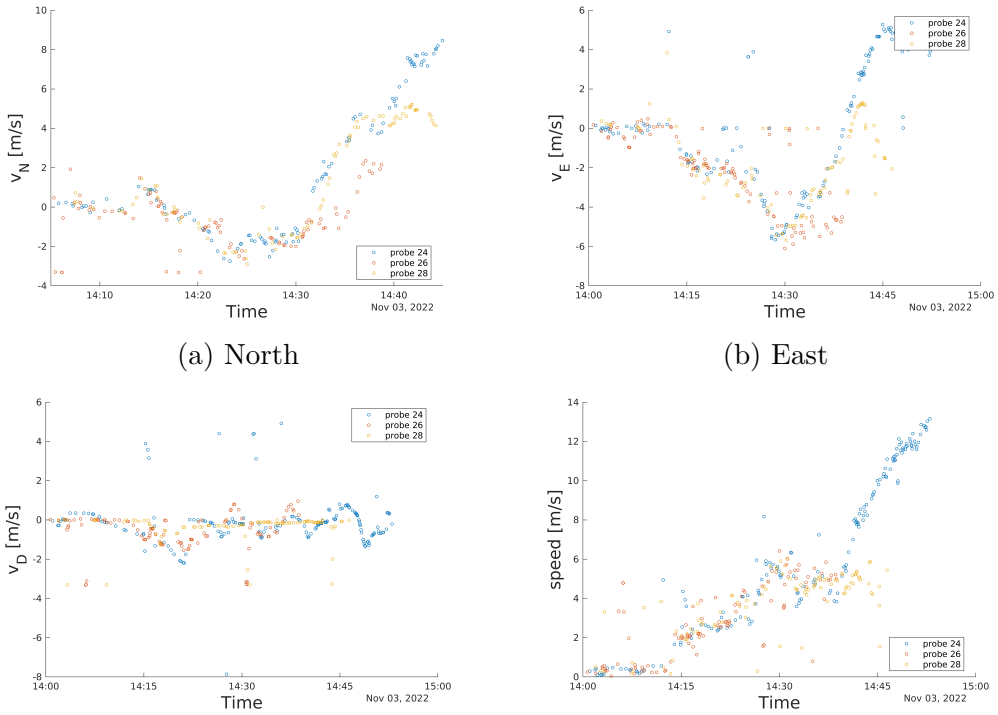

(a) North

(b) East

(c) Down

(d) Magnitude

Figure 6.10: **Raw velocity from GNSS sensor readings.**

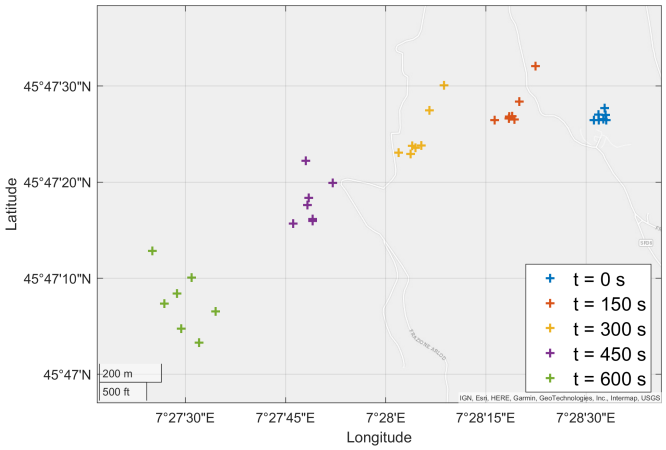

(a) Position in map

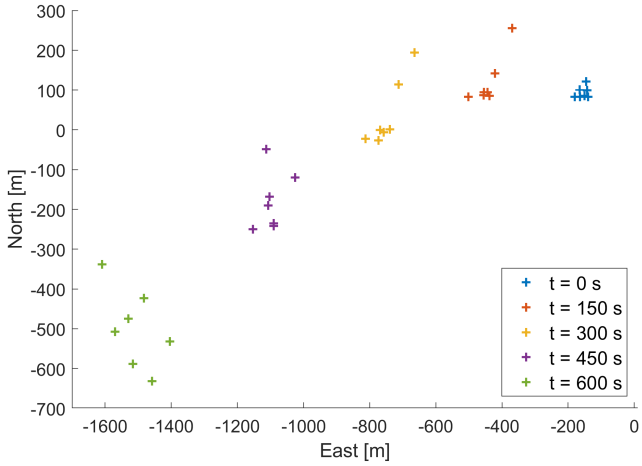

(b) Position in north-east frame

Figure 6.11: **Positions of radioprobes in the selected time instances. The initial time instance is 14:15:00. Following time instances are given in terms of seconds from the initial time instance.**

6.2 Conclusion & Future works

In this dissertation, I have shown the results of a series of Direct Numerical Simulations (DNSs), in which I have focused on the interaction of the turbulent cloud environment with the surrounding clear-air environment. I implemented Navier-Stokes' airflow turbulence in our direct numerical simulations as the gas flow phase hosting the water vapor and drops. This assumption is made both inside the clouds and in the turbulent boundary layers that separate the clouds from the surrounding clear air. I modeled these layers as a slightly unstable thermally stratified shear-less turbulence mixing.

Water vapor and water droplets have been taken into account in this air movement. Our fluid system is basically an incompressible fluid system. This system was based on Eulerian and Lagrangian equations. The main criteria controlled by the system are the velocity, temperature, and water vapor fields. These initial fields evolve under a Boussinesq approximation. Furthermore, Eulerian equations have been coupled with Lagrange equations, and the latter has been used to describe the motion of the inertial drops. The motion of the inertial drops has primarily involved both Stokes' resistance and gravitational settling. The methodology is a one-way coupling approach since it does not take into account any feedback from the drop motion to the airflow field.

One original point of this study lies in the fact that it has considered an unsteady, non-homogeneous, thus non-ergodic situation of interfacing between a cloud and clear air. First, two different types of water droplet populations were studied, considering the condition mentioned above. A population with the same droplet diameter, known as a monodisperse population, was considered as the first case. A monodisperse population distribution represents a situation in which collision processes are highly unlikely. The second and most realistic situation is a polydisperse population distribution where drops with very different radii are present. Such distribution can accommodate dominant collisions. We have included several drops, about 10 million, in the calculations of the evolution of both distributions, a number which leads to a water liquid content that matches the values of the liquid water content inside warm clouds (clouds where ice particles are not present, normally located at heights of between $1000 - 2000$ meters).

We observed marked evaporation of the droplets in the monodisperse case, accompanied by low growth due to condensation. This induces a rapid broadening of the droplet spectrum, which in turn leads to collision events. The position of the peak of the distribution of the number of drops gradually shifts toward diameters that are wider than the initial diameter, a fact that is not intuitive. Instead, as expected, the peak value decreases. We here provide quantitative data on these trends. The collision activity of the droplets becomes more intense at the Cloud and clear air interface. The colliding particle immediately evaporates at the interface, which does not happen within the cloud region. Overall, evaporation and

collision predominate over condensation at the interface.

The droplet size distribution in the polydisperse case is large from the beginning of the simulation. Therefore, the widening of the distribution is only due to the collision events. This widening is of a peaked distribution type, in which the position and value of the peak depend on the structure of the turbulence in which the droplet population is located. The width of the size distribution decreases, and the numerical concentration of the peak value increases over time. We have shown quantitative figures for these trends. The interesting feature is that much of the evaporation and condensation dynamics of this type of population take place at the lowest limit of the spectral droplet range. Evaporation predominates, together with transient condensation, within the cloud region. The evaporation resulting from condensation again predominates within the boundary layer but in a weaker form.

The collision kernel analysis has shown a clear dependence on the evolution time, as well as on the spatial region and the associated turbulence structure in which collisions occur. The statistics obtained by ensemble averaging over three simulation repetitions highlight a distinct for the kernel function but, at the same time, underline the need to conduct a further simulation campaign to increase the number of ensemble averaging to facilitate the interpolation of the kernel values during the decay of the cloud-clear air interface. This is necessary to attempt to provide an analytical model of collision dynamics under conditions that are far from ergodicity. We believe about 20 simulation repetitions will be necessary for the case of the multi-dispersed population and 100-200 repetitions for the monodisperse population. A comparison with the Saffman-Turner (ST) model, which is valid for an almost monodisperse population under stationary and isotropic turbulence conditions, highlighted the consequences introduced by having studied a system that is close to a physical reality, which is almost always non-stationary and spatially inhomogeneous.

By focusing on the only dynamic parameter present in the Saffman-Turner model, that is, the dissipation of turbulent energy under equivalent conditions, we observed ST values that were many orders of magnitude lower in our simulation. The morphology was also different. We observed a structure in our preliminary observations. However, in order to reach a more precise conclusion about this topic, we would need to run the simulation campaign mentioned above. It is interesting to note that the kernel value we observed in our simulation is of the same order of magnitude as the term that refers to the collision between droplets moving with air. Therefore, the gravitational deposition, which contains about 300,000 of the 10 million drops outside the computational domain, does not seem to have the same effect on the kernel statistics we obtained in our simulation as in the ST model. However, the crucial clue that has emerged from both the monodisperse and poly-disperse population simulations is that the unsteady turbulence mixing that limits the cloud region does not suppress the droplet collision activity. In a

time period in which the kinetic energy of the air stream that contains the cloud decreases by 90%, the collision activity inside the cloud decreases by 40%. Still, it increases by 25% inside the layer interacting with clear air. This is a result of the very rapid differentiation of droplet size due to the different weights of evaporation and condensation in the highly intermittent mixing region.

This result can explain, at least in part, the rapid increase in droplet size observed in some cumulus cloud formations, especially maritime ones, which are thought believed to be able to trigger rainfall. We would like to carry out a simulation campaign focused on the microphysics and dynamics observed in the clouds and their boundary regions, considering larger domain scales than those dealt with here. In order to obtain a long observation window, corresponding to one minute of the real phenomenon, instead of the few seconds of the present simulation, the background flow in the cloud and in the clean air area would need to be appropriately forced in different ways. This would be done to keep the kinetic energy ratio between the two regions (cloud and clear air) as constant as possible over time. Moreover, it would be appropriate, in the future, to include the effects of possible droplet fragmentation during collisions and the electromagnetic radiation present in the atmosphere in this type of direct numerical turbulent simulation. It would also be interesting to leave out the Boussinesq hypothesis, as it filters out certain important physical aspects, such as gravitational and acoustic waves in the atmosphere. The relationship between supersaturation fluctuations and turbulent small-scale dynamics in the context of an inhomogeneous, anisotropic, shear-free, turbulent air mixing layer was investigated. The different time scales affecting the microphysics of a droplet population were compared in the upper part of the cloudy region, the layer where the turbulent transport process to the saturated ambient air occurs. The time scales for evaporation, reaction, and phase relaxation agree at a value of about $20 \sim 30$ s in the layer just before the point where the supersaturation flux reaches its maximum rate of change. In the case of a polydisperse population, this agreement includes condensation time. The time scales before this spatial location are different, with differences in the order of a minute. Beyond this location, the evaporation and reaction times overlap, while the relaxation phase and condensation time scales diverge asymptotically as the environment becomes more and more undersaturated.

Assuming that the fluctuation in supersaturation depends in large part on the small-scale disruption of the carrier stream in which the vapor and liquid water phases reside, I analyzed the equation of the supersaturation balance to show their mutual correlation. To test this hypothesis, I fitted the estimated planar mean values of the time derivative of the supersaturation and condensation terms to the planar covariance of the supersaturation and the longitudinal velocity derivatives. The statistics of the velocity derivatives are particularly important for small-scale dynamics. For the specific shear-less turbulent structure considered here, the longitudinal velocity derivatives are more important for small-scale intermittency than

the transverse derivatives, which are zero. Moreover, the longitudinal velocity derivative can be considered a characteristic measure of the small-scale frequency. I found a high value of the Pearson correlation coefficient, $\rho_{\overline{\mathcal{P}_t},\mathrm{cov}_{S\partial u_i/\partial x_i}} \sim 0.7$ for the droplet populations both within the boundary layer and over the entire simulation run, leading to the conclusion that in the absence of updraft, the mismatch in the time derivative of the supersaturation and condensation terms is linearly related to the covariance of the supersaturation and longitudinal velocity derivatives of the carrier current.

The last part of the results from numerous laboratory and field testing demonstrated that the newly built radioprobe board functions satisfactorily provides correct data, and offers distinctive characteristics for the development of an instrumented weather balloon. For instance, the small size measuring instrument (5 cm x 5 cm) and extremely lightweight (7 g without taking into account the battery) are crucial features to assure a minimal moment of inertia and a minimal volume (relative to the followed trajectory). Additionally, this makes it possible to easily integrate the electronics into the balloon and achieve the buoyancy needed by the system to study turbulence from the Lagrangian perspective.

The measurement of small-scale cloud variations from the inner turbulence time scale is also guaranteed by the radioprobe's power autonomy over a time span of about 60 minutes, which is sufficient for the scope of this study endeavor. Furthermore, as its recovery after the in-cloud measurement is not anticipated, the radioprobe has been created to be disposable. To accomplish this, the instrument has a communication system that enables it to wirelessly transmit the data it has gathered to the ground. Additionally, each micro radioprobe has embedded sensors that can monitor the temperature, pressure, and humidity of nearby warm inner clouds as well as the surrounding air. It also has sensors to track the balloon's movements along its path and monitor its variations in velocity and acceleration; this data will be used to explain the characteristics of shallow warm cloud systems using temporal and spatial-spectral analysis. Each radioprobe is capable of providing precise information for the ranges required by the system in line with the atmospheric spectra produced from in-field measurements of the atmosphere region of interest. For instance, 0 °C to +30 °C in temperature, 400 mbar to 1100 mbar in external pressure, and 0 to 100 percent in relative humidity. The radioprobe's sensors can precisely detect values outside of the ranges even though these are the expected values inside the cloud observing target, making the instrument useful for various applications.

Future work will involve incorporating the newly designed radio probe boards into the finished bio balloons and testing the entire system in actual warm cloud environments over land and alpine environments since the research project's ultimate objective is the generation of an in-field cloud Lagrangian dataset. To do this, it is planned to use multiple instrumented balloons that operate as a single system to

broadcast the gathered cloud data to the ground stations concurrently. The accurate research of small-scale turbulence effects on warm clouds will be made possible by this collaborative effort, resulting in unique knowledge that will further our understanding of cloud formation. The Project COMPLETE open-access database will make the cloud-based Lagrangian datasets available to the scientific community. The analysis has been done by implementing the Richardson theory and the quantification of the turbulent dispersion and diffusion with distance neighbor function within the context of direct numerical simulations (DNSs).

The contribution of this study consists in having considered one of the possible shear-free transient interactions between cloud and clean air that are commonly present in the natural sequence of stages lasting about 100 seconds that mark the rhythm of a cloud life. The natural system anisotropy, including that of the small scale of turbulence, is taken into account. Two different types of water droplet populations have been considered. The case of a population containing drops initially having the same diameter, a situation in which collisions are in fact unlikely, and the case of a population of drops with very different radii (polydisperse, with uniform mass per class of radii), which, on the contrary, is biased to host many collision events. In both cases, we have included in the computational domain a number of drops of the order of 10 million, which matches the real liquid water content of warm clouds.

Bibliography

[1] Aliseda A. et al. “Effect of preferential concentration on the settling velocity of heavy particles in homogeneous isotropic turbulence”. In: *Journal of Fluid Mechanics* 468 (2002), pp. 1469–7645. DOI: https://www.cambridge.org/core/journals/journal-of-fluid-mechanics.

[2] Baker B. A. “Turbulent entrainment and mixing in clouds: A new observational approach”. In: *Journal of the Atmospheric Sciences* 49 (1992), pp. 387–404. DOI: 10.1175/1520-0469(1992)049<0387:TEAMIC>2.0.CO;2.

[3] Briggs D. A. et al. “Entrainment in a shear-free turbulent mixing layer”. In: *Journal of Fluid Mechanics* 310 (2006), pp. 215–241. DOI: 10.1017/S0022112096001784.

[4] Cooper W. A. “Effects of Variable Droplet Growth Histories on Droplet Size Distributions. Part I: Theory”. In: *Journal of Atmospheric Sciences* 46.10 (1989), pp. 1301–1311. DOI: 10.1175/15200469(1989)046<1301:EOVDGH>2.0.CO;2.

[5] Gabilly A. “On the role that turbulence can play in the coalescence of cloud droplets”. In: *Ann Geophys* 5 (1949), pp. 232–234.

[6] Isaac G. A. et al. “Summer cumulus cloud seeding experiments near Yellowknife and Thunder Bay, Canada”. In: *Journal of Applied Meteorology* 21 (1977), pp. 1266–1285. DOI: 10.1021/es0485681.

[7] Kaneda Y. Ishihara T. Yokokawa M. Itakura K. Uno A. “Energy dissipation rate and energy spectrum in high resolution direct numerical simulations of turbulence in a periodic box”. In: *Physics of Fluids* 15 (2003), pp. L21–L24. DOI: 10.1063/1.1539855.

[8] Khain A. et al. “Possible aerosol effects on lightning activity and structure of hurricanes”. In: *Journal of Atmospheric Science* 65 (2008), pp. 3652–3677. DOI: 10.1175/2008JAS2678.1.

[9] Malik N. A. and Hussain Fazle. “New scaling laws predicting turbulent particle pair diffusion, overcoming the limitations of the prevalent Richardson-Obukhov theory”. In: *Physics of Fluids* 33.3 (2021), p. 035135.

[10] Vaillancourt P. A., Yau M. K., and Grabowski W. W. "Microscopic approach to cloud droplet growth by condensation. Part I: model description and results without turbulence". In: *Journal of the Atmospheric Sciences* 58.14 (2001), pp. 1945–1964. DOI: 10.1175/1520-0469(2001)058<1945:MATCDG>2.0.CO;2.

[11] Vaillancourt P. A. et al. "Microscopic approach to cloud droplet growth by condensation. Part II: Turbulence, clustering, and condensational growth". In: *Journal of the Atmospheric Sciences* 59.24 (2001), pp. 3421–3435. DOI: 10.1175/1520-0469(2002)059<3421:MATCDG>2.0.CO;2.

[12] Kolmogorov A.N. "The local structure of turbulence in incompressible viscous fluid for very large Reynolds numbers". In: *Doklady Akademii Nauk SSSR* (1941), pp. 301–304.

[13] Baker M. B., Corbin R. G., and Latham J. "The influence of entrainment on the evolution of cloud droplet spectra: I. A model of inhomogeneous mixing". In: *Quarterly Journal of the Royal Meteorological Society* 106.449 (1980), pp. 581–598. DOI: 10.1002/qj.49710644914.

[14] Gilbert B. "Diffusion mixing in grid turbulence without mean shear". In: *Journal of Fluid Mechanics* 100 (1980), pp. 349–365. DOI: 10.1017/S002211208000119X.

[15] Jensen J. B. and Charlson R. J. "On the efficiency of nucleation scavenging". In: *Tellus 36E* (1984).

[16] Knaepen B., Debly Quy O., and Carati D. "Direct numerical simulation and large-eddy simulation of a shear-free mixing layer". In: *Journal of Fluid Mechanics* 514 (2004), pp. 153–172. DOI: 10.1017/S0022112004000035.

[17] Kostinski A. B. and Jameson A. R. "On the spatial distribution of cloud particles". In: *Journal of the Atmospheric Sciences* 57 (2000), pp. 901–915. DOI: 10.1175/1520-0469(2000)057<0901:OTSDOC>2.0.CO;2.

[18] Kumar B., Schumacher J., and Shaw R. A. "Cloud microphysical effects of turbulent mixing and entrainment". In: *Theoretical and Computational Fluid Dynamics* 27.3-4 (2013), pp. 361–376. DOI: 10.1007/s00162-012-0272-z.

[19] Kumar B., Schumacher J., and Shaw R. A. "Lagrangian mixing dynamics at the cloudy–clear air interface". In: *Journal of the Atmospheric Sciences* 71.7 (2014), pp. 2564–2580. DOI: 10.1175/JAS-D-13-0294.1.

[20] Kumar B., Schumacher J., and Shaw R. A. "Lagrangian mixing dynamics at the cloudy–clear air interface". In: *Journal of the Atmospheric Sciences* 71 (2014). DOI: 10.1175/JAS-D-13-0294.1.

[21] Kumar B. et al. "Scale Dependence of Cloud Microphysical Response to Turbulent Entrainment and Mixing". In: *Journal of Advances in Modeling Earth Systems* 10.11 (2018), pp. 2777–2785. DOI: 10.1029/2018MS001487.

[22] Pinsky M. B. and Khain A. P. "Turbulence effects on droplet growth and size distribution in clouds - A review". In: *Journal of the Aerosol Science* 28 (1997), pp. 1177–1214. DOI: 10.1016/S0021-8502(97)00005-0.

[23] Sawford B. "Turbulent relative dispersion". In: *Annual review of fluid mechanics* 33 (2001), p. 289.

[24] Devenish B.J. et al. "Droplet growth in warm turbulent clouds". In: *Royal Meteorological Society* 138.667 (2012), pp. 1401–1429. DOI: 10.1002/qj.1897.

[25] Ma B.K. and Warhaft Z. "Some aspects of the thermal mixing layer in grid turbulence". In: *Phys. Fluids* 29 (10 1986), pp. 3114–3120.

[26] A. BISTAGNINO et al. "Nonlinear dynamics of the viscoelastic Kolmogorov flow". In: *Journal of fluid mechanics* 509 (2007).

[27] D. A. Briggs et al. "Entrainment in a shear-free turbulent mixing layer". In: *Journal of Fluid Mechanics* 310 (1996), pp. 215–241. DOI: 10.1017/S0022112096001784.

[28] Almeida F. C. "The collisional problem of cloud droplets moving in a turbulent environment. Part I: A method of solution". In: *Journal of Atmospheric Science* 33 (1976), pp. 1571–1578. DOI: 10.1029/2003GL018567.

[29] Almeida F. C. "The collisional problem of cloud droplets moving in a turbulent environment. Part II: Turbulent collision efficiencies". In: *Journal of Atmospheric Science* 36 (1979), pp. 1564–1576. DOI: 10.1029/2003GL018567.

[30] Bastioli C. "Properties and applications of Mater-Bi starch-based materials". In: *Polymer Degradation and Stability* 59 (1998). DOI: 10.1016/S0141-3910(97)00156-0.

[31] Reade W. C. and Collins L. R. "Effect of preferential concentration on turbulent collision rates". In: *Physics of Fluid* 12.10 (2000), pp. 2530–2540. DOI: 10.1063/1.1288515.

[32] Siewert C., Bec J., and Krstulovic G. "Statistical steady state in turbulent droplet condensation". In: *Journal of Fluid Mechanics* 810 (2017), pp. 254–280. DOI: 10.1017/jfm.2016.712.

[33] Srivastava R. C. "A study of the effect of precipitation on cumulus dynamics". In: *Journal of Atmospheric Science* 24 (1967), pp. 36–45. DOI: 10.1017/S0022112004000035.

[34] Lu Ch. et al. "On Which Microphysical Time Scales to Use in Studies of Entrainment-Mixing Mechanisms in Clouds". In: *Journal of Geophysical Research: Atmospheres* 123.7 (2018), pp. 3740–3756. DOI: 10.1002/2017JD027985.

[35] Moeng CH. "Entrainment rate, cloud fraction, and liquid water path of PBL stratocumulus clouds". In: *J. Atmos. Sci.* 57.21 (2000), pp. 3627–3643. DOI: 10.1175/1520-0469(2000)057<3627:ERCFAL>2.0.CO;2.

[36] Abma D., Heus T., and Mellado J. P. "Direct Numerical Simulation of Evaporative Cooling at the Lateral Boundary of Shallow Cumulus Clouds". In: *Journal of the Atmospheric Sciences* 70 (2014), pp. 2088–2102. DOI: 10.1175/JAS-D-12-0230.1.

[37] Andrew D. Bragg A. D., Ireland P. J., and Collin L. R. "Forward and backward in time dispersion of fluid and inertial particles in isotropic turbulence". In: *Physics of Fluids* 28 (2016), p. 013305. DOI: 10.1063/1.4939694.

[38] Arenberg D. "Turbulence As The Major Factor in the Growth of Cloud Drops". In: *Bulletin methodology American society* 20 (1939), pp. 444–448.

[39] Lakehal D. "On the modelling of multiphase turbulent flows for environmental and hydrodynamic applications". In: *International Journal of Multiphase Flow* 28 (2002), pp. 823–863. DOI: 10.1016/S0301-9322(01)00086-6.

[40] Lamb D. and Verlinde J. "Physics and Chemistry of Clouds". In: *Cambridge University Press* 102 (2011), pp. 4231–4245. DOI: 10.1029/96JD02867.

[41] Tordella D. and Iovieno M. "Decaying turbulence: what happens when the correlation length varies spatially in two adjacent zones". In: *Physica D.* 242 (2012), pp. 270–281. DOI: 10.1016/j.physd.2011.09.001.

[42] Tordella D. and Iovieno M. "Numerical experiments on the intermediate asymptotics of shear-free turbulent transport and diffusion". In: *Journal of Fluid Mechanics* 549 (2006), pp. 429–441. DOI: 10.1017/S0022112005007688.

[43] Tordella D. and Iovieno M. "Small scale anisotropy in turbulent shearless mixing". In: *Physical Review Letters* 19.8 (2011), pp. 555–574. DOI: 10.1103/PhysRevLett.107.194501.

[44] Tordella D., Iovieno M., and Bailey P. R. "Sufficient condition for Gaussian departure in turbulence". In: *Physical Review E* 77.1 (2008), pp. 016–309. DOI: 10.1103/PhysRevE.77.016309.

[45] Woods J. D. and Mason B. J. "The wake capture of water drops in air". In: *Quarterly Journal of the Royal Meteorological Society* 91 (1965), pp. 35–43. DOI: 10.1002/qj.49709138706.

[46] Bodenschatz E. et al. "Can We Understand Clouds Without Turbulence?" In: *Review Of Geophysics* 327 (2010), pp. 970–971. DOI: 10.1126/science.1185138.

[47] Dimotakis P. E. "The mixing transition in turbulent flows". In: *Physics of Fluids* 409 (2000), pp. 69–98. DOI: 10.1017/S0022112099007946.

[48] Gill A. E. *Atmosphere Ocean Dynamics*. Academic Press, New York, 662pp., 1982.

[49] Howell W. E. "The growth of cloud drops in uniformly cooled air". In: *Journal of meteorology* (1949).

[50] Perin V. E. and Jonker H. J. J. "Lagrangian droplet dynamics in the subsiding shell of a cloud using Direct Numerical Simulations". In: *Journal of the Atmospheric Sciences* 72 (2015), pp. 4015–4028. DOI: 10.1175/JAS-D-15-0045.1.

[51] Richardson L. F. "Atmospheric diffusion shown on a distance-neighbour graph". In: *Proceedings of the Royal Society of London. Series A, Containing Papers of a Mathematical and Physical Character* 110.756 (1926), pp. 709–737.

[52] Yang F. et al. "Cloud droplet size distribution broadening during diffusional growth: ripening amplified by deactivation and reactivation". In: *Atmospheric Chemistry and Physics* 18 (2018), pp. 7313–7328. DOI: 10.5194/acp-18-7313-2018.

[53] Boffetta G., Celani A., and Mazzino A. "Drag reduction in the turbulent Kolmogorov flow". In: *Phys. Rev. E* 71 (2005).

[54] Falcovich G. and Pumir B. "Intermittent distribution of heavy particles in a turbulent flow". In: *Physics of Fluids* 16 (2004). DOI: 10.1063/1.1755722.

[55] Falkovich G., Fouxon A., and Stepanov M. G. "Acceleration of rain initiation by cloud turbulence". In: *Nature* 419 (2002), pp. 601–638. DOI: 10.1038/nature00983.

[56] Good G., Gerashchenko S., and Warhaft Z. "Intermittency and inertial particle entrainment at a turbulent interface: the effect of the large-scale eddies". In: *Journal of fluid mechanics* 694 (2012), p. 371.

[57] Good G., Gerashchenko S., and Warhaft Z. "Intermittency and inertial particle entrainment at a turbulent interface: the effect of the large-scale eddies". In: *Journal of fluid mechanics* 694 (2012), p. 371.

[58] Liu Y. G. and Hallett J. "On size distributions of cloud droplets growing by condensation: A new conceptual model". In: *Journal of Atmospheric Science* 55 (1998), pp. 527–536. DOI: 10.1175/1520-0469(1998)055<0527:OSDOCD>2.0.CO;2.

[59] Saffman P. G. and Turner J. S. "On the collision of drops in turbulent clouds". In: *Journal of Fluid Mechanics* 1 (1955), pp. 16–30. DOI: 10.1017/S0022112056000020.

[60] Sardina G. et al. "Broadening of cloud droplet size spectra by stochastic condensation: effects of mean updraft velocity and CCN activation". In: *Journal of The Atmospheric Science* 75 (2018), pp. 451–467. DOI: 10.1175/JAS-D-17-0241.1.

[61] Sardina G. et al. "Continuous growth of droplet size variance due to condensation in turbulent clouds". In: *Phys. Rev. Lett* 115 (2015), p. 184501. DOI: 10.1029/2003GL018567.

[62] Speziale C. G. and Bernard P. S. "The energy decay in self-preserving isotropic turbulence revisited". In: *Physics of Fluids* 241 (1992), pp. 645–667. DOI: 10.1017/S0022112092002180.

[63] Austin P. H. et al. "Small-scale variability in warm continental cumulus clouds". In: *Journal of the Atmospheric Sciences* 42 (1985), pp. 1123–1138. DOI: 10.1175/1520-0469.

[64] Kohler H. "The nucleus in and the growth of hygroscopic droplets". In: *Trans. Faraday SWang2006aoc.* 32.32 (1936), pp. 1152–1161. DOI: https://pdfslide.net/documents/the-nucleus-in-and-the-growth-of-hygroscopic-droplets.html.

[65] Seinfeld J. H. and Pandis S. N. "Atmospheric Chemistry and Physics from air pollution to climate change". In: *J. Am. Chem. Soc* (1998).

[66] Siebert H. and Shaw R. A. "Supersaturation Fluctuations during the Early Stage of Cumulus Formation". In: *Journal of the Atmospheric Sciences* 74.4 (2017), pp. 975–988. DOI: 10.1175/JAS-D-16-0115.1.

[67] Tennekes H. and Lumley J. L. *The First Course in Turbulence*. MIT, 1972.

[68] Yoshimoto H. and Goto S. "Self-similar clustering of inertial particles in homogeneous turbulence". In: *Journal of Fluid Mechanics* 577 (2007), pp. 275–286. DOI: 10.1017/S0022112007004946.

[69] James G. Hudson and Xiaoyu Da. "Volatility and size of cloud condensation nuclei". In: *Journal Of Geophysics Research-Atmospheres* 101 (1996), pp. 4435–4442. DOI: 10.1029/95JD00192.

[70] Flossman A. I., Hall W. D., and Pruppacher H. R. "A Theoretical Study of the Wet Removal of Atmospheric Pollutants.1. The redistribution of aerosol particle scaptured through nucleation and impaction scavenging by growing cloud drops". In: *Journal of the Atmospheric Science* (1985).

[71] Saito I. and Gotoh T. "Turbulence and cloud droplets in cumulus clouds". In: *New Journal of Physics* 20.023001 (2018). DOI: 10.1088/1367-2630/aaa229.

[72] Saito I., Gotoh T., and Watanabe T. "Broadening of cloud droplet size distributions by condensation in turbulence". In: *Journal of The Meteorological Society Of Japan* 19 (2019), pp. 867–891. DOI: 10.2151/jmsj.2019-049.

[73] Ghan S. J. et al. "Droplet nucleation: physically based parameterizations and comparative evaluation". In: *Journal of Advances in Modeling Earth Systems* (2011).

[74] Ireland P. J. and Collins L. R. "Direct numerical simulation of inertial particle entrainment in a shearless mixing layer". In: *Journal of fluid mechanics* 704 (2012), p. 301.

[75] Kuerten J. "Point-Particle DNS and LES of Particle-Laden Turbulent flow - a state-of-the-art review". In: *Flow Turbulence and Combustion* 97 (2016), pp. 689–713. DOI: 10.1007/S10494-016-9765-Y.

[76] Latham J. and Reed R. L. "Laboratory studies of the effects of mixing on the evolution of cloud droplet spectra". In: *Quarterly Journal of the Royal Meteorological Society* 103.436 (1977), pp. 297–306. DOI: 10.1002/qj.49710343607.

[77] Mason B. J. and Chien C. W. "Cloud droplet growth by condensation in cumulus". In: *Quarterly Journal of the Royal Meteorological Society* 88.376 (1962), pp. 136–142.

[78] Monteith J. and Unsworth M. "Principles of Environmental Physics, 3rd Edition". In: *Academic Press* (2008), p. 440. DOI: 9780080924793.

[79] Ovadnevaite J. et al. "Surface tension prevails over solute effect in organic-influenced cloud droplet activation". In: *Nature* 546 (2017), pp. 637–641. DOI: 10.1038/nature22806.

[80] Petersen A. J., Baker L., and Coletti F. "Experimental study of inertial particles clustering and settling in homogeneous turbulence". In: *Journal of Fluid Mechanics* 864 (2019), pp. 925–970. DOI: 10.1017/jfm.2019.31.

[81] Riley J., Metcalfe R. W., and Weissman M. A. "Direct numerical simulations of homogeneous turbulence in density-stratified fluids". In: *AIP Conference Proceedings* 76.1 (1981), pp. 79–112. DOI: 10.1063/1.33198.

[82] Tritton D. J. *Physical fluid dynamics*. Oxford University, 1988.

[83] Warner J. "The microstructure of cumulus cloud". In: *Journal of Atmospheric Science* 27 (1970), pp. 682–688. DOI: 10.1017/S0022112004000035.

[84] Jayesh and Z. Warhaft. "Turbulent penetration of a thermally stratified interfacial layer in a wind-tunnel". In: *J. Fluid Mech.* 277 (1994), pp. 23–54.

[85] Batchelor G. K. *The theory of homogeneous turbulence*. Vol. 38. 1953, pp. 64–65.

[86] Chandrakar K. K. et al. "Aerosol indirect effect from turbulence-induced broadening of cloud-droplet size distributions". In: *Proceedings of the National Academy of Sciences* 113.50 (2016), pp. 14243–14248. DOI: 10.1073/pnas.1612686113.

[87] Chandrakar K. K. et al. "Droplet size distributions in turbulent clouds: experimental evaluation of theoretical distributions". In: *Quarterly Journal of the Royal Meteorological Society* 146 (2020), pp. 483–504. DOI: 10.1002/qj.3692.

[88] Eaton J. K. and Fessler J. R. "Preferential concentration of particles by turbulence". In: *International Journal of Multiphase Flow* 20 (1994), pp. 169–209. DOI: 10.1016/0301-9322(94)90072-8.

[89] Lehmann K., Siebert H., and Shaw R. A. "Homogeneous and Inhomogeneous Mixing in Cumulus Clouds: Dependence on Local Turbulence Structure". In: *Journal of the Atmospheric Sciences* 66.12 (2009), pp. 3641–3659. DOI: 10.1175/2009JAS3012.1.

[90] Takahashi K. and Vassilicos J. "An efficient parallel simulation of interacting inertial particles in homogeneous isotropic turbulence". In: *Journal of Computer Physics* 242 (2013), pp. 809–827. DOI: 10.1016/j.jcp.2013.02.027.

[91] Vallis G. K. *Atmospheric and Oceanic Fluid Dynamics*. Cambridge University Press, 2006.

[92] Yau M. K. and Rogers R. R. *A Short Course in Cloud Physics*. Elsevier Science, 1996. DOI: 978-0-08-057094-5.

[93] Yoon K.H. and Warhaft Z. "The evolution of grid generated turbulence under conditions of thermal stable stratification". In: *J. Fluid Mech.* 215 (1990), pp. 601–638. ISSN: 0022-1120. DOI: 10.1017/S0022112090002786.

[94] Bergougnoux L. et al. "The motion of solid spherical particles falling in a cellular flow field at low Stokes number". In: *Physics of Fluids* 26 (2014). DOI: 10.1063/1.4895736.

[95] Fossà L. et al. "Microphysical timescales and local supersaturation balance at a warm cloud top boundary". In: *Physics of Fluids* 34 (2022), p. 067103. DOI: 10.1063/5.0090664.

[96] Gallana L. *Statistical analysis of inhomogeneous fluctuation fields. Scalar transport in shearless turbulent mixing, effects of stratification, solar wind and solar wind-interstellar medium interaction*. 2016. URL: https://iris.polito.it/handle/11583/2653026.

[97] Gallana L. et al. "Diffusion of turbulence following both stable and unstable step stratification perturbations". In: *Physics of Fluids* 34 (2022), p. 065122. DOI: 10.1063/5.0090042.

[98] Liu L. et al. "Morphology, composition and mixing state of individual airborne particles: Effects of the 2017 Action Plan in Beijing, China". In: *Journal of Cleaner Production* 329 (2021). DOI: 10.1016/j.jclepro.2021.129748.

[99] Lumley J. L. and Panofsky H. A. *The structure of atmospheric turbulence.* Interscience Publishers, 1964.

[100] Prandtl L. "Anwendung der turbulenten Reibungsgesetze aufatmosph.rische Str.mungen. Proc. IV. Intern". In: *Congress Appl. Mech.* (1934), pp. 238–239.

[101] Xie L., Dong Z., and Zheng X. "Experimental analysis of sand particles' lift-off and incident velocities in wind-blown sand flux". In: *Acta Mechanica Sinica* 21 (2006), pp. 564–573. DOI: 10.1007/s10409-005-0078-y.

[102] Richardson L.F. "Weather Prediction by Numerical Processes". In: *Boston: Cambridge University Press.* (1922), p. 65.

[103] Andrejczuk M. et al. "Numerical Simulation of Cloud–Clear Air Interfacial Mixing: Effects on Cloud Microphysics". In: *Journal of Atmospheric Science* 63 (2006), pp. 3204–3225.

[104] Andrejczuk M. et al. "Numerical simulation of cloud–clear air interfacial mixing: homogeneous versus inhomogeneous mixing". In: *Journal of the Atmospheric Sciences* 66.8 (2009), pp. 2493–2500. DOI: 10.1175/2009JAS2956.1.

[105] Golshan M. et al. "Intermittency acceleration of water droplet population dynamics inside the interfacial layer between cloudy and clear air environments". In: *International Journal of Multiphase Flow* 140 (2021), p. 103669. DOI: 10.1016/j.ijmultiphaseflow.2021.103669.

[106] Holzner M. et al. "A Lagrangian investigation of the small-scale features of turbulent entrainment through particle tracking and direct numerical simulation". In: *Journal of fluid mechanics* 598 (2008), pp. 465–475.

[107] Iovieno M., Cavazzoni C., and Tordella D. "A new technique for a parallel dealiased pseudospectral Navier stokes code". In: *Computer Physics Communications* 141.047101 (2001).

[108] Iovieno M. and Tordella D. "The angular momentum equation for a finite element of fluid: A new representation and application to turbulent modeling". In: *Physics of Fluids* 14 (2002), pp. 2673–2682. DOI: 10.1063/1.1485765.

[109] Iovieno M. et al. "Mixing of a passive scalar across a thin shearless layer: concentration of intermittency on the sides of the turbulent interface". In: *Journal of Turbulence* (2014), pp. 311–334. DOI: 10.1080/14685248.2014.905393.

[110] Kostoglou M. and Karabelas A. J. "Evaluation of Zero Order Methods for Simulating Particle Coagulation". In: *Journal of Collide and Interface Science* 163 (1994), pp. 420–431. DOI: 10.1006/jcis.1994.1121.

[111] Lau K. M. and Wu H. T. "Warm rain processes over tropical oceans and climate implications". In: *Geophysical Research Letters* 30 (2003).

[112] Obukhov A. M. "On the distribution of energy in the spectrum of turbulent flow". In: *Bull. Acad. Sci. USSR, Géog. Géophys.* 5 (1941), pp. 453–466.

[113] Vanni M. "Approximate population balance equations for aggregation-breakage processes". In: *Journal of collide and interface science* 22.2 (1999), pp. 143–160. DOI: 10.1006/jcis.1999.6571.

[114] Graw R. Mc. and Liu Y. "Brownian drift-diffusion model for evolution of droplet size distributions in turbulent clouds". In: *Geophys. Res. Lett* 33 (2006). DOI: 10.1029/2005GL023545.

[115] Ayala O., Grabowski W. W., and Wang L. P. "A hybrid approach for simulating turbulent collisions of hydrodynamically interacting particles". In: *Journal of Computational physics* 225.1 (2007), pp. 51–73. DOI: 10.1016/j.jcp.2006.11.016.

[116] Ayala O. et al. "DNS of hydro-dynamically interacting droplets in turbulent clouds: Parallel implementation and scalability analysis using 2D domain decomposition". In: *Computer physics Communications* 185.12 (2013), pp. 3269–3290. DOI: 10.1016/j.cpc.2014.09.005.

[117] Ayala O. et al. "DNS of hydrodynamically interacting droplets in turbulent clouds: Parallel implementation and scalability analysis using 2D domain decomposition". In: *Computer physics Communications* 185.12 (2014), pp. 3269–3290. DOI: 10.1016/j.cpc.2014.09.005.

[118] Tetens O. "Tetens equation". In: *Uber einige meteorologische Begriffe.270Z. Geophys* 6 (1930), pp. 207–309.

[119] Gotzfried P. et al. "Droplet dynamics and fine-scale structure in a shearless turbulent mixing layer with phase changes". In: *Journal of Fluid Mechanics* 814 (2017), pp. 452–483. DOI: 10.1017/jfm.2017.23.

[120] Malinowski S. P. et al. "Physics of Stratocumulus Top (POST): turbulent mixing across capping inversion". In: *Atmos. Chem. Phys.* 13.24 (2013), pp. 12171–12186. DOI: 10.5194/acp-13-12171-2013.

[121] Mellado J. P. "The evaporatively driven cloud-top mixing layer". In: *J. Fluid Mech.* 660 (2010), pp. 5–36. DOI: 10.1017/S0022112010002831.

[122] Mellado J. P., Stevens B., and Schmidt H. "Wind Shear and Buoyancy Reversal at the Top of Stratocumulus". In: *J. Atmos. Sci.* 71.3 (2014), pp. 1040–1057. DOI: 10.1175/JAS-D-13-0189.1.

[123] Mellado J. P. et al. “Buoyancy reversal in cloud-top mixing layers”. In: *Quart. J. Roy. Meteor. Soc.* 135.641 (2009), pp. 963–978. DOI: 10.1002/qj.417.

[124] Prabhakaran P. et al. “The role of turbulent fluctuations in aerosol activation and cloud formation”. In: *Proceedings of the National Academy of Sciences* 117.29 (2020), pp. 16831–16838. DOI: 10.1073/pnas.2006426117.

[125] Squires P. “The Growth of Cloud Drops by Condensation. I. General Characteristics”. In: *Australian Journal of Chemistry* 5.1 (1952), pp. 59–86.

[126] Squires P. and Turner J. S. “An entraining jet model for cumulonimbus updraughts”. In: *Tellus A: Dynamic Meteorology and Oceanography* 14 (1962), pp. 422–434. DOI: 10.1017/S0022112004000035.

[127] Wang L. P., Wexler A. S., and Zhou Y. “Statistical mechanical description and modelling of turbulent collision of inertial particles”. In: *Journal of Fluid Mechanics* 415 (2005), pp. 117–153. DOI: 10.1017/S0022112000008661.

[128] Salazar Juan P.L.C. and Collins L. R. “Two-Particle Dispersion in Isotropic Turbulent Flows”. In: *Annual Review of Fluid Mechanics* 41.1 (2009), pp. 405–432. DOI: 10.1146/annurev.fluid.40.111406.102224.

[129] Miryam E. Paredes Quintanilla et al. “Innovative Mini Ultralight Radioprobes to Track Lagrangian Turbulence Fluctuations within Warm Clouds: Electronic Design”. In: *MDPI* 1351 (2021), pp. 709–737. DOI: 10.3390/s21041351.

[130] East T. W. R. and Marshall J. S. “Turbulence in clouds as a factor in precipitation”. In: *Royal Meteorological Society* (1954). DOI: 10.1002/qj.49708034305.

[131] Maxey M. R. “The motion of small spherical particles in a cellular flow field”. In: *Physics of Fluids* 30.7 (1987), pp. 1915–1928. DOI: 10.1063/1.866206.

[132] Morton B. R. et al. “Turbulent gravitational convection from maintained and instantaneous sources”. In: *Proceedings of the Royal Society of London* 14 (1956), pp. 1–23. DOI: 10.1017/S0022112004000035.

[133] Onishi R., Matsuda K., and Takahashi K. “Lagrangian Tracking Simulation of Droplet Growth in Turbulence–Turbulence Enhancement of Autoconversion Rate”. In: *Journal of Atmospheric Science* 72 (2015), pp. 2591–2607.

[134] Pruppacher H. R. and Klett J. D. *Microphysics of clouds and precipitation.* Atmospheric and Oceanographic Sciences Library, 1997.

[135] Rogers R. R. and Yau M. K. “A short course in cloud physics”. In: *Oxford New York* 113 (1989), pp. 269–276. DOI: 1991239.

[136] Ruetsch G. R. and Maxey M. R. "The evolution of small-scale structures in homogenuos isotropic turbulence". In: *Physics of Fluid* 4.12 (1993), pp. 2747–2760. DOI: 10.1063/1.858333.

[137] Sreenivasan K. R. "An update on the energy dissipation rate in isotropic turbulence". In: *Physics of Fluids* 10 (1998), pp. 528–529. DOI: 10.1063/1.869575.

[138] Sreenivasan K. R. and Antonia R. A. "The phenomenology of small-scale turbulence". In: *Ann. Rev. Fluid Mech.* 29 (1997), pp. 435–472.

[139] Rogers R.R. and Yau M.K. *A Short Course in Cloud Physics*. Elsevier Science, 1996. ISBN: 9780080570945.

[140] Sheu R.S., Curry J.A., and Liu G. "Vertical stratification of tropical cloud properties as determined from satellite". In: *Journal of Geophysical Research: Atmospheres* 102.D4 (1997), pp. 4231–4245. DOI: 10.1029/96JD02867.

[141] Elghobashi S. "Direct Numerical Simulation of Turbulent Flows Laden with Droplets or Bubbles". In: *Annual Review of Fluid Mechanics* 51 (2019), pp. 217–244. DOI: 10.1146/annurev-fluid-010518-040401.

[142] Gerashchenko S., Good G., and Warhaft Z. "Entrainment and mixing of water droplets across a shearless turbulent interface with and without gravitational effects". In: *Journal of Fluid Mechanics* 668 (2011), pp. 293–303.

[143] Gerashchenko S. and Warhaft Z. "Conditional entrainment statistics of inertial particles across shearless turbulent interfaces". In: *Experiments in fluids* 54.12 (2013), pp. 1–10.

[144] Koziol A. S. and Leighton H. G. "The Effect of Turbulence on the Collision Rates of Small Cloud Drops". In: *Journal of Atmospheric Science* 53 (1996), pp. 1910–1920. DOI: 10.1029/2003GL018567.

[145] Lanotte A. S., Seminara A., and Toschi F. "Cloud droplet growth by condensation in homogeneous isotropic turbulence". In: *Journal of the Atmospheric Sciences* 66.6 (2009), pp. 1685–1697. DOI: 10.1175/2008JAS2864.1.

[146] Twomey S. "The nuclei of natural cloud formation part II: The supersaturation in natural clouds and the variation of cloud droplet concentration". In: *Geofisica pura e applicata* 43 (1959), pp. 243–249.

[147] Veeravalli S. and Warhaft Z. "The shearless turbulence mixing layer". In: *Journal of Fluid Mechanics* 207 (1989), pp. 191–229. DOI: 10.1017/S0022112089002557.

[148] Veeravalli S. and Warhaft Z. "Thermal dispersion from a line source in the shearless turbulence mixing layer". In: *J. Fluid Mech.* 216 (1990), pp. 35–70.

[149] Basso T. et al. "Evaluation of Mater-Bi and Polylactic Acid as materials for biodegradable innovative mini-radiosondes to track small-scale fluctuations within clouds". In: *Materials Chemistry and Physics* 253 (2020). DOI: 10.1016/j.matchemphys.2020.123411.

[150] Gotoh T., Suehiro T., and Saito I. "Continuous growth of cloud droplets in cumulus cloud". In: *New Journal of Physics* 18.4 (2016), p. 043042. DOI: 1367-2630/18/i=4/a=043042.

[151] Heus T. and Jonker H. J. J. "Subsiding shells around shallow cumulus clouds". In: *Journal of the Atmospheric Sciences* 65 (2008), pp. 1003–1018. DOI: 10.1175/2007JAS2322.1.

[152] Lin J. T. and Pao Y. K. "Wakes in stratified fluids". In: *Ann. Rev. Fluid Mech.* 11 (1979), pp. 317–338.

[153] Armenio V. and Fiorotto V. "The importance of the forces acting on particles in turbulent flows". In: *Physics of Fluids* 13 (2001), pp. 2437–2440. DOI: 10.1063/1.1385390.

[154] Beard K. V., Durkee R. I., and Ochs H. T. "Coalescence Efficiency Measurements for Minimally Charged Cloud Drops". In: *Journal of the Atmospheric Sciences* 59 (2002), pp. 233–243. DOI: 10.1175/1520-0469(2002)059<0233:CEMFMC>2.0.CO;2.

[155] Eswaran V. and Pope S. B. "Direct Numerical Simulations of the Turbulent Mixing of a Passive Scalar". In: *Physics of Fluids* 31 (1988), pp. 506–520. DOI: 10.1063/1.866832.

[156] Khvorostyanov V. and Curry J. "Thermodynamics, Kinetics, and Microphysics of Clouds". In: *Cambridge University Press* 102 (2014), pp. 4231–4245. DOI: 10.1029/96JD02867.

[157] Ruggiero V., Codoni D., and Tordella D. *Numerical code for the study of water droplets' growth, collision, coalescence, and clustering inside turbulent warm cloud-clear air interfaces*. 2018. DOI: 10.5281/zenodo.2633679.

[158] Khvorostyanov V.I. and Curry J.A. *Thermodynamics, Kinetics, and Microphysics of Clouds*. Cambridge University Press, 2014. ISBN: 9781316060711.

[159] Atkinson B. W. and Zhang J. W. "Mesoscale shallow convection in the atmosphere". In: *Review of Geophysics* 34 (1996), pp. 403–431. DOI: 10.1029/96RG02623.

[160] Grabowski W. W. and Wang L. "Growth of cloud droplets in a turbulent environment". In: *Annual Review of Fluid Mechanics* 45 (2013), pp. 293–324. DOI: 10.1146/annurev-fluid-011212-140750.

[161] Reuter G. W., Villiers D., and Yavin Y. "The Collection Kernel for Two Falling Cloud Drops Subjected to Random Perturbations in a Turbulent Air Flow: A Stochastic Model". In: *Journal of Atmospheric Science* 45 (1988), pp. 765–773. DOI: 10.1175/1520-0469(1988)045<0765:TCKFTF>2.0.CO;2.

[162] Wu W. and McFarquhar G. M. "Statistical Theory on the Functional Form of Cloud Particle Size Distributions". In: *Journal of Atmospheric Science* 75 (2018), pp. 2801–2814. DOI: 10.1175/JAS-D-17-0164.1.

[163] Kimura Y. and Herring J. R. "Diffusion in stably stratified turbulence". In: *Ann. Rev. Fluid Mech.* 328 (1996), pp. 253–269. DOI: 10.1017/S0022112096008713.

[164] Li X. Y. et al. "Condensational and collisional growth of cloud droplets in a turbulent environment". In: *Journal of the atmospheric sciences* 77.1 (2020), pp. 337–353. DOI: 10.1175/JAS-D-19-0107.1.

[165] Zhou Y., Wexler A. S., and Wang L. P. "Modelling turbulent collision of bidisperse inertial particles". In: *Journal of Fluid Mechanics* 433 (2001), pp. 77–104. DOI: 10.1017/S0022112000003372.

[166] Zhou Y., Wexler A. S., and Wang L. P. "Modelling turbulent collision of bidisperse inertial particles". In: *Journal of Fluid Mechanics* 433 (2001), pp. 77–104. DOI: 10.1017/S0022112000003372.

[167] Gao Zheng et al. "Investigation of Turbulent Entrainment-Mixing Processes With a New Particle-Resolved Direct Numerical Simulation Model". In: *Journal of Geophysical Research: Atmospheres* 123 (2018), pp. 2194–2214. DOI: 10.1002/2017JD027507.

This Ph.D. thesis has been typeset by means of the TEX-system facilities. The typesetting engine was pdfLATEX. The document class was `toptesi`, by Claudio Beccari, with option `tipotesi=scudo`. This class is available in every up-to-date and complete TEX-system installation.